Master Thesis

Remote Sensing for Spatial Electrostatic Characterization using the Multi-Sphere Method

H.J.A. Engwerda

Technische Universiteit Delft

TU Delft Delft University of Technology

Challenge the future

Master Thesis

Remote Sensing for Spatial Electrostatic Characterization using the Multi-Sphere Method

Delft University of Technology
Faculty of Aerospace Engineering

March 2, 2017

by

Heiko J.A. Engwerda

Assessment committee members

Chair	Prof. Dr. E.K.A. Gill	Space Systems Engineering
	Ir. P.P. Sundaramoorthy	Space Systems Engineering
	Dr. Ir. E.N. Doornbos	Astrodynamics and Space Missions
	Prof. Dr. H. Schaub	University of Colorado Boulder

Daily supervisor: Ir. P.P. Sundaramoorthy

TU Delft Delft University of Technology

Abstract

Focusing on the rapidly increasing debris population around Earth as well as the scientific and corporate interest in Asteroids, multiple missions for interaction with non-cooperative bodies have been proposed over the last years. Applications such as the Electrostatic Tractor (ET) aiming to reduce the debris populations and missions introducing close proximity or even berthing with bodies in space all require knowledge about the electrostatic characteristics of the target. In order to infer this information in a real-time manner, the Remote Sensing for Electrostatic Characterization (RSEC) method can be applied. By measuring the ambient potential with probes extended from a dedicated spacecraft, an optimization can be performed as to find a best-fit Multi-Sphere Method (MSM) model. Consisting of a set of spheres with a point charge in their middle, this model approximates both the charge and potential of the rotating target. Comparing the in-situ measured potential with the potential obtained from the MSM model, the accuracy of the MSM model can be found and with it the model can be optimized. This thesis provides an extension of the RSEC method to three-dimensional space allowing for multi-axis tumbling motions of the target. Furthermore, simplifications of the model allowing for greater computational speed and simpler application are discussed. In order to validate the model, a Finite Element Analysis (FEA) is performed allowing the RSEC method to be tested for a representative missions scenario where the ET is applied. Based on the results of the FEA simulation, a Surface-MSM (SMSM) is constructed, allowing for multi-axis rotations of the debris, where this would be too computationally expensive with a FEA. The accuracy of force prediction within the ET method is assessed for a representative debris model. Furthermore, insights are offered in the effect of varying model parameters, and the influence of force mis-prediction on reorbiting time and fuel cost is evaluated.

Preface

Since the first introduction of space debris in a bachelor's course, the quest to remove these objects from space has intrigued me. Increased understanding of (space)-flight over the years has at least lead me to one observation: *"it's a miracle we can actually launch stuff in space"*. And now it appears we actually have to retrieve that stuff as well or otherwise there will be some nasty consequences... After thinking about solutions for a while, the working principle for old TV's stuck; deflecting charged particles by means of electromagnetic fields. A comparable solution was thought of by Dr. Schaub to remove the threat of debris, namely the electrostatic tractor. To the best of my luck, Dr. Schaub was willing to let me be part of the great research group that is the AVS lab at CU Boulder and work on this awesome research.

My gratitude goes to Ir. P.P (Prem) Sundaramoorthy, who has supported me well and provided valuable feedback, even while not his main area of interest. He has been always been more than helpful and stimulated me to deliver the best of my work. Furthermore, without the input and great knowledge of Dr. Schaub, I would not have accomplished what I have today. Thank you for your great enthusiasm and mentor-ship, during my time in Boulder, as well as afterwards. Another great that deserves appreciation, is Joseph (Joe) Hughes, who helped and encouraged me find my way through a lot of this research, and my first paper. Also without my other colleagues and friends at the AVS laboratory and in room 2.50 in Delft, I wouldn't be where I am now; thank you for being a motivator, sparring partner and a good source of laughter!

Lastly, most of my gratitude should go towards my parents, who have supported me in all my endeavors, made sure I had the least amount of concern on the way and always offered me a safe and happy home. My lovely and supportive girlfriend Isabelle also deserves a lot of appreciation for encouraging and supporting me, even when being far apart for some time. Ton and Elsemiek, thank you both for being such good and fun siblings. You have been a great example for me and I hope will stay like that for many years to come.

Contents

List of Figures

List of Tables

List of Acronyms

CoR Center of Rotation ix, 4, 10, 11, 13, 15, 16, 17, 20, 21, 22, 26, 32, 33, 51

DCM Direction Cosine Matrix 8, 9

DFT Discrete Fourier Transform x, 48, 49

ET Electrostatic Tractor 1, 2, 3, 4, 7, 9, 10, 11, 33, 47, 49, 50, 53, 56, 57, 59

FEA Finite Element Analysis x, xi, 2, 4, 5, 7, 35, 37, 39, 40, 41, 42, 43, 44, 45, 46, 48, 49, 50, 52, 56, 57, 58, 59

FWHM Full Width at Half Maximum 16

GEO Geostationary Orbit 2, 3, 4, 9, 55, 58

GUI Graphical User Interface 38

HVL High Voltage Lab 35

LiDAR Light Detection and Ranging 4, 48, 49, 57

LVLH Local Vertical Local Horizontal 7, 9, 13, 31, 53

MoI Moment of Inertia 4

MRP Modified Rodrigues Parameter 7, 8, 9

MSM Multi-Sphere Method x, 2, 3, 4, 5, 7, 9, 13, 15, 27, 29, 30, 31, 32, 35, 40, 42, 43, 45, 46, 48, 57, 58

RSEC Remote Sensing for Electrostatic Characterization x, 3, 4, 5, 7, 9, 10, 13, 27, 31, 32, 35, 36, 37, 38, 40, 41, 45, 46, 49, 50, 53, 54, 56, 57, 58, 59

SMSM Surface Multi-Sphere Method x, xi, 4, 5, 35, 41, 42, 44, 45, 47, 49, 50, 54, 57, 58, 59

List of Symbols

a	Semi-major axis [km] 55
C	Capacitance [C V^{-1}] 40
a	Charge [C] 10, 26
f	Function [-] 40
F	Coulomb force vector [N] 10
F_x	Coulomb force in x-direction [N] 39, 46, 47, 50
F_y	Coulomb force in y-direction [N] 39, 44, 46, 47, 50
F_z	Coulomb force in z-direction [N] 39, 46, 50
g_0	Standard acceleration due to gravity [ms^{-2}] 55
$I_{\mathbf{sp}}$	Specific impulse [s] 55
J	Cost function [-] 31
k	Size of total sphere population [-] 10
$k_{\mathbf{c}}$	Coulomb's constant [$8.987e9Nm^2C^{-2}$] 10
L	Separation distance [m] 53, 54
m	Size of sphere population on the tug [-] 10, 26
$m_{\mathbf{d}}$	Mass of debris [kg] 55
$m_{\mathbf{t}}$	Mass of tug [kg] 55
n	Size of sphere population on the debris [-] 10, 26, 31, 33
Q	Total charge residing on a body [C] 41
r	Distance [m] ix, 10, 15, 16, 22, 23, 24, 25, 26
$r_{\mathbf{p,t}}$	Distance from probe to tug [m] 21, 22
$r_{\mathbf{p,s}_i}$	Distance from probe to debris sphere *i* [m] 21
R	Sphere Radius [m] ix, 7, 15, 22, 23, 24, 25, 26, 30, 31, 40
$r_{\mathbf{sep}}$	Distance between tug and debris center of rotation [m] 11, 21, 22, 36, 49, 54
T	Thrust magnitude [N] 55
t	Time [s] 22, 55
u	Radial velocity [m/s] 55
v	Tangential (along-track) velocity [m/s] 55
$V_{\mathbf{d}}$	Electric potential of the debris [V] 14, 25, 26, 31
$V_{\mathbf{t}}$	Electric potential of the tug [V] 31
$x_{\mathbf{p}}$	Location of probe with respect to center of tug along x-direction [m] 21

$x_{\mathbf{s},i}$ Location of debris sphere *i* along x-direction [m] 21

$y_{\mathbf{p}}$ Location of probe with respect to center of tug along y-direction [m] 21

$y_{\mathbf{s},i}$ Location of debris sphere *i* along y-direction [m] 21

$z_{\mathbf{p}}$ Location of probe with respect to center of tug along z-direction [m] 21

$z_{\mathbf{s},i}$ Location of debris sphere *i* along z-direction [m] 21

α_i Scaling factor [-] 18

β_i Scaling factor [-] 18, 25

μ_0 Standard gravitational parameter of the Earth [398600 $km^3 s^{-2}$] 55

Φ Phase offset [s] 22, 23, 25, 26

ϕ Euler angle about z-axis [rad] 21

$\Phi_{\mathbf{p}}$ Potential measured by a probe [V] 14

$\Phi'_{\mathbf{p}}$ Normalized probe potential [-] 15, 17, 18, 22, 25

Φ Angle between LVLH and Spherical coordinate system [rad] 53

$\Phi_{\mathbf{D}}$ Debris potential [V] 25, 26

$\dot{\phi}$ Euler angle rate about z-axis [rad/s] 21, 44, 45

$\Phi_{\mathbf{M}}$ Measured potential signal [V] 31

$\Phi_{\mathbf{P}}$ Predicted potential signal [V] 31

$\Phi_{\mathbf{p_s},i}$ Probe potential due to debris sphere *i* [V] 17, 18, 26

$\Phi_{\mathbf{p_s},ij}$ Probe potential due to debris sphere *i* and tug sphere *j* [-] 19

$\Phi'_{\mathbf{p_s},i}$ Normalized probe potential due to debris sphere *i* [-] 22, 25

$\Phi_{\mathbf{T}}$ Tug potential [V] 26

ψ Euler angle about z'-axis [rad] 21

$\dot{\psi}$ Euler angle rate about z'-axis [rad/s] 21, 44, 45

θ Euler angle about x'-axis [rad] 21

Θ Debris rotation angle [deg] 38, 39

Θ Angle between LVLH and Spherical coordinate system [rad] 53

$\dot{\theta}$ Euler angle rate about x'-axis [rad/s] 21, 44, 45

$\zeta_{\mathbf{c}}$ Parameter describing the potential mismatch due to coupling between spheres [-] 18, 19

1

Introduction

Over the last centuries, the footprint of mankind in space has become more clear. As with any part of the world where people have been, trash is left behind, spoiling the local environment. Even though the effects of space pollution are not yet impacting the everyday life of people on Earth, this will be the case if no action is undertaken. Debris such as defunct satellites and spent rocket bodies, but also smaller parts like paint drops and bolts, or even space suits are orbiting around Earth[6]. As these bodies with velocities of several kilometers per second collide, multiple new pieces of debris are formed. A large part of these new pieces has enough energy to cause significant damage in its own turn, either to other pieces of debris, or to functioning satellites. This cascading effect of collisions is known as the Kessler syndrome, named after the physicist who studied the evolution of the debris population around Earth[7]. For some time, not much interest was taken in the problem, but after the catastrophic collision of the Iridium 33 and Cosmos 2251 satellites, as well as the anti-satellite missile test breaking up the Fengyun 1-C satellite, it became clear that action is required. An overview of the number of cataloged objects orbiting around Earth from the first launch in 1957 of Sputnik through the beginning of the year 2017 can be found in Figure 1.1[1]. The large increment in objects after 2007 is due to the Fengyun break-up, while the Iridium-Cosmos collision drastically increased the population in 2009.

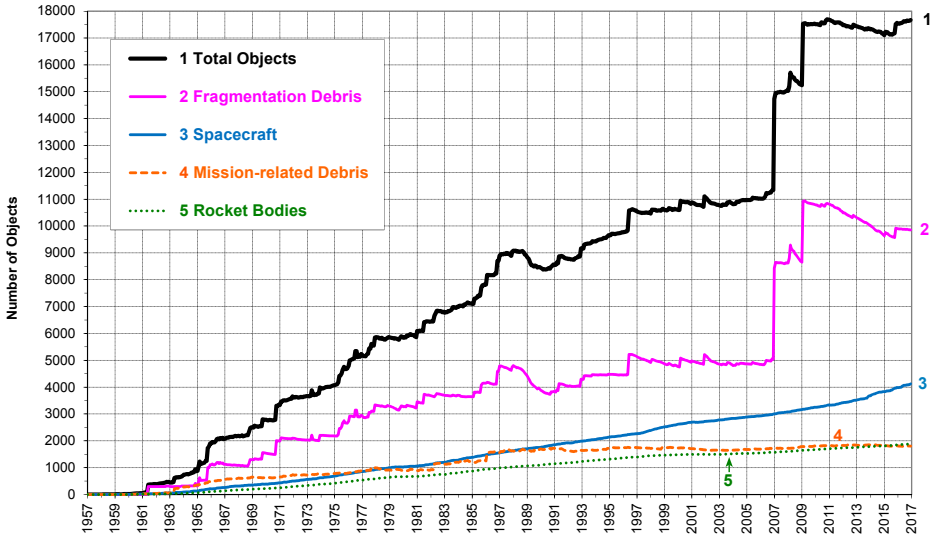

Figure 1.1: Monthly number of cataloged objects in Earth orbit, as obtained from the Orbital Debris Quarterly News[1].

In order to maintain a sustainable space environment, research has shown that 5-10 (large) pieces of debris have to be removed per year[8,9]. Several methods for active debris removal have been identified

and discussed in the literature study preceding this thesis[10]. Methods such as grappling[11], throwing nets[12] and harpoons[13] are promising and show high Technical Readiness Levels. The drawback of these mechanisms however, is that an uncooperative piece of debris can destroy the tether, create secondary debris due to the impacting harpoon and in general introduce extensive attitude and orbit control issues. Methods that do not require a mechanical link and thus reduce these risks are developed in the form of the Ion-Beam Shepherd[14,15] and most notably the Electrostatic Tractor (ET), as proposed by Moorer Jr and Schaub[16,17].

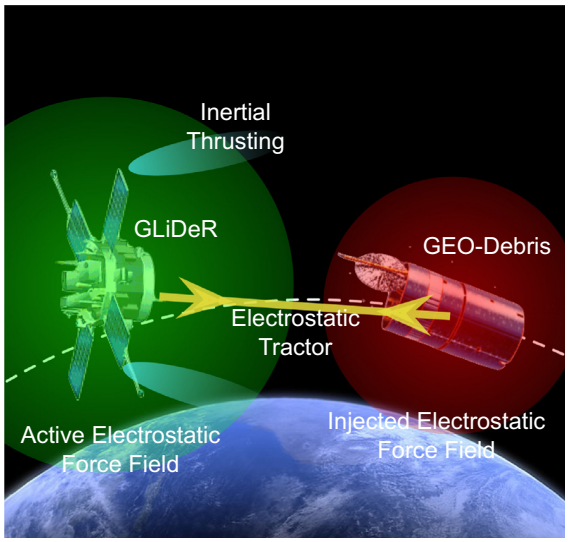

Figure 1.2: Graphical representation of the geosynchronous large debris reorbiter (GLiDeR) concept, as obtained from Schaub and Sternovsky[2].

By means of an electron gun, electrons can be transferred from a dedicated spacecraft onto a piece of debris. As the debris charges negatively and the spacecraft, which will be called the 'tug' from here onwards, charges positively, a Coulomb force is generated between the bodies. This force can then be used to control the orbit of the debris, such that it can be moved to a less critical regime[18]. A graphical representation of ET concept can be found in Figure 1.2. Especially in Geostationary Orbit (GEO), where the application of the tractor would be, a lot of critical space assets reside, as the majority of all insured satellites is in this region[19]. In order to reorbit the debris, the most effective and safe tug-debris orientation is that where the tug orbits ahead of the debris and 'pulls' this body towards it. Such an orientation is especially beneficial when the Coulomb force is over-predicted; in which case the tug will simply move away from the debris, decreasing only the ET performance in terms of reorbiting time. When the force is under-predicted however, the debris closes in with the tug and a collision can be the result. For this reason, knowledge about the electrostatic behavior of the debris must be obtained in a real-time manner, such that these scenarios can be avoided[5].

Different methods exist that can be applied to model the electrostatic behavior of a charged body. A very fast method is to approximate the bodies as point charges, from which the Coulomb force can be found in less then a second of computation time. The drawback of this method, is the very low accuracy, introducing large force estimation errors. A method that can model the charge distribution, and Coulomb force, very accurately is the Finite Element Analysis (FEA), where the geometries are split into very fine cells. For each of these cells, the physics governing electrostatic interaction are evaluated, resulting in a high-fidelity model. High accuracy comes at the price of high computational costs however. As a FEA to model the electrostatic behavior of the debris can take up to hours, even without taking into account (varying) plasma conditions, a faster modeling technique is required for real-time application. As a solution, the Multi-Sphere Method (MSM) has been proposed by Stevenson and Schaub, which uses a population of spheres with a charge residing in the center to approximate the debris. By doing so, computation times are drastically reduced with respect to FEA simulations, while still allowing for (relatively) accurate modeling[3]. A schematic overview of the accuracy and computational time of the methods described can be found in Figure 1.3.

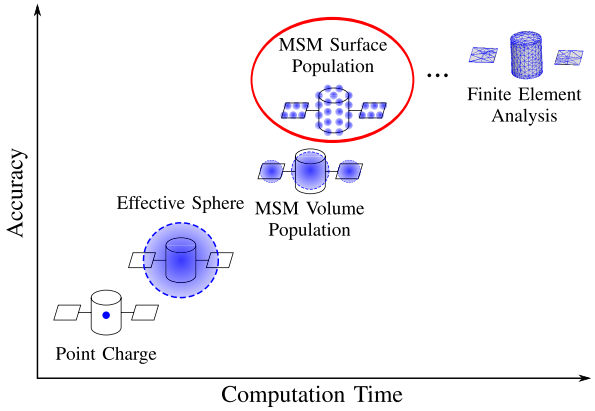

Figure 1.3: Schematic overview of accuracy versus computational cost for various (electrostatic) modeling techniques, as obtained from Stevenson and Schaub [3].

Some recent advances in MSM modeling are as follows. Using a MSM model, debris detumbling studies are possible [21,22]. The benefit of detumbling includes easier interaction for on-orbit servicing, allowing for other removal techniques such as grappling, and better force predictions. Furthermore, optimal sphere placement has been researched, as to increase the accuracy of the MSM simulations [3]. Each of these models and techniques however, require knowledge of the debris potential and in general, its shape or electrostatic characteristics. In order to determine the potential in-situ, the Remote Sensing for Electrostatic Characterization (RSEC) method has been proposed [23].

By measuring the potential in space over a rotation of the debris, information is inferred about the characteristics of the body. By placing MSM spheres, a model is created which resembles the measured potential best. This best-fitting MSM model can then be used to determine the state of the debris at any time during its orbit and application of the ET. A graphical representation of this method is displayed on the cover. As the RSEC method requires minimal knowledge of the body in question, it can potentially be used to determine the charge of asteroids as to asses risks during rendezvous with these objects [24]. Other applications of the method include studies on dust transfer over the lunar surface, which is governed by charging processes, and in general inferring information about the charged state of a body before conducting physical contact [25,26].

Measuring electric potentials in space with probes is a well proven technique. The first missions to measure kilovolt potentials were the ATS-5 and Scatha missions [27,28]. The latter showed that especially during eclipse, spacecraft can charge to very large potentials, introducing discharge events when not designed for [29]. The current study evaluates debris specifically at GEO, where active charging can be performed with very low levels of electrical power [2]. Additionally, at this specific altitude regime, nominal values of the Debye length are in the range of over 200 meter [30]. The Debye length is the region over which ions and electrons in the ambient plasma rearrange itself as to counter external electric fields. Evaluating debris removal with the ET at GEO allows therefore for electric fields and forces between bodies within this shielding distance. Ongoing research concerned with application of the electrostatic tractor in orbit regimes with lower Debye lengths by using pulsed beams is performed by Hughes and Schaub [31]. This research assumes a constant charging process and negligible influence of the ambient plasma on the electric field around the bodies of interest.

Research Objective

The developed RSEC method, shows a promising solution to determine the electrostatic characteristics of uncooperative bodies, of which not much information is known. However, the current state of the method limits the application to planar geometries and rotations about the out-of-plane axis [23]. Furthermore, validation of the method with data external to the developed model is still to be performed. In order to progress this method, the following research objective is therefore established:

Develop and validate a model that is able to characterize the electrostatic behavior of a three-dimensional, tumbling, charged object in space, in a real-time and accurate manner.

More specifically, this relates to the following requirements on the model:

1. The model shall have real-time applicability
2. The accuracy of the model shall be better than a simple 2-sphere model
3. The model shall be able to evaluate full spatial geometries and multi-axis rotations

By meeting these requirements, a method is established that can be used to create a fast and reliable estimate of the charged state of a uncooperative body, as required for successful application of the ET concept.

Mission Scenario

The application scenario for the RSEC method as envisioned in this study, is the following. Assume there is a piece of debris orbiting Earth in GEO. After identifying this object as a high-risk and high-priority target, a dedicated debris removal satellite is appointed the task of re-orbiting this piece of debris to a graveyard orbit. After closing in with the target, the satellite performs a formation flying maneuver to map the geometric features of the debris, as well as its Moment of Inertia (MoI) and rotation rates. In Figure 1.4, this part of the mission is displayed in the *Simulated In-situ Debris Measurements* block. Using a form of ranging, such as Light Detection and Ranging (LiDAR), the distance with respect to the Center of Rotation (CoR) of the debris is determined. The tug satellite then beams a current of electrons onto the debris, causes the former to charge up positively and the latter negatively. The resulting coulomb force can then be used to attract the debris, which is known as the ET. By thrusting away from the debris at the same time, the tug maintains a safe separation distance, while the total tug-debris system is raised to a higher orbit.

During the application of the ET, potential probes located at the end of booms suspended from the tug register the ambient potential field over the course of at least a full tumble of the debris. By applying the RSEC method, a MSM characterization of the debris is obtained, which can be used to infer the force and torque in the system due to the ET. This is performed by creating a state vector consisting of parameters describing the MSM model. Using the inferred rotation rate of the debris, a rotating MSM can be obtained. For each of the rotation states, the charge distribution on tug and debris can be determined using the inverted capacitance matrix. From the charge distribution, the force and torque on the two-body system can be determined as well as an expected potential signal. By comparing this potential signal with potential measurements from the probes, i.e. the cost function, the location of the spheres on the MSM model can be optimized. This iteration can be found in the *Characterization / Optimizations Model* block in Figure 1.4. After finding the best-fit MSM model, potential measurements and observations of the orientation of the debris can be used to estimate the force and torque at any instance of time. Based on these parameters, appropriate thrust levels can be selected on the tug as to ensure a safe and robust application of the ET, according to the control law depicted in the block *Error Analysis / Model Validation*. Additionally, the torque estimates could be used to determine the required modulation of the electron beam such that detumbling of the debris can be performed. As described before, benefits of detumling are easier interaction for on-board servicing, better control of the Coulomb force and more stable reorbiting maneuvers, and allowing for other debris removal interactions. This report does not cover the influence of torque though, as the focus lies predominantly on the Coulomb force used to attract the debris.

In order to validate the model, the application scenario of the RSEC method is as follows. Data obtained during rendezvous with the debris, such as MoI, CoR and rotation rates as well as pre-flight calibration data of the tug, are fed into the RSEC model. In this study, as will be shown later, the torque has little influence on the debris dynamics and therefore the influence of torque and MoI is neglected. What in application with a real mission scenario would be the potential measured by the probes, is now determined with use of a FEA numerical simulation. Based on these measurements, the RSEC model constructs a best-fit MSM model of the debris. For simple geometries and one axis rotations, the rotation rate can be resolved. The best-fit MSM model is then used to determine the force and

torque on the system. This part of the model can be found in the *Finite Element Analysis* block of Figure 1.4. Additionally, a Surface Multi-Sphere Method (SMSM) model is constructed based on the results from the FEA simulations, as to allow for validation with more complex rotations. Comparing the estimated Coulomb force with the output from the FEA analysis, the error of the RSEC method can be determined. Using the control law developed by[5] and the found mis-prediction, a mass and re-orbiting time envelope can be constructed. This part of the *Error Analysis* is used to asses the RSEC method on its applicability and accuracy.

This report follows roughly the same structure as described in Figure 1.4. Note that the relevant chapter for each block can also be found in this model flow diagram. The characterization model is described in Chapter 2, where the equations governing the MSM model are addressed. For some specific cases of debris and tug geometries and rotations, model simplifications can be performed. These simplifications and their application are discussed in Chapter 3. As one of the most important parts of the RSEC method is optimization, Chapter 4 addresses this issue. In this chapter, different strategies and their benefits are discussed. After discussing the characterization and optimization model, the FEA set-up is elaborated upon in Chapter 5. This chapter describes different options for generating validation data as well an intermediate SMSM model that can be used to create multi-axis tumbling simulations. After obtaining the validation data, a numerical simulation is described in Chapter 6, where the RSEC method is put to the test. The results are analyzed and the influence of varying model parameters is evaluated. Lastly, this chapter describes the effect of the model accuracy on reorbiting time and fuel cost. A final chapter on recommendation and conclusions based on this work can be found in Chapter 7.

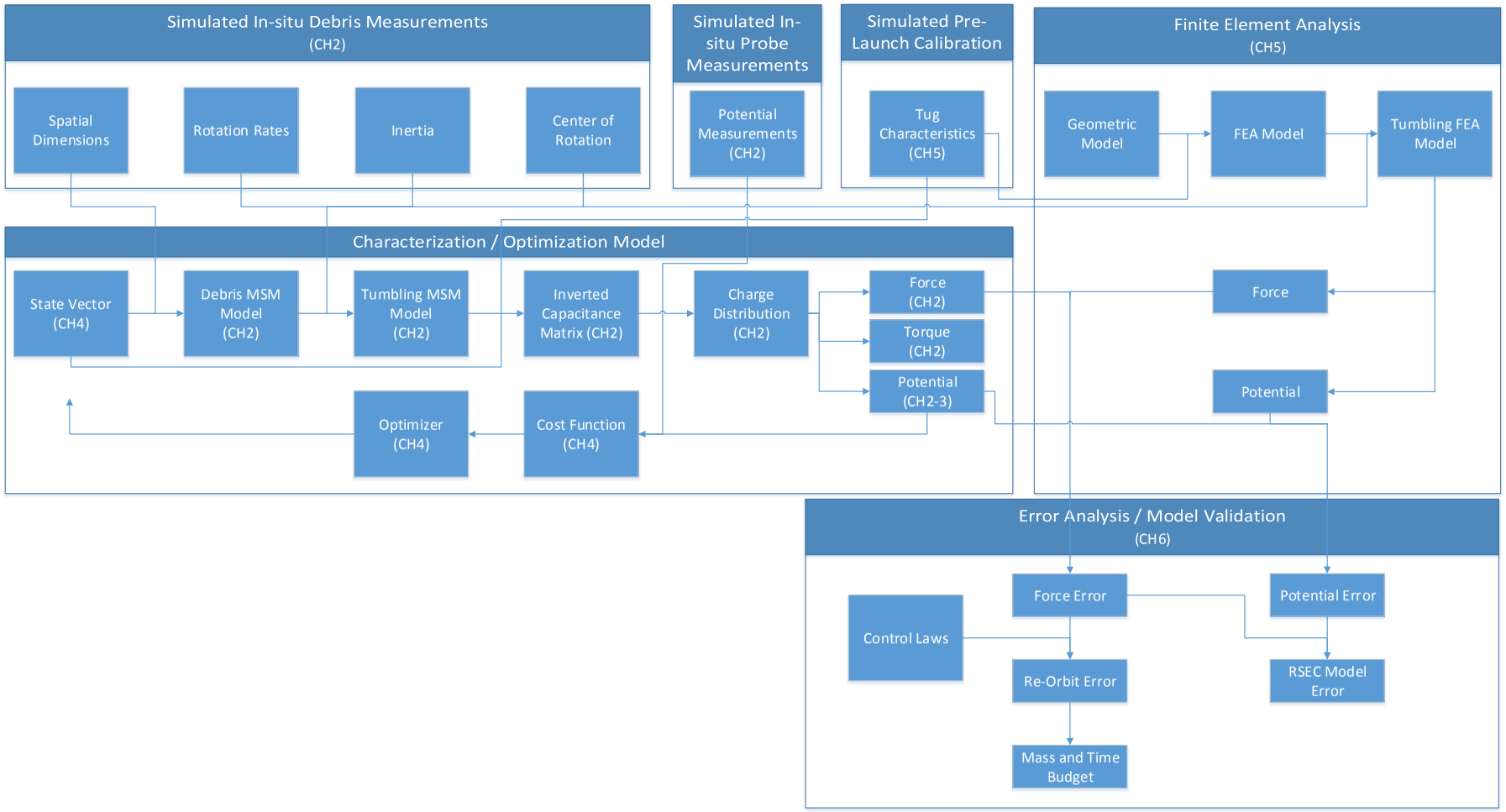

Figure 1.4: Flow diagram of the developed debris characterization model, including the relevant chapters for detailed information.

2

Multi-Sphere Method Model Setup

For safe application of the Electrostatic Tractor (ET), it is required that the charge distribution over the debris is characterized multiple times over a full orbital revolution. Performing a Finite Element Analysis (FEA) for a full orbit can easily take days, if not more. The beauty of the Remote Sensing for Electrostatic Characterization (RSEC) method is that it depends on the Multi-Sphere Method (MSM), which can be used to determine the electrostatic characteristics in a much shorter time[3].

This chapter provides an overview of the implementation of the MSM within the RSEC method, for general three-dimensional (spatial) application. The relevant reference frames, propagation of the sphere's orientation over time and equations to determine potential, force and torque, are discussed in the coming sections. This chapter therefore is an extension to the work performed by[23], where only planar characterization was discussed.

2.1. The Multi-Sphere Method

In stead of dividing the geometrical model of the debris in a number of finite volumes and analyzing the appropriate equations for each and every of these cells, as performed by a FEA, the approach of the MSM is as follows. Multiple spheres are distributed over either the volume or surface of the bodies that need to be characterized. The electrostatic behavior then results from a point charge located in the center of each of these spheres. The total set of spheres represents the electrostatic characteristics of the evaluated body. An extended overview of the MSM can be found in Stevenson and Schaub[3,20].

Every sphere is characterized in the Local Vertical Local Horizontal (LVLH), or Hill reference frame $\mathcal{H}$, with the origin attached to the center of mass of the tug. This reference frame is defined with the elementary vectors $\hat{\mathrm{o}}_r$ in the radial direction, $\hat{\mathrm{o}}_\theta$ in the along-track direction, and $\hat{\mathrm{o}}_h$ completing the right-handed frame. An illustration can be found in Figure 2.1.

In order to minimize collision probability and optimize the efficiency of the ET, it is assumed the tug orbits ahead of the debris in the along track direction[5]. The spheres can then be represented by their coordinates (x, y, z) and radii R. Here the assumption is made that due to the close proximity of the bodies, the curvature of the orbit can be neglected and the debris lies in the LVLH plane. Furthermore, the electric potential of the whole collection of spheres on the debris is characterized by V_{deb}. An overview of these parameters can be found in Figure 2.2.

Notice that in the rest of this report the LVLH reference frame is used, unless specified otherwise.

2.2. Tumbling Motion using Modified Rodriguez Parameters

In order to simulate the tumbling motion of the debris, a formalism has to be chosen to represent the orientation of the MSM spheres at any instance of time. A common problem in representing the

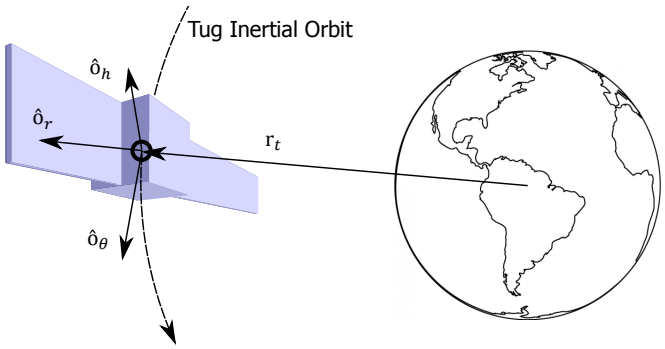

Figure 2.1: Illustration of the local vertical local horizontal (LVHL) reference frame with respect to the tug inertial orbit.

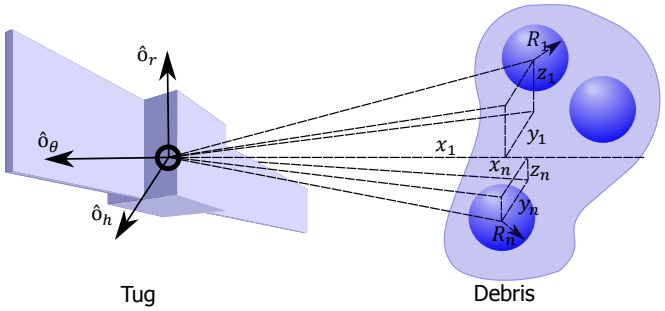

Figure 2.2: Illustration of the local vertical local horizontal (LVHL) reference frame with respect to the tug and debris.

orientation of a body within a reference frame, is that multiple sets of angles can be used to describe the same orientation, or that for some angles singularities are introduced in the transformation equations. Characterized by the limited amount of singularities over a full tumbling revolution, its application in estimation theory and well-formulated definition, Modified Rodrigues Parameters (MRPs) are chosen to represent the orientation of the spheres on the debris. The following section describes how the sphere locations can be propagated over the rotation period of the debris by using these parameters.

By defining the principle rotation axis as $\bar{e}$ and the principle rotation angle as ϕ, the MRP vector σ can be written as[32]:

$$\sigma = \tan\left(\frac{\phi}{4}\right)\bar{e}; \tag{2.1}$$

Due to the singularities of the MRP vector at ± 360 degrees, a conversion to the so called "shadow set" σ^S has to be made following Algorithm 1.

Algorithm 1 MRP shadow set conversion

```
procedure Shadowset
    σ ← σ^S
    if ||σ|| ≥ 1 then
        σ^S ← −σ/(σ^T σ)
        σ ← σ^S
    end if
end procedure
```

The Direction Cosine Matrix (DCM), represented by the parameter C, can then be obtained by converting

the MRP vector with the following equations[33]:

$$C = \frac{1}{1+\sigma^{\mathsf{T}}\sigma}\begin{bmatrix} 4(\sigma_1^2-\sigma_2^2-\sigma_3^2)+\Sigma^2 & 8\sigma_1\sigma_2+4\sigma_3\Sigma & 8\sigma_1\sigma_3-4\sigma_2\Sigma \\ 8\sigma_2\sigma_1-4\sigma_3\Sigma & 4(-\sigma_1^2+\sigma_2^2-\sigma_3^2)+\Sigma^2 & 8\sigma_2\sigma_3+4\sigma_1\Sigma \\ 8\sigma_3\sigma_1+4\sigma_2\Sigma & 8\sigma_3\sigma_2-4\sigma_1\Sigma & 4(-\sigma_1^2-\sigma_2^2+\sigma_3^2)+\Sigma^2 \end{bmatrix} \tag{2.2a}$$

$$\Sigma = 1-\sigma^{\mathsf{T}}\sigma \tag{2.2b}$$

By determining the DCM for every rotation angle, the position of the spheres on the debris in the LVLH reference frame can be determined with Equation 2.3

$$[x,y,z]_\phi^T = C(\phi)[x,y,z]_0^T \tag{2.3}$$

where the initial position of each sphere is given by $[x,y,z]_0^T$.

In the application scenario of the ET, as described in the introduction, it is assumed that the tug is actively performing attitude control. Since the inter-body Coulomb force introduces a torque on both bodies, the tumbling rate of the debris is not constant. This effect can be exploited to detumble the debris, as discussed by Bennett *et al.*[21,22]. Using a small time step Δt, the tumbling motion can be propagated by applying Algorithm 2.

Algorithm 2 MRP propagation

1: **procedure** Propagation
2: $\sigma \leftarrow \sigma + \Delta\sigma\Delta t$
3: **while** $t \leq t_{\text{final}}$ **do**
4: $I_{\text{i}} \leftarrow C * I_{\text{b}} * C^T$
5: $\Delta\sigma \leftarrow 0.25B\omega$
6: $\sigma \leftarrow \sigma + \Delta\sigma\Delta t$
7: $\alpha \leftarrow \text{inv}(I_{\text{i}}) * \text{T}_{\text{d}}$
8: $\omega \leftarrow \omega + \alpha\Delta t$
9: **end while**
10: **end procedure**

The parameters I_{i} and I_{b} in this algorithm represent the debris inertia matrix in the LVLH and body reference frame respectively. Furthermore, the differential kinematic relation on line 6 depends on the matrix B given by Equation 2.4 to transform the body angular velocity ω into the derivative of the MRP vector $\Delta\sigma$[33].

$$B = \begin{bmatrix} 1+\sigma_1^2-\sigma_2^2-\sigma_3^2 & 2(\sigma_1\sigma_2-\sigma_3) & 2(\sigma_1\sigma_3+\sigma_2) \\ 2(\sigma_2\sigma_1+\sigma_3) & 1-\sigma_1^2+\sigma_2^2-\sigma_3^2 & 2(\sigma_2\sigma_3-\sigma_1) \\ 2(\sigma_3\sigma_1-\sigma_2) & 2(\sigma_3\sigma_2+\sigma_1) & 1-\sigma_1^2-\sigma_2^2+\sigma_3^2 \end{bmatrix} \tag{2.4}$$

Applying Algorithm 2 for a few full revolutions shows that the tumbling rate can be assumed constant over the typical measurement period of the RSEC method, as the torque on the debris T_{d} and consequently the body angular acceleration α are very small. More elaboration on the effects of force and torque are described in Section 2.5.

2.3. Charge Distribution during Tumbling Motion

During the tumbling motion of the debris, charge moves around in both tug and debris due to the presence of the other body. In this study, the bodies are assumed perfectly conducting, such that the charge is allowed to move uniformly over the whole surface of the respective body. Due to the charge re-distribution, the potential field around the two bodies changes over time. This ambient potential field is also influenced by the electric field around the Earth and the plasma properties, but in this study a

perfect vacuum around the bodies is assumed with no potential field other than that induced by the tug and debris. A source of potential variation of the bodies is also the varying space weather. However, as the time scale over which this variation happens in Geostationary Orbit (GEO) is in the order of hours[30], a constant debris potential can be assumed[34]. In order to determine the structure of the ambient potential field, the charge distribution represented by the MSM spheres has to be evaluated.

For every sphere k in the tug-debris system, the distance with respect to the other spheres can be represented with the parameter r. The relation between the potential ϕ and charge a can then be found using Equation 2.5, where k_c represents Coulomb's constant[23,34].

$$\begin{bmatrix} q_1 \\ q_2 \\ \vdots \\ q_k \end{bmatrix} = \frac{1}{k_c} \begin{bmatrix} 1/R_1 & 1/r_{2,1} & \dots & 1/r_{k,1} \\ 1/r_{1,2} & 1/R_2 & \dots & 1/r_{k,2} \\ \vdots & \vdots & \ddots & \vdots \\ 1/r_{1,k} & 1/r_{2,k} & \dots & 1/R_k \end{bmatrix}^{-1} \begin{bmatrix} \phi_1 \\ \phi_2 \\ \vdots \\ \phi_k \end{bmatrix} \tag{2.5}$$

The center matrix of Equation 2.5 is also known as the inverse capacitance matrix. It can be divided into four quadrants, as shown in Equation 2.6.

$$\left[C^{-1}\right] = \begin{bmatrix} C_{\mathrm{t}}^{-1} & C_{\mathrm{t,d}}^{-1} \\ C_{\mathrm{d,t}}^{-1} & C_{\mathrm{d}}^{-1} \end{bmatrix} \qquad C_{\mathrm{d,t}}^{-1} = C_{\mathrm{t,d}}^{-1\,\mathrm{T}} \tag{2.6}$$

In this form, the entries C_{t}^{-1} and C_{d}^{-1} represent the tug and debris self capacitance respectively. The mutual capacitance is given by $C_{\mathrm{t,d}}^{-1}$, which is the transpose of $C_{\mathrm{d,t}}^{-1}$. By rewriting the equations in the form of quadrants, a block matrix inversion can be applied, as described in Equation 2.7[35].

$$\begin{bmatrix} A & B \\ C & D \end{bmatrix}^{-1} = \begin{bmatrix} (A - BD^{-1}C)^{-1} & -A^{-1}B(D - CA^{-1}B)^{-1} \\ -D^{-1}C(A - BD^{-1}C)^{-1} & (D - CA^{-1}B)^{-1} \end{bmatrix} \tag{2.7}$$

The benefit of performing a block matrix inversion instead of regular matrix inversion, is that the quadrants can be individually evaluated. By assuming that the tug characteristics, i.e. the location and radii of the spheres on the tug, are known from calibration, the tug self capacitance can be determined a-priori of the RSEC evaluation. Furthermore, as the spheres on the debris all rotate about the Center of Rotation (CoR), the debris self capacitance stays constant over time as well. Therefore only the mutual capacitance has to be evaluated with the block inversion at every time step Δt, reducing computational cost.

2.4. Potential, Force and Torque Calculations

After evaluating the charge distribution on the debris and tug, the potential at the location of the probes can be determined. Assuming the influence of the charge located within the probe is negligible, the potential at the location of the probe can be calculated with Equation 2.8.

$$\Phi_{\mathrm{p}} = k_c \sum_{i=1}^{k} \frac{q_i}{r_{i,\mathrm{p}}} \tag{2.8}$$

As the debris tumbles, the potential at the probe location varies and therefore a potential curve can be constructed over the full rotation of the debris. Furthermore, the Coulomb force F introduced by the ET between the debris and tug can be calculated. This inter-body force depends on the summation of the charge product of all spheres n on the debris and m on the tug, divided by their separation. The equation for this force, as shown in Equation 2.9, is an adaptation of the equation given by Stevenson and Schaub with a double summation[34] over all spheres.

$$\mathrm{F_c} = k_\mathrm{c} \sum_{j=1}^{m} \sum_{i=1}^{n} \frac{q_i q_j}{r_{i,j}^3} \mathrm{r}_{i,j} \tag{2.9}$$

Similarly, the torque T on both debris and tug can be found by introducing the cross product between the separation vector of the spheres and the vector from the spheres with respect to the corresponding CoR.

$$\mathrm{T_d} = k_\mathrm{c} \sum_{j=1}^{m} \sum_{i=1}^{n} \frac{q_i q_j}{r_{i,j}^3} \mathrm{r}_{i,j} \times \mathrm{r}_i \tag{2.10}$$

2.5. Influence of Force and Torque on Potential Measurements

For a typical mission scenario, a large piece of debris has to be removed. Typical Coulomb force magnitudes are in the mili-Newton range, and therefore also torque magnitudes are small. Where over multiple weeks or even months, the torque has a direct influence on the angular momentum of the debris, over short periods, the influence is negligible. For a simple cylindrical geometry of debris and spherical tug, where the mass of the tug is 500 kg, and that of the debris $1000kg$, Bennett and Schaub has shown that active detumbling can be performed over a timescale of hundreds of hours[22]. Therefore the influence of torque on debris rotation can be neglected in the models evaluated over a short time period. As the potential signals are obtained for a single, or at most a few, revolutions of the debris, the resulting potential signal can be considered to repeat itself over these rotations without deviation.

The effect of the Coulomb force on the inter-body separation distance r_{sep} will be neglected in the numerical simulations discussed in this report as well. As the primary incentive for application of the ET is to accelerate the debris in order to reorbit the body, the tug has to maintain a stable separation during this period. In order to do so, the tug will apply a thrust in the along track direction in order to maintain the separation and provide an optimal reorbit maneuver. Therefore it is assumed that the influence of varying distance between the bodies on the potential measurements is negligible.

3

Decoupled Sphere Model

Optimizing the set of parameters described by the Multi-Sphere Method (MSM) model based on potential measurements introduces a fundamental problem. The electric potential of a fixed point in space (in the Local Vertical Local Horizontal (LVLH) reference frame) depends on the radii and potential of, and distance to, the set of MSM spheres. As these parameters are coupled via the capacitance matrix, multiple solutions exist that result in roughly the same potential curve. Not all of these solutions provide the optimal MSM geometry in terms of force prediction though. This chapter evaluates the influence of the parameters on the probe potential measurements, such that more insight is gained in possible bottlenecks and advantages of the Remote Sensing for Electrostatic Characterization (RSEC) method. The first two sections describe the effect of varying the debris potential and radii respectively. Based on amongst others the conclusions drawn from these two sections, a decoupled sphere model is introduced in Section 3.3. It is found that for tug geometries that can be represented by a single sphere on the tug, a (semi)-analytical approach can be taken to find the potential curve without the need for an sequential computation of the potential for each time step. This methodology is elaborated upon in Section 3.6 for a spatial debris geometry and rotation, whereas Section 3.5 describes the approach for planar debris geometries and rotations. In case the tug cannot be approximated by a single sphere, decoupling of parameters is still possible, as described in Section 3.4. A graphical overview of the relation between the sections can be found in Figure 3.1.

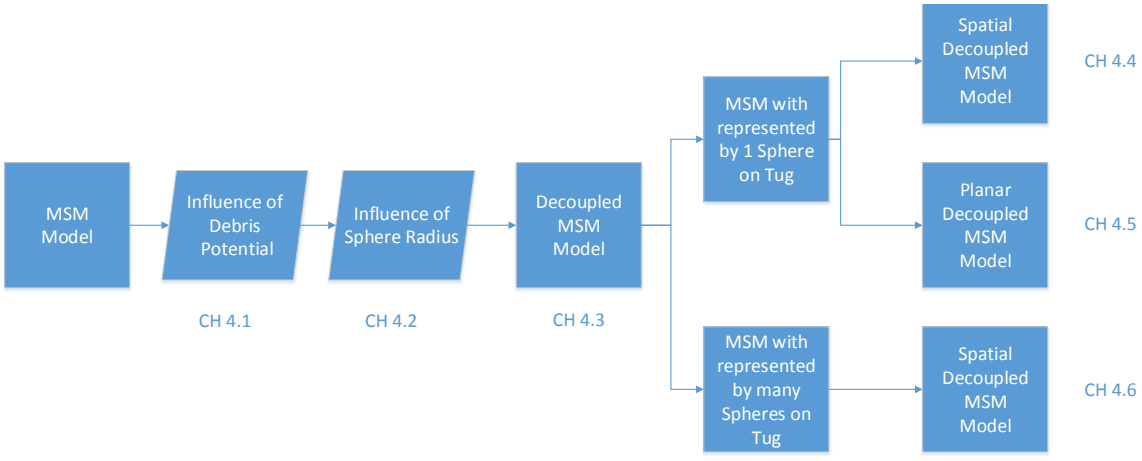

Figure 3.1: Flow diagram describing the structure of the chapter.

Based on the simplifications described in this chapter, some conclusions are drawn, which aid in developing a sense of how the RSEC could be applied and provide an advantage over the conventional, coupled, methodology.

3.1. Influence of Debris Potential on Probe Measurements

In Chapter 2 the methodology of obtaining probe potential measurements from a MSM model is described. For the following analysis, such a model was constructed with a random distribution of 14 spheres representing some arbitrary piece of debris. The debris spheres are contained within a square box with sides of 10 meter, centered at the Center of Rotation (CoR) (15,0,0). An overview of such a geometry is given in Figure 3.2.

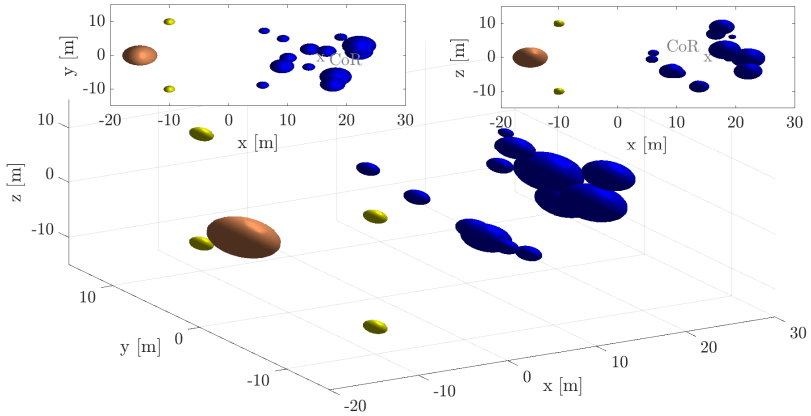

Figure 3.2: Overview of the model used for analysis, with in brown the tug, yellow the probes and blue the (randomly located) debris.

The tug is held to a fixed positive kilovolt potential, while the debris negative potential is varied. As the debris becomes increasingly negatively charged, the potential measured close to the tug (which initially assumed positive values) decreases. This behavior can be observed in the left-hand side of Figure 3.3, where the potential Φ_p registered by four distinct probes in between the tug and debris is evaluated over time. Note that one full revolution of the debris is observed.

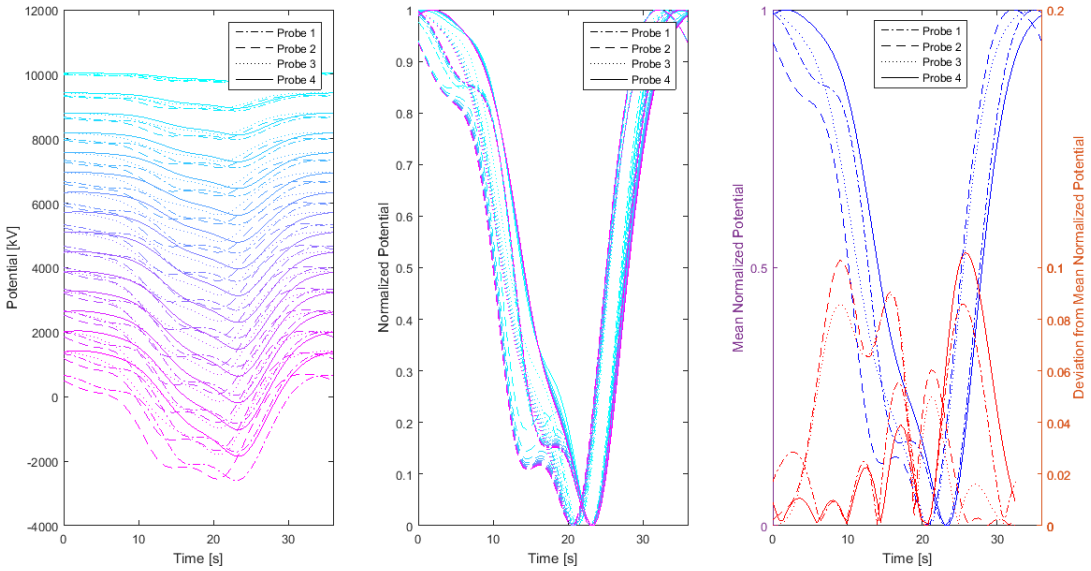

Figure 3.3: Normalization of measurement data obtained for a range of debris potentials, ranging from 0 (blue) to -70 kV (purple) at four distinct probe locations. The two plots on the right side shows the mean normalized probe signal and the error of each normalized signal in respect.

From this figure, it can be observed that as the potential of the debris V_d is increased negatively from

0 to $-70kV$, the peaks and valleys in the signal become more distinct. The locations of these features on the x-axis remains constant though, as the geometry of the debris is kept constant over the varying signals.

These signals can then be normalized to unity by applying Equation 3.1. The resulting normalized probe potentials Φ'_p are displayed in the middle of Figure 3.3.

$$\Phi'_p = \frac{\Phi_p - \Phi_{p_{min}}}{\Phi_{p_{max}} - \Phi_{p_{min}}} \tag{3.1}$$

By normalizing the potential, it becomes clear that even for such a large debris potential range, the general shape of the potential signal stays constant. In order to determine how much the signal differs over the potential range, the mean value of the variation of potential signals is obtained for each probe at every time step. These curves are displayed in the right-hand side of the figure in blue. For each of the probes, the maximum deviation (either for 0 or -70 kV) of the signal with respect to this mean is determined. These curves can be found in red in the same plot. By taking such a close look at the maximum deviation of a signal when varied by a certain potential, it becomes clear that indeed the potential magnitude has minor effect on the shape of the normalized potential Φ'_p. The only significant effect it has is to the absolute measured potential level. Decoupling of the debris potential from the set of parameters describing the MSM model seems therefore a feasible option.

3.2. Influence of Debris Radius on Probe Measurements

A similar approach as in the previous section is taken to study the influence of debris radius on probe potential measurements. A simple two-sphere model is created, with the first sphere representing the tug at a potential of 30 kilovolt, and the second representing the debris which is rotating about a fixed CoR. An overview of this geometry can be found in Figure 3.4.

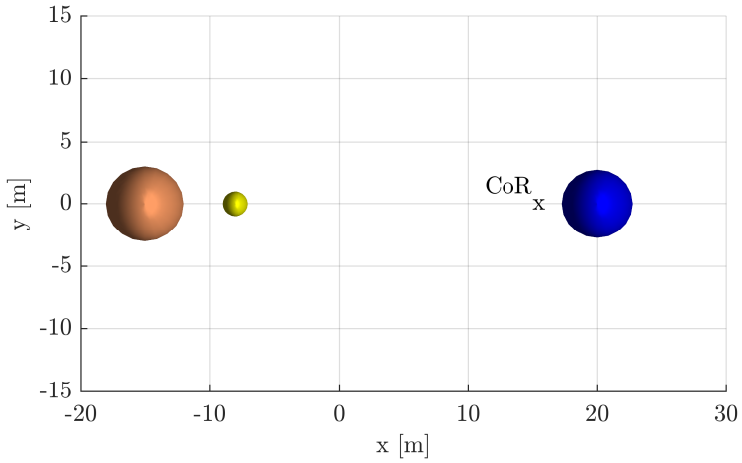

Figure 3.4: Two-sphere model with in brown the tug, yellow the probe and blue the debris, rotating about the CoR.

In order to study the behavior of the observed potential signal, the debris radius R and distance to the CoR (r) are varied. In the left-hand side of Figure 3.5, these parameters are each varied between two values, resulting in three distinct probe signals.

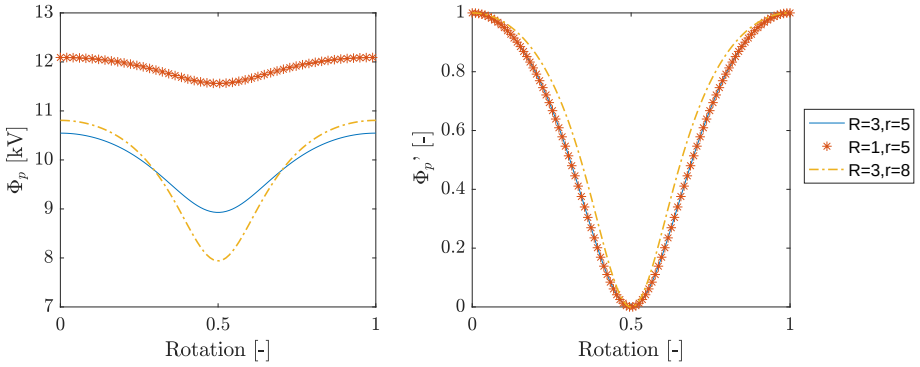

Figure 3.5: Measured potential for a variation of debris distance to the CoR and radius as well as the normalized version of this potential signal over a full rotation.

On the right-hand side of this figure, the same signals are given over a full rotation but normalized to unity scale. From this figure, it becomes clear that at least for a simple model like this, the normalized signal is independent of sphere radius. Another observation can be made from the normalized data. As the distance of the debris with respect tot the CoR increases, the Full Width at Half Maximum (FWHM) of the signal decreases. In order to evaluate this relationship further, the distance r is varied between approximately 0 and 15 meters. The measured potential near the debris and its normalized versions are given in Figure 3.6.

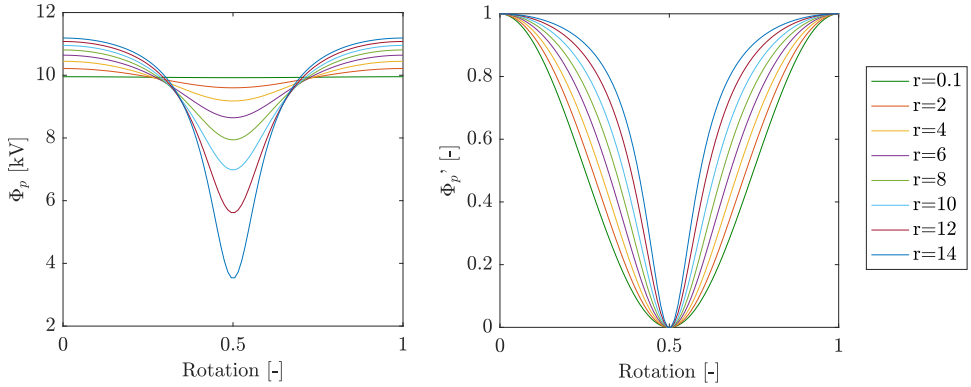

Figure 3.6: Measured potential for a variation of debris rotation radius as well as the normalized potential signal over a full rotation.

Next to the decrease in FWHM of the normalized signal, also the limit of the signal can clearly be recognized. For a distance close to zero, so almost no rotation at all, the signal approximates a pure cosine function.

3.3. Decoupled Single Sphere Model

The previous two sections have shown indication that normalizing the measured potential of a probe can reduce the number of parameters that influence a sphere optimization problem. The parameters describing the influence of a single sphere have been evaluated, so the next step is to evaluate the influence of spheres on each other. A simple model is constructed, consisting of three spheres making up the tug and three spheres of unity radius rotating about the CoR making up the debris. A graphical representation is given in Figure 3.7. Furthermore, the tug is initially at 30 kilovolt potential, while the debris is at negative 30 kilovolt potential.

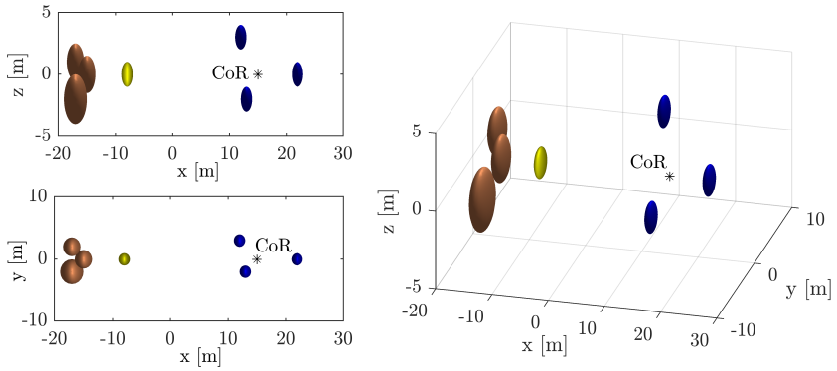

Figure 3.7: Graphical representation of the multi-sphere geometry, with in brown the tug, yellow the probe and blue the debris which is tumbling about the CoR.

The spheres are now rotated a full revolution around some arbitrary axis through the CoR and the potential at a probe location is registered and normalized. This signal Φ'_p is given in the lower left of Figure 3.8. Since there exists evidence that the potential of the spheres does not contribute extensively to the normalized potential, the tug is now given a 1 volt potential and the debris a negative 1 volt potential. Furthermore, the model is reduced by two debris spheres, such that a 'single sphere' system is created; meaning that only one debris sphere is revolving around the CoR. The resulting probe potential $\Phi_{p_{s,i}}$ is displayed in the top left figure as a function of rotation angle. The same analysis is performed for the two other spheres on the debris, as indicated by the top middle and top right plot. Now these three 'single sphere' potentials are added and normalized, as is displayed in the bottom middle figure. In the bottom right figure, the difference between the normalized potential of three debris spheres and the normalized potential of the spheres summed is given.

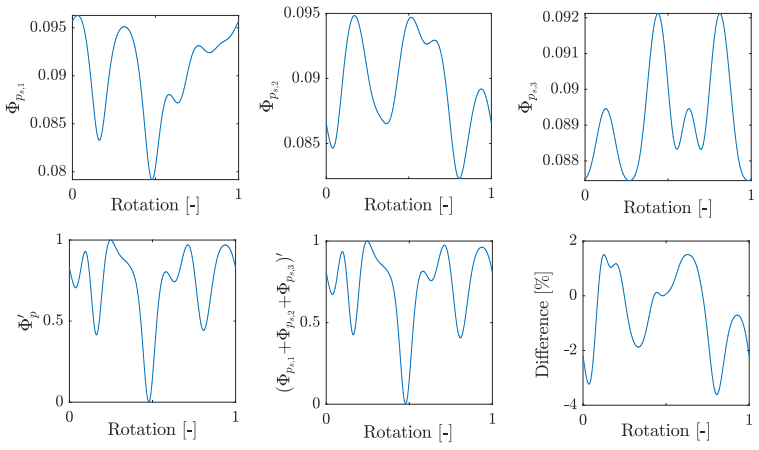

Figure 3.8: Comparison of normalized probe measurements for a combination of 3 spheres and summation of 3 individual spheres.

The error graph shows that even though the individually evaluated models are very different, the summation of single sphere measurements is comparable to that of the original multi-sphere model. The relationship was tested for multiple sphere geometries and seemed to hold. The following hypothesis can thus be constructed: 'The unity-based normalization of the potential measured by a probe can be approximated as the unity-based normalization of the summation of potentials measured by the same probe due to individual spheres on the debris'. In a mathematical form this is described by Equation 3.2.

$$\Phi'_{\mathrm{p}} \approx \left(\sum_{i=1}^{n} \Phi_{\mathrm{p_{s,}}i} \right)' + \zeta_{\mathrm{c}} \tag{3.2}$$

In this equation, the number of spheres on the debris is given by n, while the definitions of the measured potentials Φ'_{p} and $\Phi_{\mathrm{p_{s,}}i}$ are as described above. Furthermore, the parameter ζ_{c} describes the mismatch in potential due to the coupling between spheres. In a more graphical way, this hypothesis is displayed in Figure 3.9.

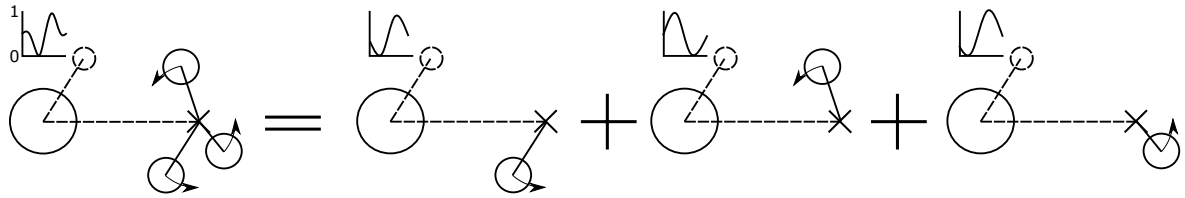

Figure 3.9: Graphical representation showing that the normalized measured potential can be decoupled in the summation of single spheres. On the left a single sphere representing the tug with a small probe attached indicating its (normalized) output. On the right three spheres representing the tumbling debris.

Even though this figure is a two-dimensional one, the content can be extended to three dimensions, as described by the model in Figure 3.7. Moreover, this relationship is tested for both tug and debris potentials of unity, indicating that on top of decoupling the spheres from each other, also the potential can be decoupled.

By analyzing the signals, it was found that Equation 3.2 can be adapted to obtain even less error between the coupled and decoupled model. The modified versions are given in Equations 3.3, where 3.3a seems to be performing better than 3.3b.

$$\Phi'_{\mathrm{p}} \approx \left(\sum_{i=1}^{n} \alpha_i \Phi_{\mathrm{p_{s,}}i} \right)' \tag{3.3a}$$

$$\Phi'_{\mathrm{p}} \approx \sum_{i=1}^{n} \beta_i \Phi'_{\mathrm{p_{s,}}i} \tag{3.3b}$$

By scaling each of the single sphere signals with α_i, or the normalized single sphere signals with β_i, the error can be decreased even further, as is displayed in Figure 3.10 for the same input as before.

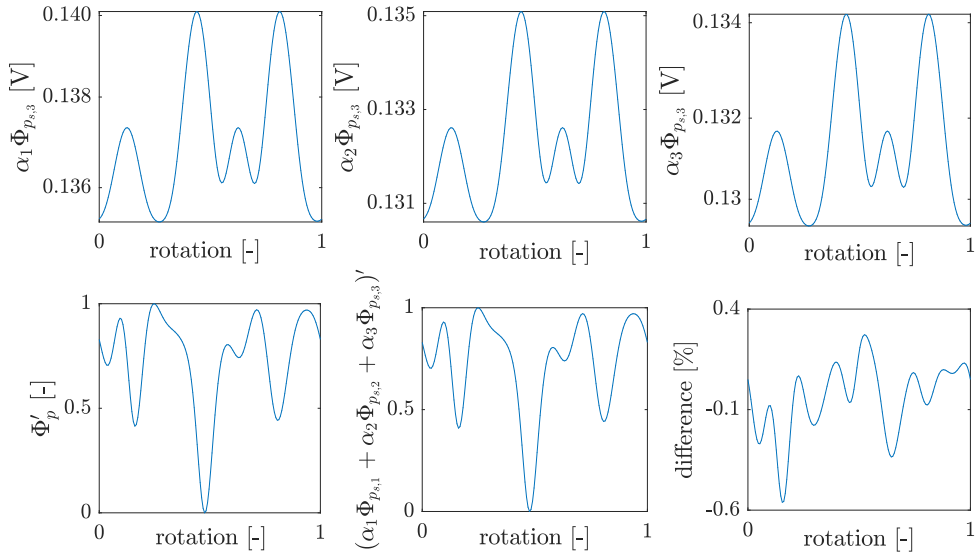

Figure 3.10: Summation of scaled potential curves as well as normalized potential of the three spheres together and the difference between the two.

The scaling factors applied in this figure have been found by numerically minimizing the norm of the error function. An explicit relation for these scaling factors has not been found however, as they are dependent on all other variables. Therefore it can be assumed that the effect of the capacitive coupling is mainly described by these scaling factors (which translates back to the parameter ζ_c).

As it is shown that the spheres on the debris can be decoupled, the question rises whether the same can be done for the spheres on the tug. If the full set of spheres can be reduced to a summation of single-tug-single-debris spheres, analytical equations can be used, speeding up the calculation of the model tremendously. Therefore, the following equation is analyzed:

$$\Phi'_p \approx \left(\sum_{j=1}^{m} \sum_{i=1}^{n} \Phi_{p_{s,ij}} \right)' \tag{3.4}$$

where $\Phi_{p_{s,ij}}$ is the measured potential due to sphere i on the debris and j on the tug. If the potential of tug and debris are again set to 1 and -1 V respectively, while assuming sphere radii of 1 m, the potential curves displayed in Figure 3.12 are obtained for the model represented in Figure 3.11.

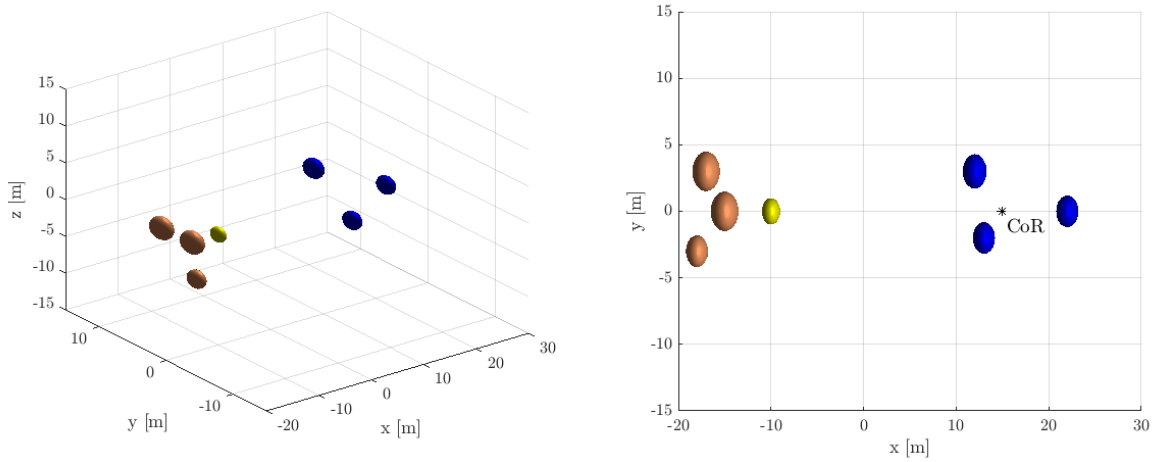

Figure 3.11: Graphical representation of the multi-sphere model given as input for decoupling of both tug and debris spheres. Tug is given in brown, probe in yellow and debris in blue.

In this model, an arbitrary rotation about the CoR has been chosen, completing a full revolution in time. The normalized probe potential due to the collection of spheres can be found in the left-hand side of Figure 3.12, while the normalized summation of all possible single-tug-single-debris potentials can be found in the middle of the figure.

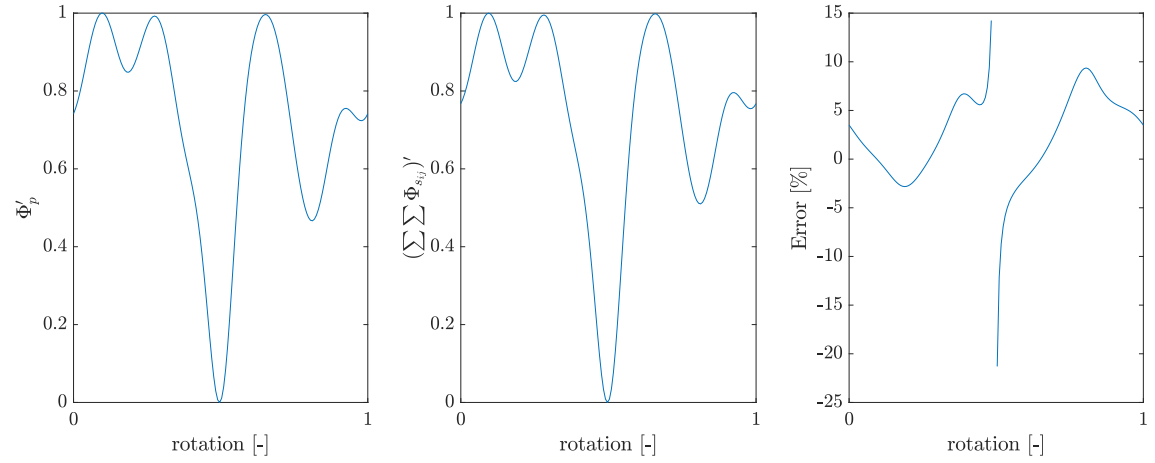

Figure 3.12: Normalized potential, normalized summation of 2-sphere signals and error between the two over a full rotation of the debris.

Evaluating the error between the two curves, as indicated in the right-hand side figure, it can be concluded that even for a few spheres, the error is significant. Therefore this approximation should not be performed when optimizing for sphere locations as the expected sphere locations will be off significantly as well.

3.4. Single Tug Approximation

The previous section described the decoupling of a generic multi-sphere problem. A special case of this problem is where the tug can be represented by a single sphere. For this case, the full set of equations described in Chapter 2 can be reduced to a more elegant form.

As described in the previous section, the model consisting of multiple spheres on the debris can be decoupled into a set of 'single spheres'. For the following discussion, one of such models is assumed

consisting of a single sphere on the tug and a single sphere on the debris. Rewriting Equations 2.5 and 2.8 for this simple system, yields the potential measured by a probe. In short form, this equation is written as:

$$\Phi_{p_{s,i}} = \frac{r_{t,s_i} r_{p,t} - r_{t,s_i} r_{p,s_i}}{r_{p,t} r_{p,s_i} - r_{t,s_i} r_{p,t} r_{p,s_i}} \tag{3.5}$$

where the potential of the tug and debris are taken as 1 and -1 Volt respectively. The distance between sphere *i* and the tug, from probe to tug $r_{p,t}$ and from sphere *i* to probe r_{p,s_i} are given by Equations 3.6 through 3.8 respectively.

$$\begin{aligned} r_{t,s_i} = \Big\{ & r_{sep}^2 + x_{s,i}^2 + y_{s,i}^2 + z_{s,i}^2 + \\ & 2r_{sep}\Big[\cos(\dot{\phi}t)\left(x_{s,i}\cos(\dot{\psi}t) + -y_{s,i}\sin(\dot{\psi}t)\right) + \\ & \sin(\dot{\phi}t)\Big(-\cos(\dot{\theta}t)\left(y_{s,i}\cos(\dot{\psi}t) + x_{s,i}\sin(\dot{\psi}t)\right) + z_{s,i}\sin(\dot{\theta}t)\Big)\Big]\Big\}^{1/2} \end{aligned} \tag{3.6}$$

$$r_{p,t} = \sqrt{x_p^2 + y_p^2 + z_p^2} \tag{3.7}$$

$$\begin{aligned} r_{p,s_i} = \Big\{ & \Big[-z_p + z_{s,i}\cos(\dot{\theta}t) + \left(y_{s,i}\cos(\dot{\psi}t) + x_{s,i}\sin(\dot{\psi}t)\right)\sin(\dot{\theta}t)\Big]^2 + \\ & \Big[x_p + -r_{sep} + \cos(\dot{\phi}t)\left(-x_{s,i}\cos(\dot{\psi}t) + y_{s,i}\sin(\dot{\psi}t)\right) + \\ & \sin(\dot{\phi}t)\Big(\cos(\dot{\theta}t)\left(y_{s,i}\cos(\dot{\psi}t) + x_{s,i}\sin(\dot{\psi}t)\right) + -z_{s,i}\sin(\dot{\theta}t)\Big)\Big]^2 + \\ & \Big[y_p + \sin(\dot{\phi}t)\left(-x_{s,i}\cos(\dot{\psi}t) + y_{s,i}\sin(\dot{\psi}t)\right) + \\ & \cos(\dot{\phi}t)\Big(-\cos(\dot{\theta}t)\left(y_{s,i}\cos(\dot{\psi}t) + x_{s,i}\sin(\dot{\psi}t)\right) + z_{s,i}\sin(\dot{\theta}t)\Big)\Big]^2\Big\}^{1/2} \end{aligned} \tag{3.8}$$

In these equation, the location of sphere i with respect to the CoR is given by $(x_{s,i}, y_{s,i}, z_{s,i})$ and the location of the probe with respect to the (center of the) tug is given by (x_p, y_p, z_p). The distance from the tug to the CoR along the x-axis is given by r_{sep} and the rotations are given by the proper Euler anglesϕ, θ and ψ (z-x'-z'). These angles are obtained for every time step from the respective Euler angle rates $\dot{\phi}$, $\dot{\theta}$ and $\dot{\psi}$. An overview of these angles can be found in Figure 3.13[4].

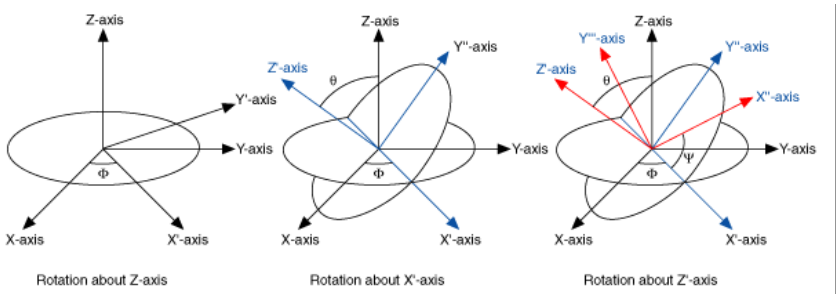

Figure 3.13: Rotation of a Cartesian coordinate frame with the Euler angles Φ, Θ and Ψ (z-x'-z'), as obtained from National Instruments [4].

In this figure, the rotation of a Cartesian axis system is performed about the z-x'-z' axis. The first revolution about the first axis is shown in the left-hand side of the figure, while the final orientation of the axis system can be found in the right-hand side.

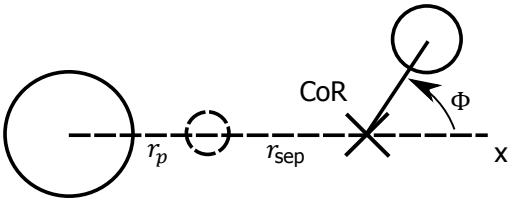

Figure 3.14: Planar 'single sphere' geometry with the tug on the left, the probe in the middle and the debris on the right.

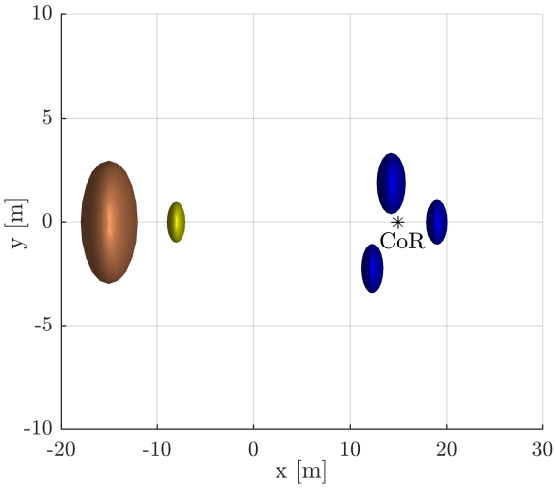

Figure 3.15: Planar problem geometry with the debris spheres in blue, the tug in brown and the probe in yellow.

3.5. Planar Semi-Analytical Single Sphere Model

There exists a special case for which the sphere locations can be found very accurately. When the debris is very flat, i.e. it extends only marginally in the direction of a certain axis, and rotates exclusively around this axis as well, the spheres only have to be distributed in two-dimensional space. This problem is already dealt with in[23], but now the single sphere model is introduced.

The following model is constructed. A single sphere representing the tug with Radius R is placed at the origin. The CoR is located along the x-axis at a distance r_{sep}. Along the same axis, the probe is located at a distance $r_{\text{p,t}}$ from the tug and the debris at a distance r from the CoR, all in positive direction. Now the debris is given an initial phase offset Φ around an axis perpendicular to the x-axis. This geometry is sketched in Figure 3.14.

The normalized potential $\Phi'_{\text{p}_{\text{s},i}}$ measured by the probe at any time t:$[0, 2\pi]$s, is given by Equation 3.9.

$$\begin{aligned}\Phi'_{\text{p}_{\text{s},i}} = 1 - \Bigg\{\Bigg[&\frac{1}{\sqrt{r_{\text{sep}}^2 + 2r_{\text{sep}} r\cos(t+\phi)}}\left(\frac{1}{r_p} + \frac{1}{r_{\text{sep}} - r_p + r\cos(t+\phi)}\right) - \\ &\frac{1}{\sqrt{r_{\text{sep}}^2 + 2r_{\text{sep}} r}}\left(\frac{1}{r_p} + \frac{1}{r_{\text{sep}} - r_p + r}\right)\Bigg] \Big/ \Bigg[\frac{1}{\sqrt{r_{\text{sep}}^2 - 2r_{\text{sep}} r}}\left(\frac{1}{r_p} + \frac{1}{r_{\text{sep}} - r_p - r}\right) - \\ &\frac{1}{\sqrt{r_{\text{sep}}^2 + 2r_{\text{sep}} r}}\left(\frac{1}{r_p} + \frac{1}{r_{\text{sep}} - r_p + r}\right)\Bigg]\Bigg\}\end{aligned} \tag{3.9}$$

To derive this equation, the normalization Equation 3.1 is applied on the equations for probe potential 2.5 and 2.8. Furthermore, the quantity $\frac{V}{R}$ for both tug and debris is set to zero as this is just a scaling factor and the potential of both spheres is again set to unity.

In order to apply the given equation, first a model must be constructed consisting of multiple spheres. Consider the geometry displayed in Figure 3.15, where three spheres have been placed on the debris. For this geometry, the normalized potential measured by the probe Φ'_{p} is displayed in the left-hand side of Figure 3.16. As it is known from the previous sections that this signal is the summation of a set of single sphere signals, the phase of the signals can be decoupled. For a single sphere undergoing a full

rotation, the valley of the signal, i.e. where the distance between the two spheres is smallest, occurs once. The problem of a multi-sphere problem is however, that not all peaks can be distinguished, as some spheres 'cast a shadow' on the signal of others. An often more fruitful approach is to look at the second derivative of the signal, as can be seen in the right-hand side Figure 3.16. Whereof in the Φ'_p signal, only two valleys and valleys can be distinguished, the second derivative shows all three of them.

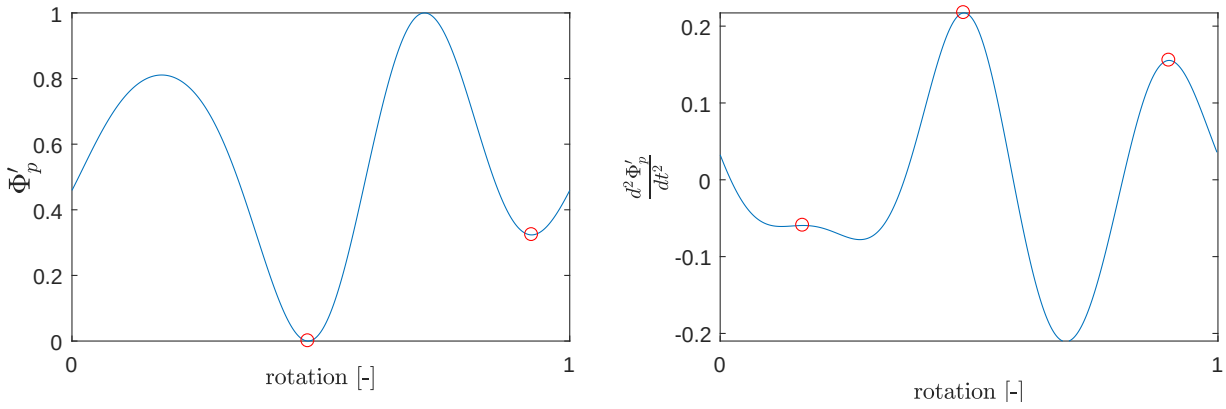

Figure 3.16: Normalized probe potential and its second derivative versus a full rotation of the debris.

As the initial phase offset of each sphere is directly related to the position of the peaks in the second derivative, it is of essence that these peaks are clearly observable. In order to see how well they can be found over a range of sphere radii R and rotation distances r, a Monte Carlo simulation is performed. For a random distribution of 1000 sets of R and r, as well as for 4 distinct sphere geometries indicated by Φ, the probability of finding a peak at a certain location is given. In other words, for three given sphere phases, the parameters R and r are varied and the peak locations in the respective signal are counted. By performing this simulation, a metric of robustness can be specified as to whether for a random signal, the sphere locations can be filtered out. If the peak locations are found with a high probability and at the right locations, this method of deducing sphere locations directly from the observed potential signal can prove to be promising, while vice versa the method is not found suitable for future development. The results of the simulation can be found in Figure 3.17.

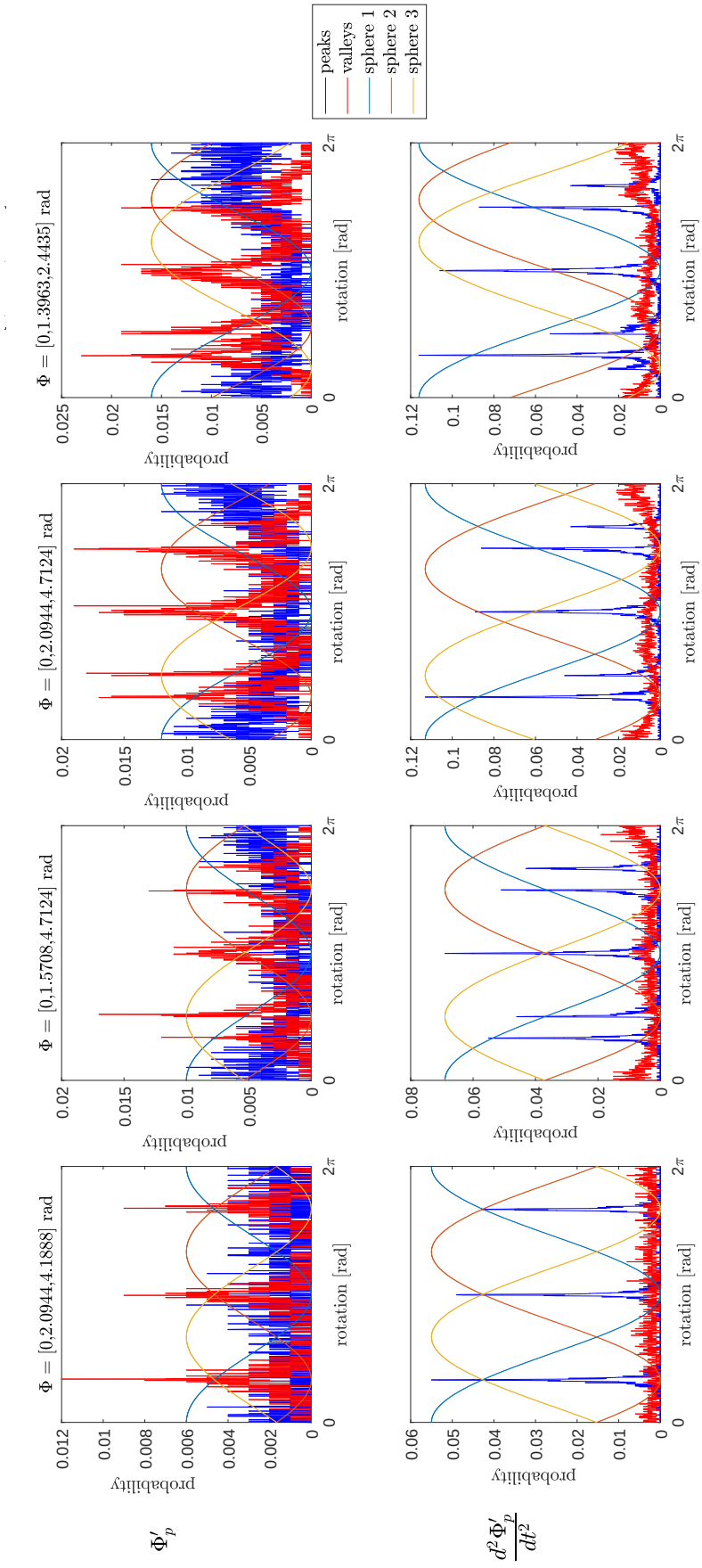

Figure 3.17: Monte Carlo simulation showing the probability of finding a peak in the normalized probe potential and its second derivative, for a random distribution of r and R, for 4 sets of sphere locations.

In the top row of this figure, the probability of finding the peaks and valleys in the normalized probe potential signal is given versus a full rotation. The second row represents this data for the second derivative of the signal, where every column corresponds to a specific sphere geometry indicated above the graphs. The angles specified are the phase offset of the three debris spheres. Furthermore, the normalized probe potentials due to each single sphere $\Phi'_{p_{s,i}}$ are scaled to the maximum value of the peaks and plotted in every graph as well. The peaks and valleys should therefore be matched with the respective peaks and valleys of these curves, as they represent the truth model.
From the figure, a few observations can be made. First of all, the peaks are indeed more clearly resolvable for the second derivative than for the normalized probe potential $\Phi'_{p_{s,i}}$. Where in the latter the distribution of the peaks is more spread out and therefore often found at the wrong locations, the second derivative shows almost a perfect distribution. Furthermore, due to the coupled nature of the problem, peaks are forming close to the location where the peak is expected without the influence of other spheres. Especially for phase angles close to each other, the resolvability of individual peaks and valleys becomes more cumbersome. Lastly, and most important, the probability is at most marginal, indicating that for most models, it is very difficult to resolve each sphere individually. By increasing the amount of spheres, the resolvability becomes even worse.

Assuming a model is chosen where the peaks can be resolved and therefore the phase offset of each sphere be found, the next step is to obtain the scaling factor and sphere distance r. Since the analytical equation for $\Phi'_{p_{s,i}}$ is known, Equation 3.3b can be used to find β_i, rather than using Equation 3.3a. As a solving method, the Matlab built-in function *fsolve* is used, which requires input of the same amount of equations as there are unknowns[36]. Since the debris sphere populations is 3, and the parameters that have to be solved for are r and β_i, the amount of unknowns is 6. In order to obtain the same amount of equations, 6 sample points are taken from the normalized probe potential signal Φ'_p. As the influence of the individual sphere signals is most prominent around the peaks, the samples are taken at $0.1/\pi\%$ to the left of each peak and valley. Additionally two samples are taken at the same distance to the right of the valleys. An overview of these sample points can be found in the left-hand side of Figure 3.18. In order to obtain the 6 equations, Equation 3.9 is substituted in 3.3b and evaluated at the sample points. The resulting approximation of Φ'_p can be found in the left-hand side of Figure 3.18.

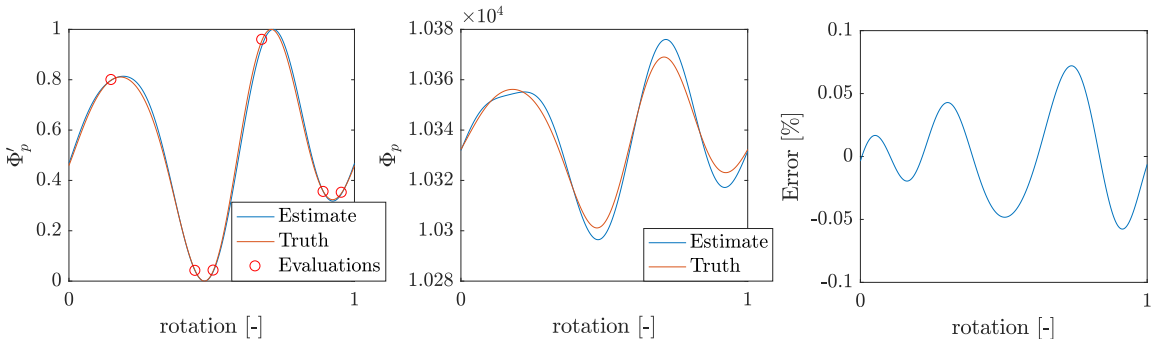

Figure 3.18: Truth and estimate (normalized) potential curves, also showing the sample locations and error of the approximation.

The last step in finding the best representative sphere model, is to obtain the original sphere radii R and debris potential Φ_D. In order to find these parameters, a model is constructed with the obtained sphere distances r and phase offsets Φ, but now with an arbitrary set of sphere radii and debris potential V_d. By minimizing the difference between the measured probe potential of this approximated model and the 'truth' model, the best fitting radii and potential can be obtained. A more in-depth analysis of such an optimization process can be found in the next chapter. The resulting best fitting Φ'_p can be found in the middle of Figure 3.18, while the error between 'truth' and approximate Φ'_p are displayed in the right-hand side of the figure. Even though the error is small, it should be noted that this does not account for the scale of the signal. As the potential is in the kilovolt range, the absolute error can result in significant errors in electrostatic force approximation.

From the analysis and methodology described in this section, it becomes clear that for the special case

of a planar piece of debris with distinguishable peaks, the potential can be found very accurately and without large computational costs by performing some simple manipulations. For three dimensional problems however, the analytical solution is hard to obtain. A reason for this is that locations out of the plane of rotation are only marginally separable, as can be observed in figure 3.19.

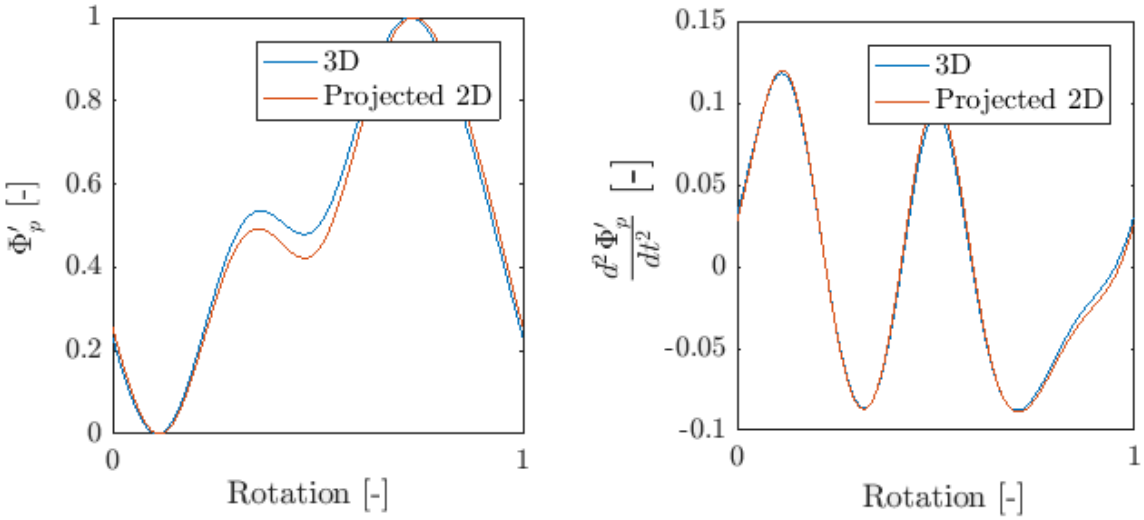

Figure 3.19: Normalized potential and its second derivative of a three-dimensional multi-sphere problem and the projected two-dimensional version.

This figure is created with a 3-sphere (on debris) model where two of the spheres are placed out of plane. A projected version of this model consists of the same spheres but without the out of plane component (so the z-component is set to zero). As the out of plane distance only marginally increases the total distance to the probe, the effects on the probe potential are almost impossible to discern.

3.6. Spatial Numerical Single Sphere Model

In case the tug cannot be accurately represented as a single sphere, the equations in Section 3.4 no longer hold. In order to decouple the equations and simplify them, the following model is considered. The tug is represented by m spheres with radii R and uniform potential Φ_T. The debris consists of n spheres with radii R and uniform potential Φ_D. The 'single sphere' probe potential $\Phi_{p_{s,i}}$ can then be calculated with Equation 3.10.

$$\Phi_{p_{s,i}} = k_c\left(\sum_{j=1}^{m}\frac{q_j}{r_{p,j}} + \frac{q_i}{r_{p,i}}\right) \qquad i \in n \tag{3.10}$$

The charge a can be found from the capacitance Equation 2.5, but with the potentials adapted to Φ_T and Φ_D, as is done in Equation 3.11.

$$\begin{bmatrix} q_1 \\ q_2 \\ \vdots \\ q_m \\ q_i \end{bmatrix} = \frac{1}{k_c}\begin{bmatrix} 1/R_1 & 1/r_{2,1} & \dots & 1/r_{m,1} & 1/r_{i,1} \\ 1/r_{1,2} & 1/R_2 & \dots & 1/r_{m,2} & 1/r_{i,2} \\ \vdots & \vdots & \ddots & \vdots & \vdots \\ 1/r_{1,m} & 1/r_{2,m} & \dots & 1/R_m & 1/r_{i,m} \\ 1/r_{1,i} & 1/r_{2,i} & \dots & 1/r_{m,i} & 1/R_i \end{bmatrix}^{-1}\begin{bmatrix} \phi_T \\ \phi_T \\ \vdots \\ \phi_T \\ \phi_D \end{bmatrix} \qquad i \in n \tag{3.11}$$

As described in Section 2.3 by Equation 2.7, the inverse capacitance matrix can quickly be evaluated using a block matrix inversion.

3.7. Summary and Conclusions

In this chapter, the influence of the parameter R, V_d and sphere locations are described. It is shown that the potential of debris and tug has little influence on the optimal location of debris spheres. For this reason, it is beneficial to perform an optimization based on the normalized potential signal. This reduces the set of parameters that have to be optimized for and decouples the potential from the sphere locations. Furthermore, it is found that also the radius of the debris spheres can be decoupled for some distinct cases. The biggest influence on the constructed potential curve, is the distance of which spheres are revolving around the CoR. For a debris geometry that is very planar, this means that the set of parameters that describe most of the normalized potential curve, are the orbital radius r and initial angle (phase) Φ. Furthermore, it is shown that the normalized potential signal due to a set of debris spheres is almost equal to the normalized summation of single debris sphere signals. Effectively, this means that instead of computing the inverse capacitance matrix of a square $m+n$ sized matrix, n computations of a square $m+1$ size matrix have to be computed. The effect of decoupling the spheres from each other on computational cost can be found in Figure 3.20.

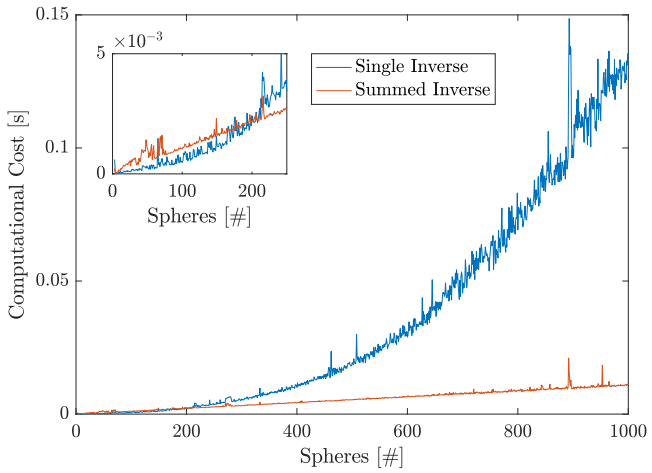

Figure 3.20: Overview of computational cost of inverting a single square matrix of varying size or multiple times (size-2) a matrix of size 3.

In this figure, the computational cost of inverting a square matrix of varying size (3 through 1000) is compared with inverting a $3x3$ matrix a varying amount of times (1 through 998). This corresponds with a inverting the inverse capacitance matrix of a 2-sphere tug and single sphere debris. As can be seen in this figure, computing multiple times a smaller matrix is only beneficial in terms of computational cost when more than a couple of hundred spheres have to be evaluated. In terms of absolute computational cost of inverting the inverse capacitance matrix in the RSEC method, a significant variation between the two models can be found. As every iteration within the optimizer requires computation of the potential curve, the amount of inversions performed during a full RSEC application is considerable. The biggest advantage of decoupling the spheres however, is the insight that can be gained from analyzing the influence of every sphere separately. The RSEC method can be therefore possibly be improved to find the individual sphere locations based on peaks and valleys in the potential signal, as described in Section 3.5. Furthermore, for models where the tug can be approximated by a single sphere, the analytical equations for the normalized potential can be constructed for this simple two-sphere model, which can be added together to create the decoupled MSM model.

Concluding from these observations, it can be stated that simplifications to the MSM model can be used to decrease the amount of parameters that have to be optimized for such that the coupling effect between sphere location, radius and potential can be decreased. This means that for many spheres, the computational cost can be decreased, while for only a few spheres, these spheres can be placed based on observation of peaks and valleys in the signal, although this is currently only evaluated for planar geometries and rotations.

4

Optimizing Strategies

In the previous sections, the physics and geometry of the Multi-Sphere Method (MSM) model have been described. In order to find the best sphere locations, as well as potential and radii, optimization algorithms are applied. Depending on the application, information about the debris and/or tug can be available. Visual inspection of the target body during a formation flying maneuver can indicate whether the tumbling motion is dictated by a single axis, or whether the body can be approximated by a near-planar shape. Furthermore, calibration data of the tug can indicate whether a single tug sphere model is justified. Depending on the availability of this information, the scheme drawn in Figure 4.1 indicates which model simplification can be used. The relevant section in which these simplifications are described are also given.

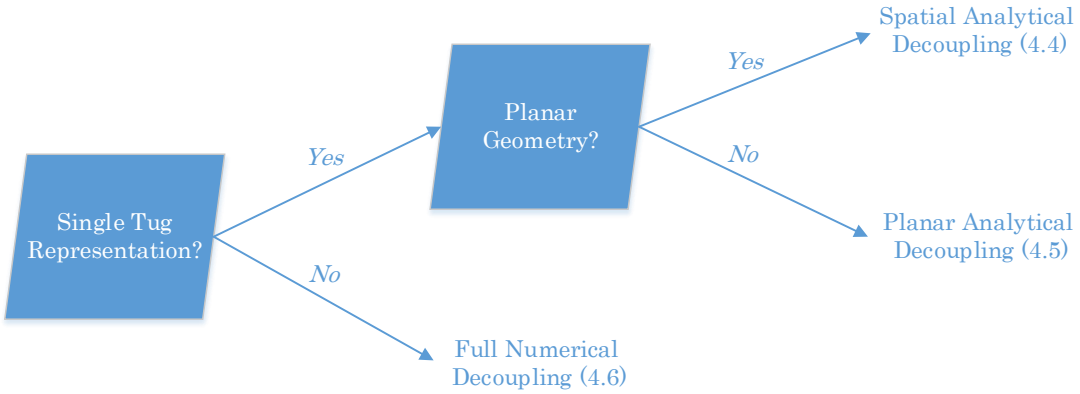

Figure 4.1: Logic tree describing which simplifications of the model can be used and where to find them in this report.

Based on the appropriate simplification of the model, a optimizing strategy can be chosen. Three distinct optimization methods are developed and will be evaluated. An overview of these methods can be found in Table 4.1.

Table 4.1: Overview of three distinct solving methods and a description of which state variables they solve for.

Name	Algorithm	State Variables
Method 1	1. Optimize using radii and potential of unity and random sphere locations	x,y,z
	2. Optimize using resulting state variables from step 1	x,y,z,R,V
Method 2	1. Optimize using random radii, potential and sphere locations	x,y,z,R,V
Method 3	1. Optimize using radii and potential of unity and random sphere locations	x,y,z
	2. Optimize only sphere radii and potential	R,V

In this table, for each of the methods, the steps (algorithm) are displayed and in the right-most column, the parameters solved for are displayed. A more elaborate description of the methods is given hereafter.

The first method applies the sphere decoupling equations found in Chapter 3. The debris and tug potential are set to unity, as are all sphere radii R. After optimizing the sphere locations using the reduced system, a second optimization is performed, where the sphere locations are given as input, while the output contains sphere locations as well as radii and potentials. This method can be applied to show that the decoupled system can be used to find a first approximation. Especially for simple debris geometries, the computational time can be significantly reduced as (semi)-analytical equations can be used to find the potential over time. The second method is to perform a single optimization, starting from a random generated initial state vector. No decoupling of parameters is performed and the optimizer tries to find all sphere locations, radii and potential of the debris in the same time. This method is most robust and requires the least amount of assumptions. The third method takes roughly the same approach as the first. By decoupling the model, a first rough solution set of sphere locations is found. The second optimization then uses these sphere locations, but only solves for the radii and potential. Due to the coupling of sphere radii and their location, this method is the least accurate of the three and not evaluated in most of the simulations following.

An overview of the functional flow of the first two methods can be found in Figure 4.2.

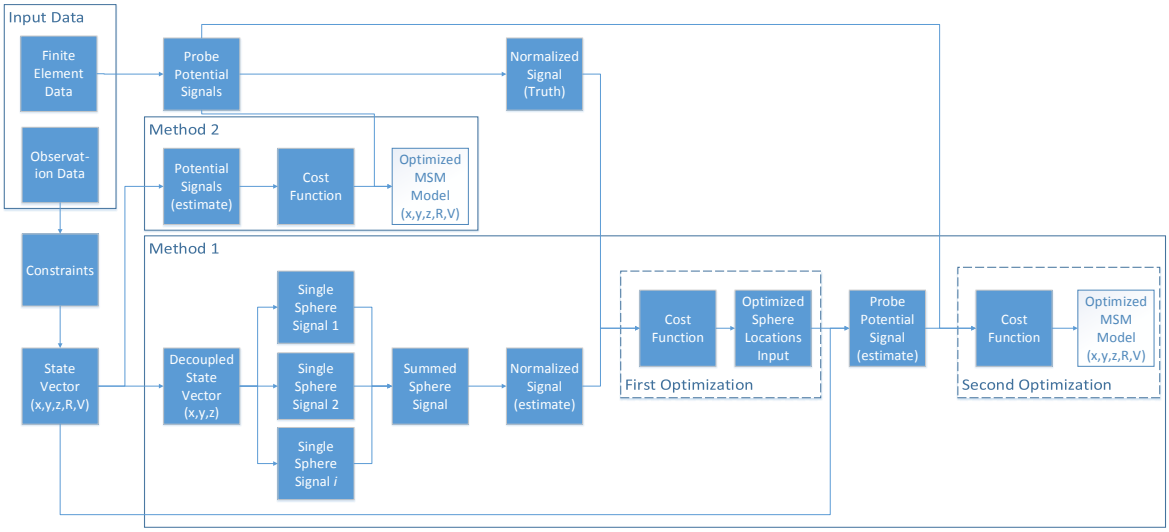

Figure 4.2: Model flow diagram indicating the operations performed in the two distinct optimization methods.

Depending on the method chosen, a state vector is created. This vector contains the parameters that will be optimized for. Based on an initial state vector, a MSM is set-up, taking into account constraints and limitations of the parameter values. Depending on the method, the resulting potential curve is obtained as a summation of single sphere potentials, or directly from the MSM model. In order to compare this curve with the potential measurements, a cost function is created. By varying the state vector, the cost function can be minimized, such that the potential curves match to a specified tolerance. In order to constrain the range of values the state vector can assume, boundary conditions are supplied. The sections following in this chapter describe the building blocks of the flow in more detail.

4.1. State Vector and Initialization

Referring back to Figure 2.2, each sphere is represented by its coordinates (x, y, z) in the Local Vertical Local Horizontal (LVLH) reference frame, and radius R. Furthermore, the set of spheres on the tug has a uniform potential of V_t and the set of spheres on the debris a uniform potential of V_d. Assuming the set of parameters of the tug is known from calibration, the state vector containing all parameters of interest can be constructed as:

$$\mathrm{x} = [x_1, y_1, z_1, R_1, \ldots, x_n, y_n, z_n, R_n, V_{\mathrm{deb}}] \tag{4.1}$$

where n is the total number of spheres on the debris. In order to find the best-fit MSM model, these parameters are varied until a satisfying combination is found. Due to the large size of parameters optimized for and coupled nature of the MSM model, multiple solutions exist that satisfy the optimizing tolerance. Furthermore, for specific combinations of the parameters, local minima are attained in the cost function. For this reason, evaluating the initial state vector is of importance. By forcing a specific distribution on the spheres, these minima can be evaded.

The most robust population of the initial state vector is with a random distribution. When the optimizer is able to find an accurate representation of the debris starting from a state constructed with minimal knowledge of this body, i.e. a random input, the Remote Sensing for Electrostatic Characterization (RSEC) method can be expected to work for the widest range of applications. Assuming some knowledge of the shape of the debris is available, the initial state vector can be constructed more efficiently. By evaluating the geometrical bounds of the body, a sphere distribution can be applied to this region. This can be done either with a volume population method, or a surface population method[37]. Furthermore, a either a homogeneous distribution of spheres can be chosen, or one that mimics more of the local behavior of the body. As the random state vector initialization gives most credit to the applicability of the RSEC method, this initial state vector representation is chosen for the simulations described in this report.

4.2. Cost Functions

Optimization is performed by varying the parameters in the state vector, such that a cost function is minimized. The cost function therefore has a big impact on the ability of the solver to find the best fitting sphere distribution. In general, the parameters are varied until the cost function attains a specified tolerance. This tolerance is often specified as a minimum step-size, or a minimum function value. In order for the optimizer to take smooth steps along a clear gradient, the cost function should be clearly defined.

For the RSEC method, the data that is obtained as input and reference, is the potential measured by probes. Typically, cost functions take values in the $0 - 1$ range. A typical and simple cost function J which is clearly defined and positive-definite, such that a smooth behavior can be expected, is given in Equation 4.2[38].

$$J = \left\| \phi_{\mathrm{P}}(\mathrm{x}, \mathrm{t}) - \phi_{\mathrm{M}}(\mathrm{t}) \right\| \tag{4.2}$$

In this equation, the norm is taken between a measured ($\Phi_{\mathbf{M}}$) and predicted potential signal $\Phi_{\mathbf{P}}$. Another option is to first normalize the individual signals, before taking the norm, as is displayed in Equations 4.3.

$$J = \left\| \frac{\phi_P(x,t) - \min(\phi_P(x,t))}{\max(\phi_P(x,t)) - \min(\phi_P(x,t))} - \frac{\phi_M(x,t) - \min(\phi_M(x,t))}{\max(\phi_M(x,t)) - \min(\phi_M(x,t))} \right\| \tag{4.3a}$$

$$J = \left\| \phi'_P(x,t) - \phi'_M(t) \right\| \tag{4.3b}$$

Applying normalization to the signals offers some advantages and some drawbacks. In the previous chapter, it has been shown that normalizing the data reduces the influence of sphere radii and potential. When optimizing for these two parameters, it is therefore wise to choose a cost function which is not dependent on normalization. The advantage of normalizing data however, is that for some debris rotations and probe locations, the influence of spheres located far from the Center of Rotation (CoR) is minimal on the cost function, while they do have a large influence on the torque in the system. By placing probes more outwards, the effect of these spheres becomes more prominent, but as the potential data itself decreases in magnitude, this effect gets reduced. By normalizing the potential data for such a case, better fitting sphere models can be found.

In order to analyze how the cost function behaves, the following 'cube-plate' model is constructed. Given the MSM model as displayed in the right-hand side of Figure 4.3, one additional sphere is added to the system. The z-location of the additional sphere is 0, while the x and y-direction are varied. For every location, the cost function is evaluated. In the left-hand side of Figure 4.3, the cost function values are displayed, where the scale is arbitrary, but should be minimized.

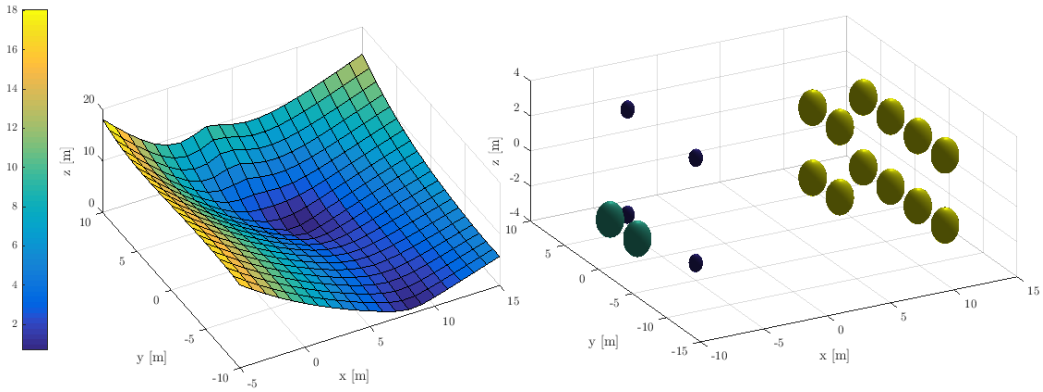

Figure 4.3: Cost function evaluation for placement of a single sphere, with on the right-hand side the MSM model to which the sphere is added.

From the figure, it can be concluded that the cost function is minimal near the regions where most charge resides. Especially the far end of plate, i.e. the location that comes closest to the tug over during the tumbling motion, the cost function value attains a low value. The result of this behavior is, that spheres tend to move towards the most outwards position on a geometry.

4.3. Boundary Conditions and Constraints

In order to obtain better optimization results, it can be helpful to implement boundary conditions. This sections gives a brief overview of these conditions and the motivation for their application.

There are two boundary conditions that are always applied, as they are found to contribute significantly to the performance of the RSEC method. First of all there is a constraint which requires the spheres to have a certain minimal separation from each other. In order to enforce this constraint, the distance from each sphere to the others is determined, after which the minimal value is tested with a reference

distance. By enforcing a minimal sphere separation, it is made sure that spheres do not overlap, which creates singularities in the capacitance matrix. Furthermore, spheres that are overlapped do not contribute to the system of spheres and therefore these spheres should be forced to a different location.

Secondly, there are upper and lower bounds in the state vector. These can be seen as a bounding box around the debris, in which the spheres have to be located. The size of this box can found from visual inspection, or can be taken very large to ensure general applicability. Furthermore, the upper and lower bounds put a constraint on the sphere radii. Where spheres are enforced to maintain distance, a large sphere can still overlap another sphere. Therefore the size of spheres is generally restricted to values smaller than 3 meter. Lastly, the debris potential is allowed to vary between 0 and -50 kV. Due to the Electrostatic Tractor (ET), the magnitude of the debris potential will have a negative sign. Also, as the truth potential is 30 kV, potentials larger than -50 kV can be neglected.

If information about the debris geometry is present from observations, a 'bounding box' can be placed around the body. The debris spheres are not allowed to be placed out of this box. For the debris geometry applied in this report, a bounding box is chosen that has a length of 30, width of 10 and height of 10 meter, where the length is along the panels. As the debris geometry is a lot smaller, this bounding box is a soft constraint.

Another constraint that is often useful, is that of sectors. As is shown in the previous section, spheres tend to move to the edges of a geometry while optimizing. In order to ensure that not all spheres move to this edge, a restriction is applied where at least some spheres have to be located on the opposite side of the CoR. If a bounding box is present, this box can be divided in sectors. For the simulations described hereafter, four equal sized sectors are applied in the xy-plane, with the intersection at the CoR.

4.4. Choice of Optimizing Function

Depending on the geometry of the problem and the available sensor data, several different optimizing functions / algorithms can be chosen. The first optimizing function discussed is the *fsolve* function within Matlab[36].

Especially for planar decoupled models, the amount of parameters that have to be estimated can be limited. For such models, the *fsolve* function within Matlab can give accurate results[36]. The condition for which this function can be used, is that an equal amount of equations as there are parameters must be specified, as this function solves for a system of nonlinear equations. For a decoupled problem, so solving only for (x,y,z), where n=3 spheres have to be optimized, this means that either 9 probes are required, or that measurements are split, making the algorithm more complex. Furthermore, after this optimization, still the potential and radii of the spheres have to be found, requiring a second optimization step.

A second option is to use the *fmincon* function, which is a gradient based solver built-in to Matlab[39]. The solver evaluates the specified cost-function based on a state vector and constraints as specified in the previous sections. By determining the gradient of the function around the current evaluation point, the next state vector values can be determined. The function continues to evaluate the cost function until the next step size or the difference in cost function is smaller than a given tolerance. Especially for a large population of spheres, the objective function is not very smooth and the chance of ending up in a local minimum is large. As a solution, the function can be run multiple times with a random input, by using the *multistart* option[40].

The third option considered is to enforce multiple starts is by using a *genetic algorithm*. Such an algorithm evaluates many initial conditions and based on their outcome, a new pool of initial conditions around the best outcome is created. By doing so, the best options 'survive'. The downside of such an algorithm is the computational cost it introduces.

The method that is found to be working best under the widest range of debris geometries and rotations, while still introducing manageable computing cost, is the *fmincon* function. For the numerical simulation described in the next chapters, this function is therefore applied.

5

Finite Element Validation Setup

As all of the physics, equations and constraints concerning the Remote Sensing for Electrostatic Characterization (RSEC) method have been analyzed, the next step is to put the developed method to the test. As it is infeasible to obtain in-situ potential measurements of an actual piece of debris orbiting around Earth, an alternative source of data is required. This chapter elaborates on different options to obtain this data. An overview is given on how a representative Finite Element Analysis (FEA) is set-up and the validity of the resulting data. Furthermore, an intermediate step to obtain data in terms of the Surface Multi-Sphere Method (SMSM) is described, allowing for more extensive multi-axis simulations.

5.1. Validation Options

Although a flight experiment is beyond the scope of this research and no relevant data can be collected from past missions, there are some options to obtain a valuable set of data. To date, there have been a couple of experiments regarding the electrostatic interaction between bodies[41,42]. In these experiments, a sphere is constructed from foam, on top of which an aluminum conducting layer is wrapped. A high voltage source is attached to the sphere as to charge it to kilovolt potentials, mimicking the Multi-Sphere Method (MSM) behavior. If such an experiment is to be extended as to test the performance of the RSEC method, an important issues has to be resolved. In order to test the ability to measure the potential at a distance from these spheres and use the RSEC method to find the force, a probing technique has to be found capable of observing these potential levels in a contact-less manner. From a meeting with staff from the TU Delft High Voltage Lab (HVL) addressing this issue, the following results were found[43].
Measuring the potential at a distance is possible with a contact-less probe such as the Trek probe[44]. These kind of probes only work for small separations with the charged surface however, as to create a capacitance in the sensor that can be measured. For larger separations, a lot of noise is introduced in the measurements. As the spheres require a radius of tens of centimeters to store the charge and generate a uniform field, the separation distance between spheres, and therefore also between probe and sphere has to be a lot larger than the probe can provide accurate measurements for.
The second option is to use an electric field mill to retrieve potential data from the electric field between the spheres[45]. The electric field mill that is available however, has dimensions in the order of ($10x10x10$ cm), which severely restricts the accuracy of the measurements. Scaling the measurements to larger dimensions is neither an option as the test-setup will become cumbersome. A third option is to place a small conductor, such as a piece of metal, in the field. By measuring the deflection with a laser, the field properties can be obtained. As such a test-setup has to be created from scratch, this option is also ruled out. Creating and calibrating this set-up is beyond the scope of this research, while the outcome of the measurement has to be validated itself. Before such an experiment can be applied to validate the RSEC method, there most like is no space left in the alloted time for this thesis work.
It was decided to focus on computer models, as this was the most practical and feasible approach. The experience of the HVL has shown that a FEA using the Comsol software is a reliable source of data[46].

The set-up of the Comsol model, will be discussed in the following sections.

5.2. Geometrical Comsol Model

In order to construct a model which resembles a possible mission scenario while still keeping computational cost within bounds, the geometry displayed in Figure 5.1 is chosen.

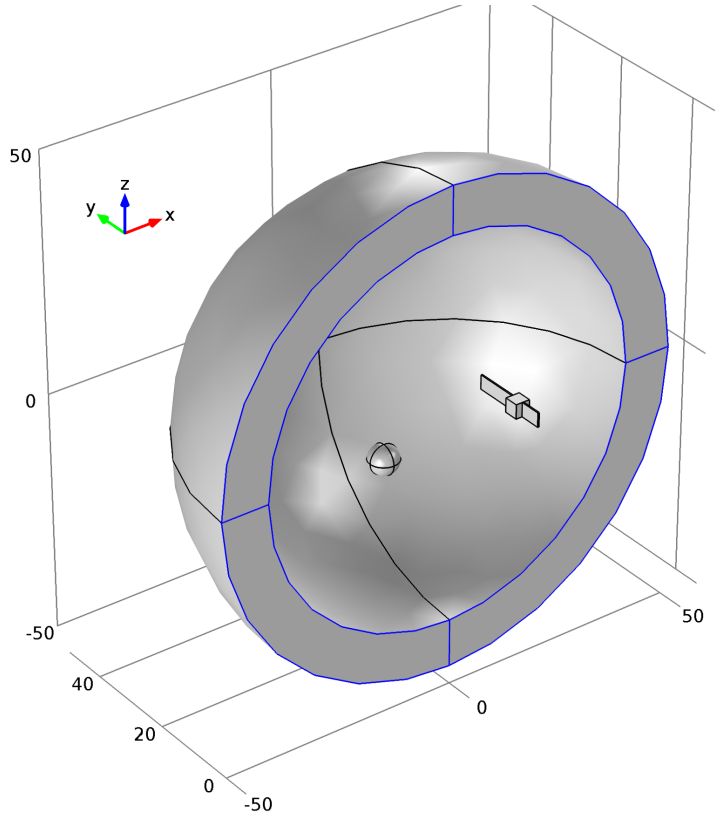

Figure 5.1: Graphical representation of the Comsol model used to create validation data for the RSEC method.

As it is assumed that the characteristics of the tug will be calibrated for, a single sphere of 3 meters radius is chosen. This allows for direct application of and comparison with the equations described in previous chapters, as well as simple meshing of the surface and reduction of computational cost with respect to a complex shape with more resemblance to a satellite. The drawback of using a simple sphere is that the model is simplified and resembling less of an actual mission scenario. The 3 meters is chosen as an effective satellite radius based on data obtained from Jasper and Schaub[47]. The debris is modeled as a box with two plates adhered, as to represent a defunct satellite with two solar panels. One of the panels is shorter than the other in order to introduce asymmetry to the model. This allows conclusions to be extended to a wider range of application as well as to obtain more clearly distinguishable potential measurement data. The separation distance r_{sep} is chosen to be 30 meters, such that the panels of the debris tumbling around the middle of the box will never hit the tug or probes. The location of the probes, debris and tug are indicated in Table 5.1

Table 5.1: Locations of probes, debris and tug describing the Comsol model geometry.

	x [m]	y [m]	z [m]
Probe 1	-10	-10	10
Probe 2	-10	-10	-10
Probe 3	-10	10	10
Probe 4	-10	10	-10
Tug (c)	-15	0	0
Debris (c)	15	0	0

Table 5.2: Dimension of debris and tug describing the Comsol model geometry.

	Width [m]	Height [m]	Length [m]
Panel 1	0.3	3	9
Panel 2	0.3	3	4.5
Box	3	3	3
Sphere	3	3	3

Furthermore, a large sphere with radius of 50 meter and a layer thickness of 10 meter is added around the bodies. On this sphere, the infinite element boundary constraints are applied, as to represent the potential field at infinity, which is set to zero.

Note that the probes are not included in the geometrical model displayed in Figure 5.1, as the registered potentials are taken at points in space. By doing so, the probes will not change the field around them, which is also assumed for the RSEC method discussed in this report. This reduces the need for simulating probe behavior, which is a study on its own. Other boundary conditions that are applied to the model are the potentials on the debris and tug, as well as charge conservation in the whole system. The debris is given a potential of -30 kV, where the tug assumes an electric potential of 30 kV.

5.3. Meshing of the Model

Selecting and creating an appropriate mesh has a tremendous influence on the outcome of the FEA study. A very coarse mesh will result in fast computation but poor results, while a fine mesh yields high accuracy results at the cost of computation time. In order to find the right balance, some observations are made. First of all, the infinite element domain allows for a coarse, swept mesh, as the geometry is very symmetric and results in this domain are not as critical as on the surface of the bodies. A view of this mesh can be found in Figure 5.2. Secondly, the domains inside of the debris and tug are of least importance as well, as all charge will reside on the surface of the bodies. Therefore these domains can be applied with a coarse mesh as well. The size of the mesh is still significantly lower than that of the infinite element domain, as the size of the bodies surrounding the mesh are smaller. Thirdly, the points on the bodies closest to each other will accumulate most charge, therefore requiring the finest mesh. In order to account for this, the point on the tug closest to the debris is chosen to have a maximum mesh size of only 1 cm. A larger mesh-size is found (in test-runs) to introduce a lot of noise in the force-curves. An even smaller mesh size introduced memory issues and drives the computational time to levels that are not manageable within the given time. Lastly, computing the surface charge for straight edges requires a very fine mesh. Therefore the edges of the debris are all given a maximum mesh size of 1 cm as well. As giving a good view of such a fine mesh is difficult, a mesh with a larger size was constructed and illustrated in Figure 5.3. Note that the mesh in between the bodies is not displayed, but is taken to be fine near the bodies and coarse near the infinite element domain.

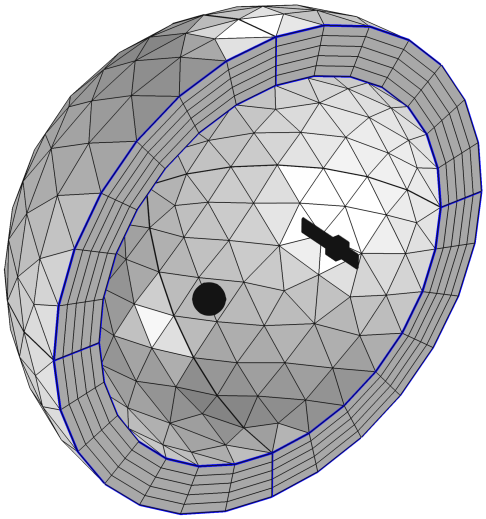

Figure 5.2: Comsol model with a mesh applied to the surfaces and volumes.

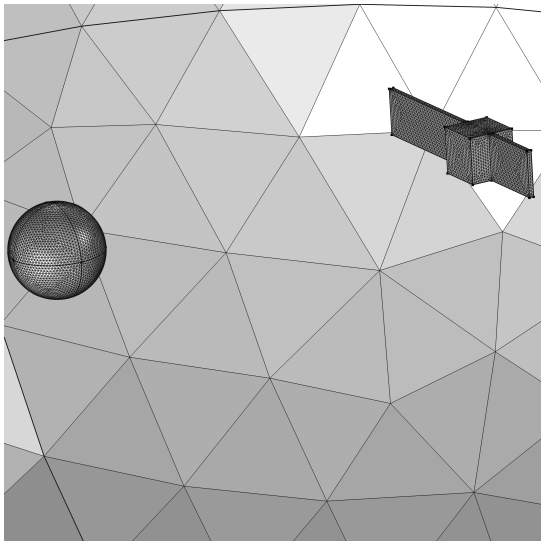

Figure 5.3: Close-up view of a mesh created for tug and debris.

5.4. Livelink and Cluster Simulations

A useful feature of Comsol is the Livelink with Matlab interface[48]. By setting up a client-server connection, a Comsol model can be created and directly loaded from Matlab. The benefits of this interface are simple implementation of calculations and data processing as well as extended controllability. For computationally heavy simulations with a parameter sweep, Comsol can run out of memory or simply occupy most of the computers processing power and memory. By running the model from Matlab, partial data can easily be stored and in case of an error or crash, the simulation can be resumed from this point onwards. Even though this provides better computational power, the fine meshes required for a satellite geometry require more processing power and memory. For this reason cluster computations are performed.
TU-Delft manages a cluster called HPC12 consisting of 1536 cores and on average 4 GB of memory per core. These cores are divided into nodes, where at most 48 cores can be used for one simulation. Within Comsol, there is the option to divide the parametric sweep into parts and let them calculate at different cores. The Comsol data can be directly loaded into the cluster via the SSH Secure Cell Client. During the simulation, a log file is created, which contains information that would normally be read from the Comsol Graphical User Interface (GUI). A single output file is created with all processed data in it, which can be retrieved from the client. After opening, the data has to be re-processed to yield the required potential and force curves. As the data has to be opened at a licensed computer, this process can take up to a few hours. It is therefore advised to create a sample output before running the simulation, such that minimal user input is required after loading the cluster data into the licensed computer. Additionally, all advanced rendering options can be turned off, and a fast CAD geometry creator can be selected. In case the TU Delft computers are used, also the temporary file directory should be changed as the factory settings limit the available memory.

5.5. Finite Element Simulation Results

A study is created within Comsol, where a stationary (stead) study is chosen for the geometry discussed in the previous sections. In order to generate a time-dependent potential signal, a parameter sweep is created, where the angle of the debris about the z-axis Θ is varied in the range of $[0, 190]$ degrees, with a step size of 5 degrees. Note that the zero angle of rotation is defined as where the large panel is directed along the x-axis. This corresponds to a rotation of the debris with -90 degrees as depicted in Figure 5.2. As the debris rotation is symmetric, the data points in this domain can be mirrored to the $[180, 360]$ degrees region, with the exception of F_y data, which also switches sign. Furthermore,

two extra data points (185 and 190 degrees) are added such that a check can be performed on the correctness of the data after mirroring. The step size is chosen as to generate enough data points for a smooth curve and good applicability of the RSEC method, while maintaining manageable computational cost.
For each step in the parameter sweep, the potential is registered at the probe locations. By applying the electrostatic force calculation in the model, also the force in three directions is determined. As the model generates a few million cell evaluations, the output file of a single parameter sweep becomes cumbrous. For this reason, the sweep is sectioned in 10 partitions and run on the TU Delft cluster. The results are concatenated and extended to the full rotation as described previously. As two data points (135 and 175 degrees) are corrupt, the output for these sphere rotations is linearly interpolated. The resulting force and potential curves can be found in Figure 5.4.

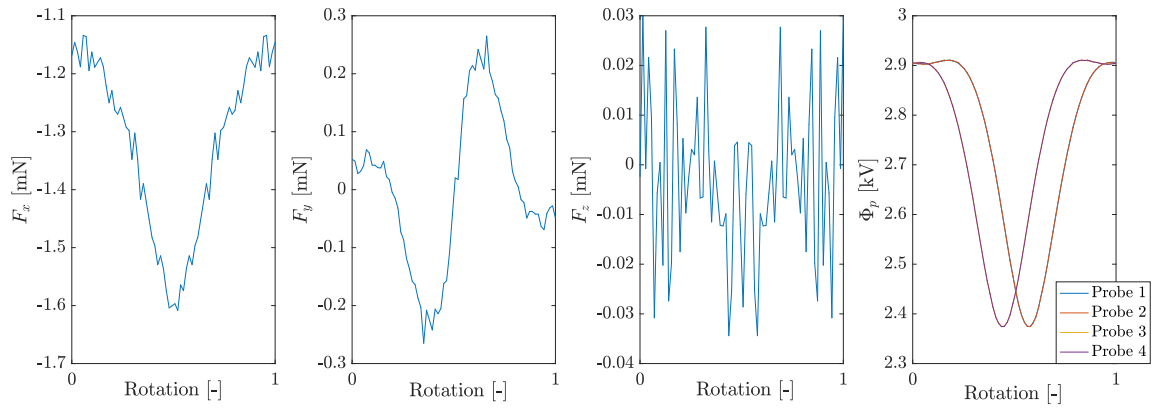

Figure 5.4: Raw force and potential data obtained from Comsol simulation.

From this figure, some observation can be made. First of all, the general shape of the curves is as expected; the registered potential is least positive where the large panel is close to the tug while the electrostatic force at this point is most negative. Furthermore, there exists an offset between the probe measurements as first the probes with positive y-locations will register the large panel coming closer, followed by the other two probes at a certain phase shift. As the debris is symmetric about the body y-axis and rotates about z, two probes with the same y-locations and mirrored z-location (i.e. probes 1 & 2 and probes 3 & 4) have identical potential measurements.
Secondly, the scale of the data is as expected. The force F_x which is used to manipulate the debris acceleration, is in the mili-Newton range, while the force F_y, which is used to detumble the debris, is almost an order of magnitude lower. Tue to the symmetry, the force in z-direction F_z is zero except for some noise.
Thirdly, the specific shape of each curve is as expected. As explained previously, F_x increases as the large panel moves closer to the tug. While the same hold for the potential field, the probes at negative y-location will also see the large panel moving further away for Θ smaller than a couple of degrees. This causes a small measured potential increase before the large decrease due to the panel coming closer to the tug.
The behavior of F_y is a little bit more difficult to explain. First of all, there seems to be an error in the computation, as the values at 0 and 360 degrees are not identical. Due to symmetry of the model at this rotation angle, these values should be zero. Aside from this error, the shape of the curve can be explained as following. The general shape of the curve is close to a sine as the force is zero for 0 and 180 degrees. Furthermore, as charge is allowed to move in the debris, it can reach the largest distance in y-direction at 90 and 270 degrees. However, as more charge moves to the panel when it gets closer to the tug, the peaks in the signal shift a bit towards 180 degrees. When the angle Θ increases beyond this point, the sign off F_y changes and the same behavior results in opposite direction.

Additional insight is gained from the potential field around the bodies. For a debris orientation where the larger panel is directed towards the tug, i.e. where the Coulomb force is largest, the potential field is retrieved from the FEA solver. The data is presented at specific nodes in the mesh for two slices; the xy-plane as well as the xz-plane. The results can be found in Figure 5.5.

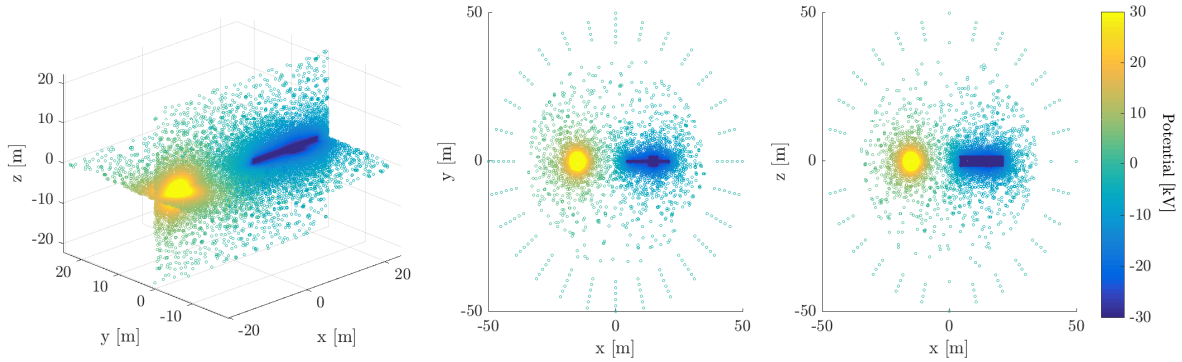

Figure 5.5: Potential field obtained from finite element data for a rotation angle of the debris of 180 degrees about the z-axis.

The field can be seen to vary from 30 kV at the surface of the tug, to 0 V at a specific point between the two bodies, to -30 kV at the surface of the debris. Radially outward of the bodies, the field drops with a $1/r$ relation. Corresponding with the very fine mesh on the surface of the bodies and a coarse mesh near the edge of the domain, the density of data-points drops with the distance away from the bodies. Furthermore, the potential within the bodies is manually appointed the maximum value of its corresponding surface, as the potential field within the bodies is not evaluated due to a lack of charge in these volumes.

5.6. Finite Elements versus Multi-Sphere Method

Inherently, there is a difference between the results from a FEA and the MSM as the latter resembles the charge residing on an object as a point charge. Instead of a continuous charge distribution, a step-wise distribution is therefore present. For the analysis described in the report, as based on the mission scenario, it is assumed that the tug characteristics can be calibrated and this information fed into to RSEC solver. In order to introduce the least amount of error as possible due to conversion of FEA to MSM representation of the tug in these simulations, a well known shape is therefore chosen; that of a sphere. Even though this shape allows for simple meshing and representation, the difference between FEA and MSM modeling requires adaptation of the sphere when applied in a MSM model. An accurate representation is proposed by Stevenson and Schaub where the golden section spiral distribution is used to populate the surface of the original sphere with a set of smaller spheres[3,49]. In order to find the optimal radius of these spheres, the difference in self-capacitance C of the tug for the two sphere populations can be minimized with the function f[3]:

$$f(R) = C_{\text{MSM}} - C_{\text{Single Sphere}} \tag{5.1}$$

where the only parameter that influences the self-capacitance for a given distribution of spheres is the radius R. The theoretical capacitance of a single sphere can be found from Equation 5.2a, while the capacitance of a set of spheres can be obtained from the Equation 5.2b.

$$C = \frac{R}{k_{\text{C}}} \tag{5.2a}$$

$$C = \frac{Q}{V} \tag{5.2b}$$

From analysis of the numerical results, there seems to exist an offset between the capacitance of a single sphere and that found from the FEA. For this reason, the following function is used to find the MSM sphere radius, where it is assumed that the FEA results can be considered the 'truth model' and the potential of the tug and debris is at 30 and -30 kV respectively.

$$f(R) = Q_{\text{MSM}} - Q_{\text{FEA}} \tag{5.3}$$

In Comsol, an integration over the surface of the bodies is performed in order to find the total charge Q on the body for a given rotational state of the debris. For an angle of 90 degrees, such as depicted in Figures 5.2 and 5.3, the charge on tug and debris is displayed in Table 5.3. For two distinct sphere populations, the radii corresponding to these charge levels is evaluated. These results can be found in the table as well. Note that the separation between the spheres on the debris is the governing factor for the sphere population. In order to maintain a homogeneous distribution of spheres on the debris, two separation distances are tested; 0.5 and 0.1 meter.

Table 5.3: Overview of optimal SMSM sphere radii based on charge found from FEA.

Body [%]	Charge [μC]	# Spheres [-]	Separation [m]	Sphere Radius [m]
Tug	11.238	30	-	0.5009
	11.238	50	-	0.3893
Debris	-12.639	407	0.5	0.1315
	-12.639	9587	0.1	0.3095

$V_{\text{deb}} = -30$ kV, $V_{\text{tug}} = 30$ kV, Debris angle = 90 deg

From the results shown in this table, it can be deduced that the larger sphere population provides a lot of overlap between the spheres, as the distance between spheres is 0.1 meter, while the optimal radius is 0.3 meter. Furthermore, comparing the Coulomb force curves for both sphere populations, a negligible difference was found. For this reason, the smallest population is used in simulations as the computational cost of this distribution is significantly smaller than that of the larger population.

5.7. Multi-axis Tumbling

Performing the FEA computations for the one-axis revolution of the debris took a full day, while retrieving and processing the data into the corresponding figures took another. In order to demonstrate the general applicability of the RSEC method, rotations about multiple axis need to be evaluated. As the expected computational cost is very large, an alternative has to be found. A feasible approach is to find the capacitance of a non-rotating model using a FEA of the tug-debris system, while performing the rotation using the corresponding SMSM model. Using the population of 30 spheres on the tug and 407 on the debris, as found in Table 5.3, the following SMSM model is constructed that compares with the previously described FEA model.

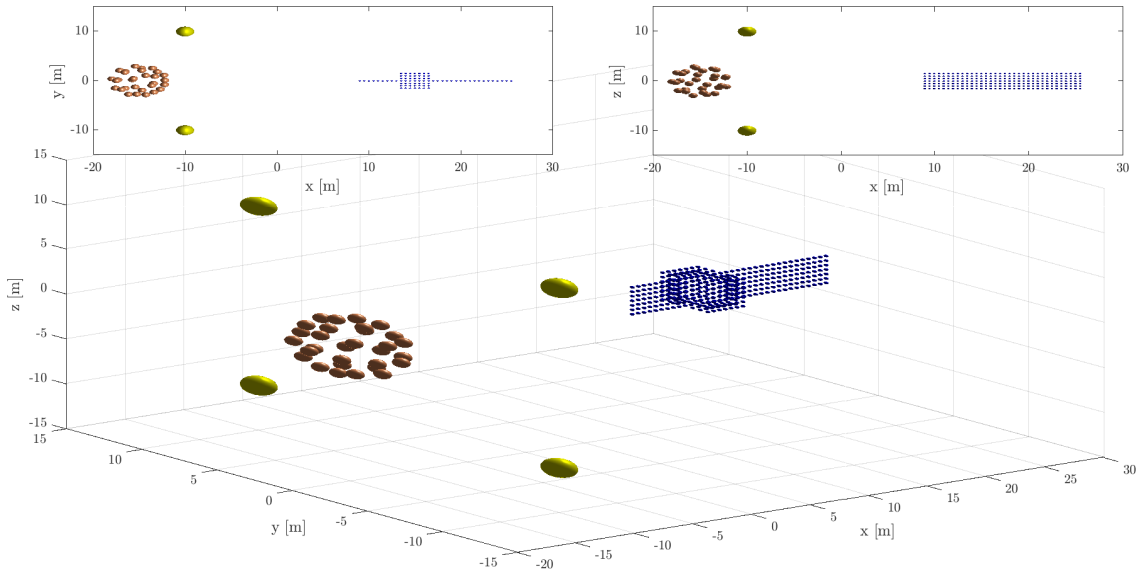

Figure 5.6: Sphere locations used in the SMSM simulation, with 30 spheres on the debris and 407 on the tug.

In this model, the golden-section spiral distribution used on the tug can be found in brown, the 4 probes in yellow and the homogeneous distribution of spheres with a separation of 0.5 meter in blue. Using this SMSM geometry, the potential field around the bodies can be evaluated and compared with the FEA results. In the bottom row of Figure 5.7, the potential field of the SMSM can be found for two slice plots in the xz and xy plane. The same slice plots can be found in the top row for the results of the FEA, as was already displayed in Figure 5.5.

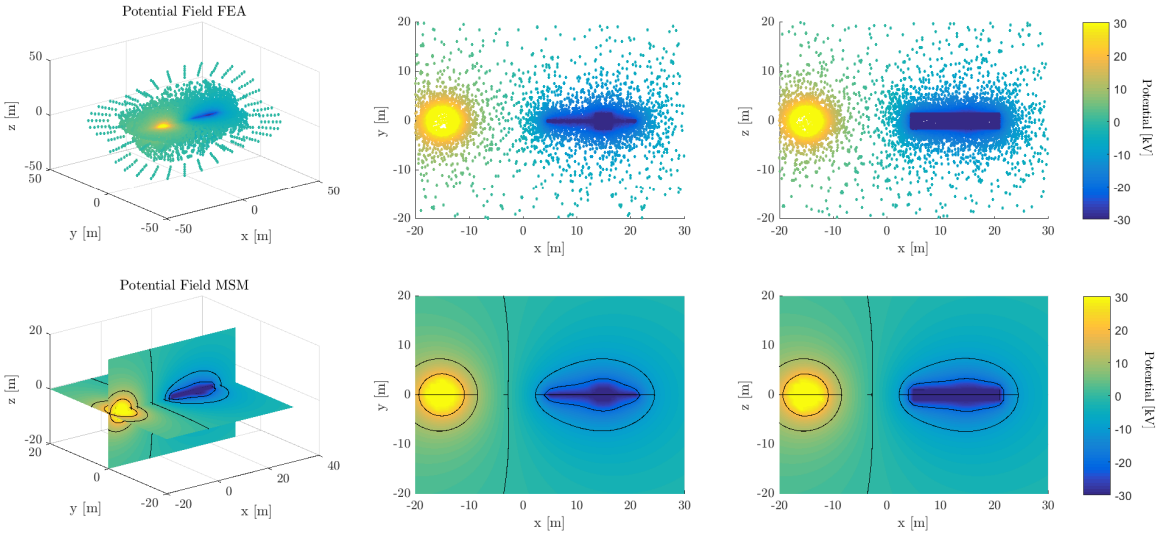

Figure 5.7: Potential field around tug and debris obtained from FEA (top row) and MSM (bottom row).

In this figure, the difference between a sphere representation and panels as in the FEA can be noticed. The latter has sharp edges, while the SMSM field decayes more smoothly near the boundary of the debris. At a distance from the bodies, both fields 'smooth' out, as they would when resulting from a point source. As the charge on the bodies resides on the surface, the inner volume of both bodies is manually given the maximum value found on its surface, as to maintain a clear visualization.

In order to compare the potential field obtained from the FEA and that of the MSM, the same data points have to be used. As the MSM data is contained within a uniform grid, it allows for quick interpolation. Using the Matlab built in function *interp2*, a two dimensional interpolation can be performed[50]. The interpolated potential field can be found in the bottom left of Figures 5.8 and 5.9. The difference between the interpolated MSM and the FEA potential field can be found in the bottom right of the figures. It should be noted that some outliers are filtered out in order to obtain a clear visualization. The 95th percentile of the data is shown, such that most of the data is still present and valid conclusions can be drawn.

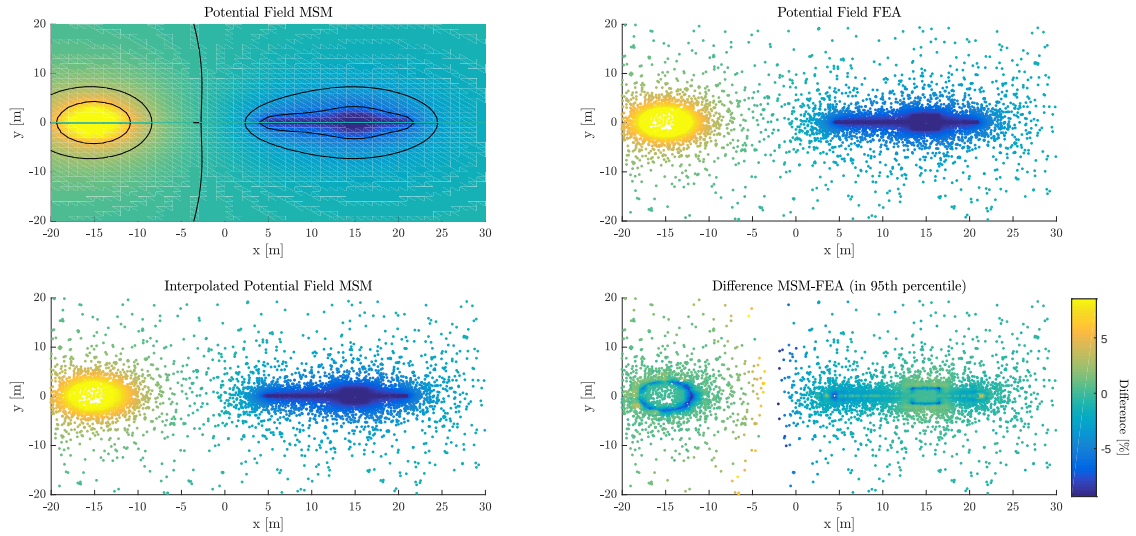

Figure 5.8: Potential field in the xy-plane obtained from FEA as well as MSM are displayed on the top row. In the bottom row, the MSM data interpolated at the same points as the FEA and the error between the two methods at these points.

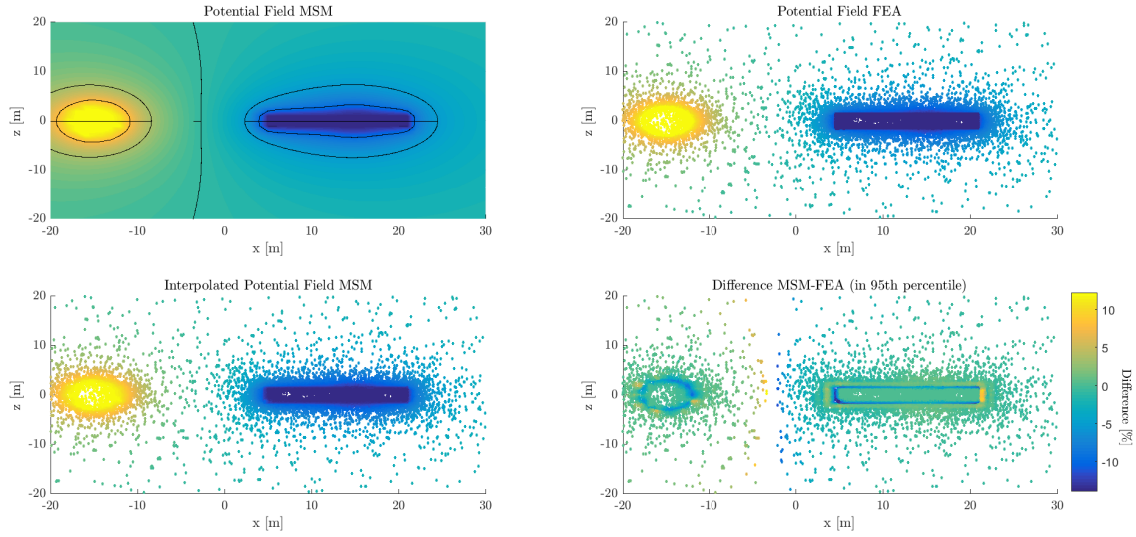

Figure 5.9: Potential field in the xz-plane obtained from FEA as well as MSM are displayed on the top row. In the bottom row, the MSM data interpolated at the same points as the FEA and the error between the two methods at these points.

Some observations can be made based on these figures. First of all the potential difference is largest at the surface of the bodies, as this is where the charge is residing in the FEA model, whereas the MSM model introduces the charge at the center of the spheres in a step-wise distribution. Secondly, in

the region where the potential field is near-zero ($-5 < x < 0$), the error is larger, as a small absolute deviation results in a large percent error. As the potential measurements are taken at $x = -10$, the field error should be minimal at these locations. From the figures, it can be seen that the potential field here is indeed comparable.

Taking this model as the new 'truth model', a multi-axis rotation can be performed. An initial debris orientation is taken as depicted in Figures 5.2 and 5.3, i.e. with the panels perpendicular to the separation direction between the bodies. A rotation with the Euler angle rates $\dot{\phi}$, $\dot{\theta}$ and $\dot{\psi}$, as described in Section 3.4, is then performed. As input for the numerical simulation, the following angular rates are applied such that a full revolution back to the original debris orientation is performed:

$$\dot{\Psi} = 4\dot{\Phi}, \quad \dot{\Theta} = 2\dot{\Phi}$$

Over a full rotation, with probe locations as given in Table 5.1, the potential measurements are obtained and displayed in the left-hand side of Figure 5.10. The Coulomb force between the bodies corresponding to this rotation can be found in the right hand-side of the figure.

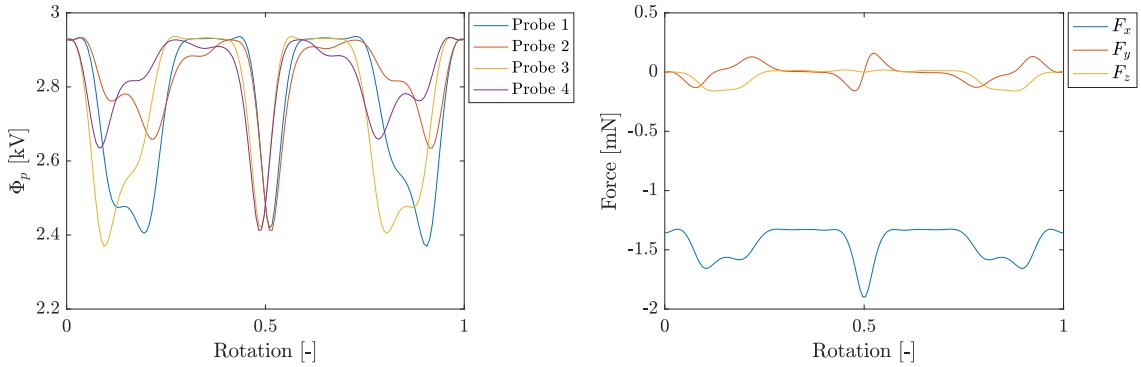

Figure 5.10: Probe potential and force curves obtained from the SMSM simulation.

Whereas the FEA results showed noise in the force curve as well as a non-continuous F_y curve, the SMSM results provide a smooth and continuous curve. Comparing the curves with that of the FEA displayed in Figure 5.4, a comparable magnitude in both force and potential signal can be seen. In the force curves, some sections seem almost constant, but in fact these parts are still varying (as can be seen in the corresponding potential signals), but due to the geometry of the debris this variation is marginal.

6

Numerical Simulation and Results

This chapter describes the performance of the Remote Sensing for Electrostatic Characterization (RSEC) method based on numerical simulations. Firstly, by applying the method on a Multi-Sphere Method (MSM) truth model, the force error resulting from the method is tested against a variation of spheres, their location and separation distance. Secondly, the method is applied for the two models described in the previous chapter; the Finite Element Analysis (FEA) and the multi-axis tumbling Surface Multi-Sphere Method (SMSM) model. Based on the validation data of the FEA, the optimal number of representative MSM spheres is found. Furthermore, the force error with respect to the FEA data is used to determine the variation in reorbiting time and fuel cost for a representative mission scenario.

6.1. Performance Sweep based on MSM Truth Model

With use of a truth model consisting of MSM spheres, the performance of the developed RSEC method is tested for a variation of parameters. The benefit of using a MSM truth model, is that many different debris geometries can be evaluated quickly. In order to do so, the debris population is randomly varied between 5 and 15 spheres, their locations between -10 and 10 meter in x,y and z direction and the radii are bounded between 0 and 1 meter. The analysis is performed 50 times, and for each simulation run, the maximal and mean force error of the best-fit model is displayed in Figure 6.1. Note that within the RSEC application the three methods described in Table 4.1 have been applied. Furthermore, the tug consists of three spheres and the debris is rotating with $\dot{\phi} = 3\dot{\psi}$ and $\dot{\theta} = 2\dot{\psi}$.

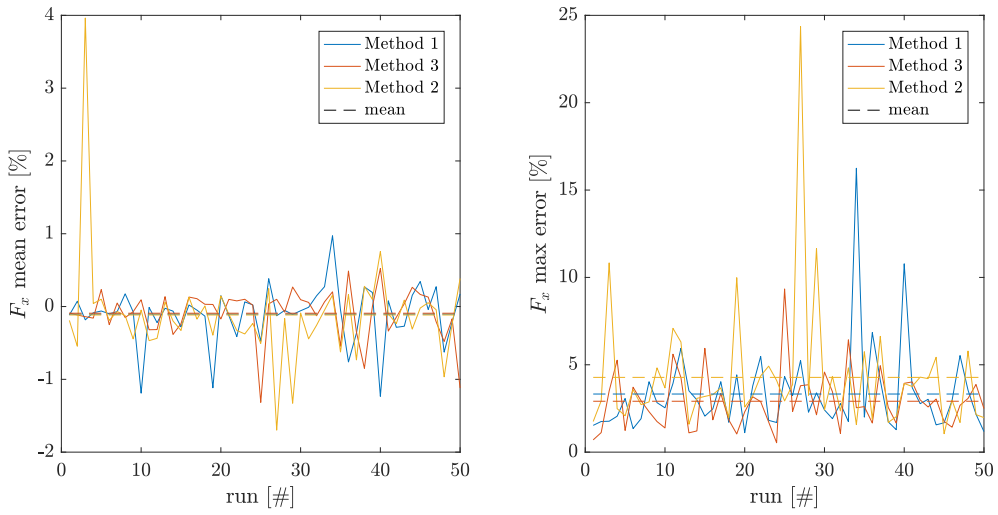

Figure 6.1: Mean and maximum force error in x-direction for a variation of debris sphere locations and number.

From this figure, it can be concluded that all three methods are able to accurately predict the force obtained from the truth MSM model. Except for a few outliers, the mean error lies mostly within a percent margin.

6.2. COMSOL Results

In Chapter 5, a description is given of the Comsol model that is used to validate the constructed RSEC method. The data obtained from the parameter sweep simulation can be used as input, as to find the best fitting sphere model that corresponds with this tug-debris system. In order to find this result, methods 1 and 2 are applied, as described in Chapter 4. As has been indicated, the tug potential and radius of the FEA is not the same as that of the equivalent MSM model. Therefore the radius of the tug has to be adapted from 3 to 2.9 meters, while the potential is changed from 30 kilovolt to 29.5. By applying the RSEC method, the following measured potential is obtained.

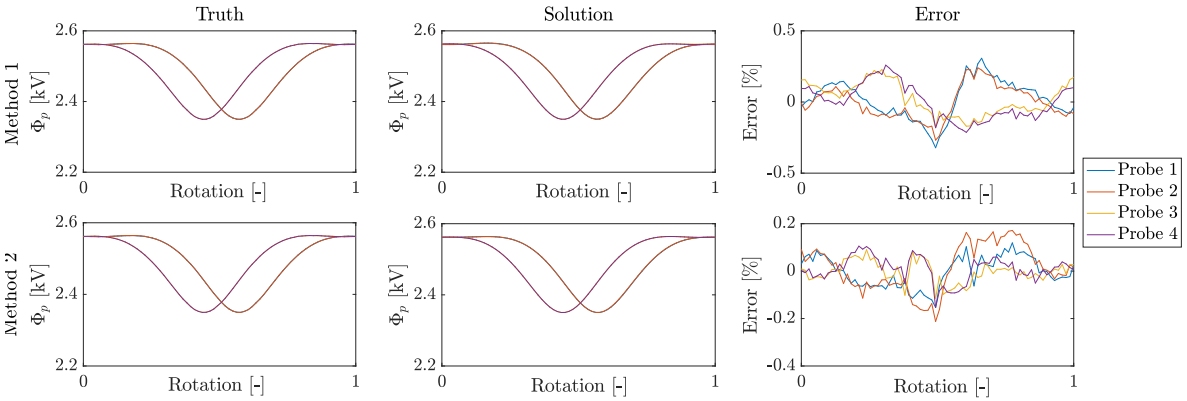

Figure 6.2: Resulting potential curves and error with respect to the FEA simulation data.

Figure 6.2 shows that both methods are capable of matching the potential obtained from FEA and RSEC to very high accuracy. The resulting force curves due to the best-fit sphere model, can be found in Figure 6.3. As the force in x-direction is of most importance, the error curve has been plotted separately

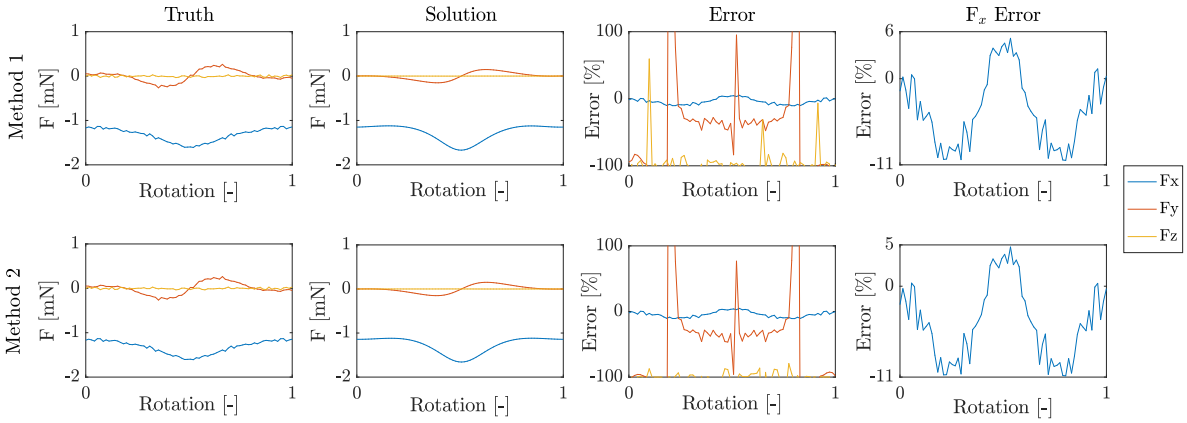

Figure 6.3: Resulting force curves and error with respect to the FEA simulation data.

Even though the resulting MSM model is not able to catch the F_y and F_z forces accurately, the influence is due to their low magnitude marginal. The most important parameter F_x is however been resembled within a good error margin. In both Figures 6.2 and 6.3, a clear sine wave can be observed. The origin of this wave can be attributed to the inherent nature of the solver to place spheres at the locations

where their influence is largest, i.e. on the ends of the panels, as is discussed in Section 4.2. In Figures 6.4 and 6.5, the location of the spheres due to both solving methods is displayed.

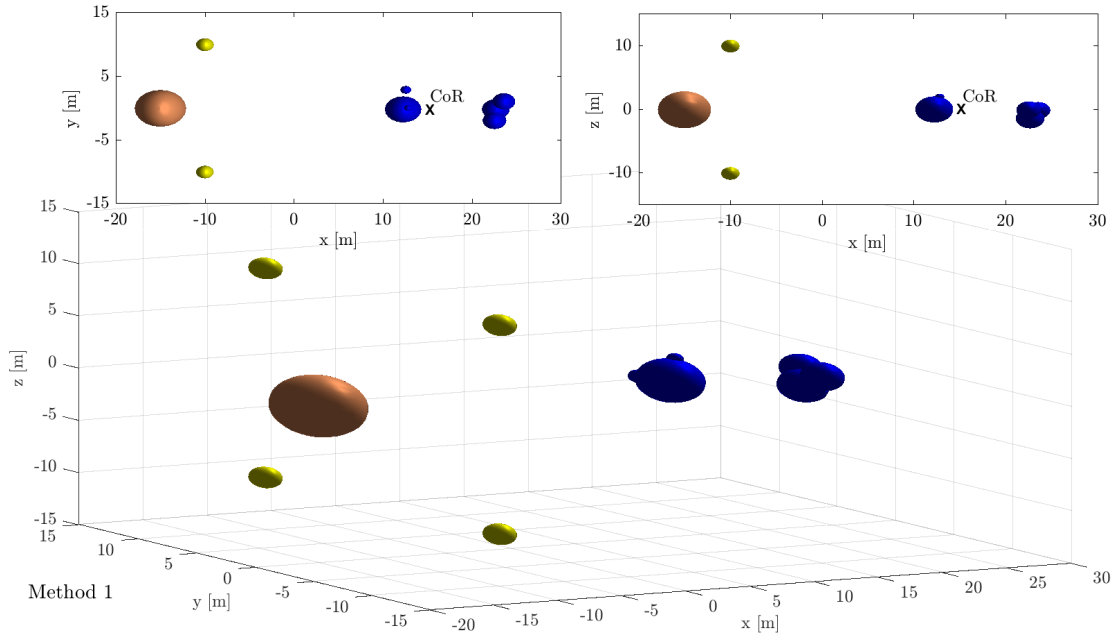

Figure 6.4: Resulting sphere placement for method 1 given a debris sphere population of 6.

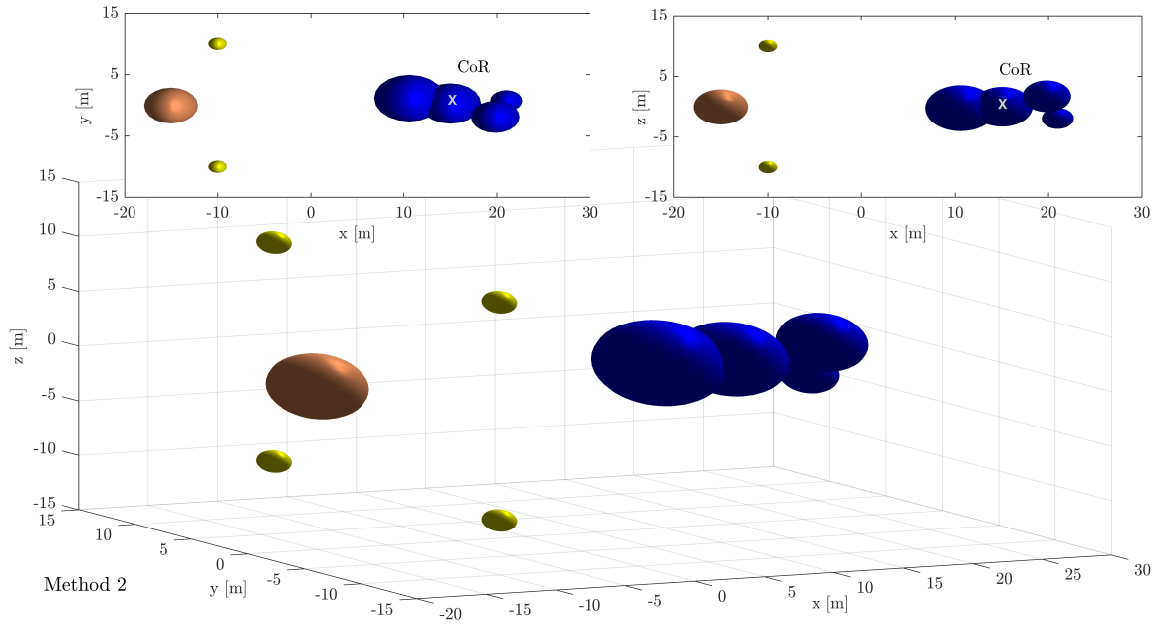

Figure 6.5: Resulting sphere placement for method 2 given a debris sphere population of 6.

Especially for the first solving method, the separation between spheres is quite distinct. As spheres are mainly located near the places of most influence, the times where the influence is less, the error grows. The biggest errors can therefore be expected around 90 and 270 degrees, exactly where F_y is largest, which also explains the F_y error peaks in the third row of Figure 6.3. From the F_x error curve, it can also be noticed that the error is not centered around 0%. As the input tug radius and potential is an approximation, the total force curve is scaled, in the same way the potential was scaled in Figure 3.3.

Therefore, better calibration of the tug characteristics will result in better force prediction performance, while keeping the potential prediction the same. An example for this will be given in the discussion of the SMSM results. It is of interest however, to note that mis-predicting the tug characteristics can be beneficial to the Electrostatic Tractor (ET) application. As will be discussed later in this chapter, over-prediction is preferred over under-prediction as the latter can cause a collision between tug and debris. For this reason, a forced mis-prediction of the tug characteristics might prove useful. Further investigation in the effect of this mis-prediction is however required.

6.2.1. Performance sweep

Now the model has proven to provide an accurate force prediction, it is of interest to see how the results vary over different input parameters. One of the most influencing parameters is the size of the sphere population used to represent the debris. If a single sphere is already capable of providing the same accuracy, there is no need to add a multiple. The mean and maximum absolute force error have been displayed against a varying population size in Figure 6.6. Furthermore, the data is divided in the two optimization methods.

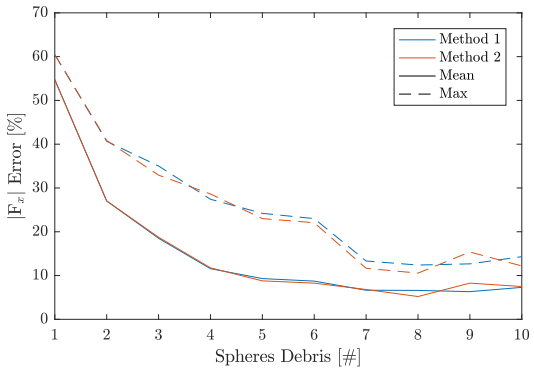

Figure 6.6: Variation of sphere population representing the debris versus mean and maximum absolute force error in x-direction.

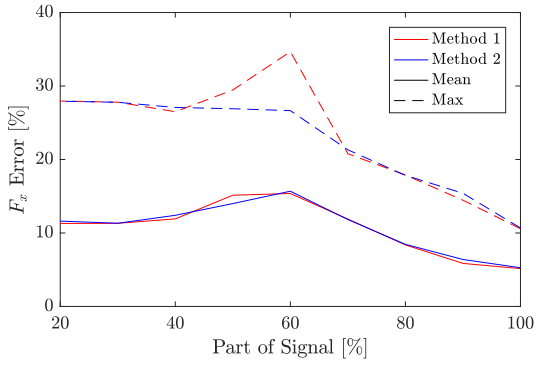

Figure 6.7: Mean and maximum error in force prediction over a full rotation, based on two methods where only a part of the full signal length is applied.

A clear conclusion can be drawn from this figure. For a small sphere population, the error grows almost exponentially, while there is almost no reduction in error by using more than 5 spheres. Even more so, from planar simulations performed by Engwerda *et al.* it was concluded that a very large population will add in error[23]. The tail in Figure 6.6 also seems to indicate this result. It is of interest to see how this result fits in with previous work on sphere population optimization, where it was found that for a known geometry the best solution comes from many uniformly placed spheres with constant radius[3].

A second performance sweep is applied for the case where not a full signal is available. Ranging from only 20% of a full revolution, i.e. 72 degrees, to a full revolution, the mean and maximum error in the predicted force is evaluated for both method 1 and 2. The results are displayed in Figure 6.7. The results show that for a simple rotation about one axis, not the full signal is required to establish an accurate MSM model. However, for more complex geometries and rotations, the results are expected to decrease more rapidly with a larger limitation to the observed signal. Performing these simulations is part of the recommendations of this thesis however.

6.2.2. Resolving Rotation Rates

As the model evaluated with the FEA consists of debris rotating about a single axis, it opens up the possibility to deduce the rotation rate from the potential measurements instead of relying on additional Light Detection and Ranging (LiDAR) observations. By performing a Discrete Fourier Transform (DFT) of the potential measurements, the rotation frequency can be found. In order to do this, measurements

over multiple full revolutions of the debris are required. A quick method to find the DFT is by means of Matlab's built in *FFT* function[51]. This function translates the input signal in the time domain to its Fourier transform in the frequency domain. In order to demonstrate this feature, the potential measurements obtained from the FEA simulation are sampled such that two full revolutions are present in the signal. Assuming a rotation rate of 10 degrees per second, the signal given in the left-hand side of Figure 6.8 is obtained.

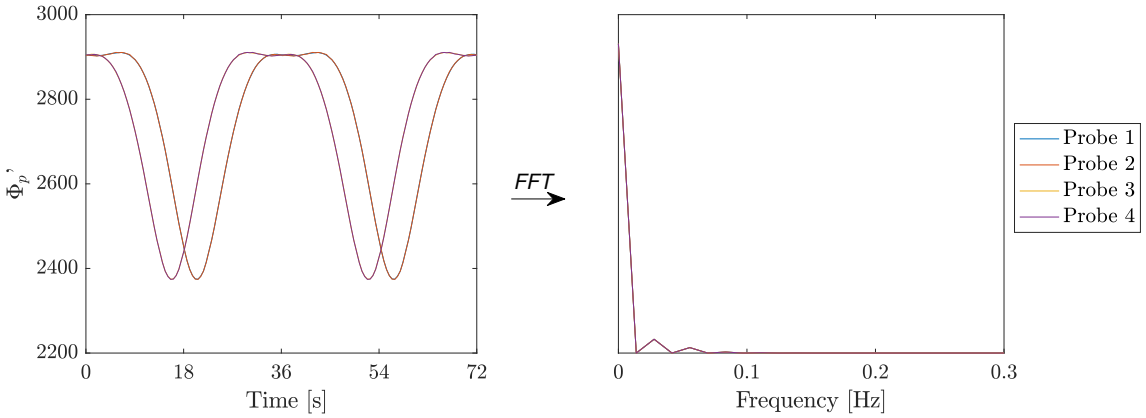

Figure 6.8: Application of DFT to the normalized potential measurements obtained from the FEA simulation for two full rotations at 10 degrees per second.

In the right-hand side of this figure, the DFT can be found. Neglecting the zero-frequency peak, the first peak in the frequency domain corresponds to the debris rotation rate. This peak can be found at a frequency of 0.0278 Hz, which indeed translates to 10 degrees per second.

Even though the correct result is obtained for this case, most other mission scenarios will introduce problems to this method. For sampling rates of only a few full revolutions, the estimated frequency can differ largely from the truth. If for instance 2.5 full revolutions are sampled in 72 seconds, the resulting rotation rate will be 10 deg/s, instead of 12.5 deg/s. This error is reduced by evaluating many full rotations, but this introduces its own error. Tumbling rates of debris are in general not constant and even less when the ET is changing the kinetic energy of the debris. Therefore the potential measurements will significantly differ over multiple full rotations.

A second issue complicating the application of the DFT is the geometrical properties of the system. Consider the debris geometry discussed so far, but with both panels the same length. During one full revolution of the debris, a probe will now register a peak potential twice, instead of a single peak and a lower value 180 degrees later. Even more so, for complex shapes and multi-axis rotations, the distribution of charge can cause probes to register peaks at different moments, not related to each other. In order to avoid measuring the effects of local charge phenomena, probes should therefore be placed close to each other. Aside from the technical issues this gives rise to, even then not all rotation rates can be solved for. In conclusion, application of LiDAR to find the rotation rates is more robust and viable option.

6.3. SMSM Results

Based on the potential signals obtained in the SMSM numerical simulation, the RSEC method is tested for a rotation about all body axis. The tug SMSM model consisting of 30 spheres is taken as input assuming this distribution can be obtained from calibration in a applicable mission scenario. Furthermore, the potential of the tug is fixed at 30 kV, the separation distance r_{sep} at 30 meter, the debris population at 6 spheres and the orientation of this body is assumed to be known from LiDAR measurements. In order to increase optimization performance, the spheres on the debris are constraint according to the conditions described in Section 4.3. By applying the same two optimization methods as for the FEA, i.e.

the two step optimization (Method 1) and optimization from random input (method 2), the potential signals are matched as displayed in Figure 6.9.

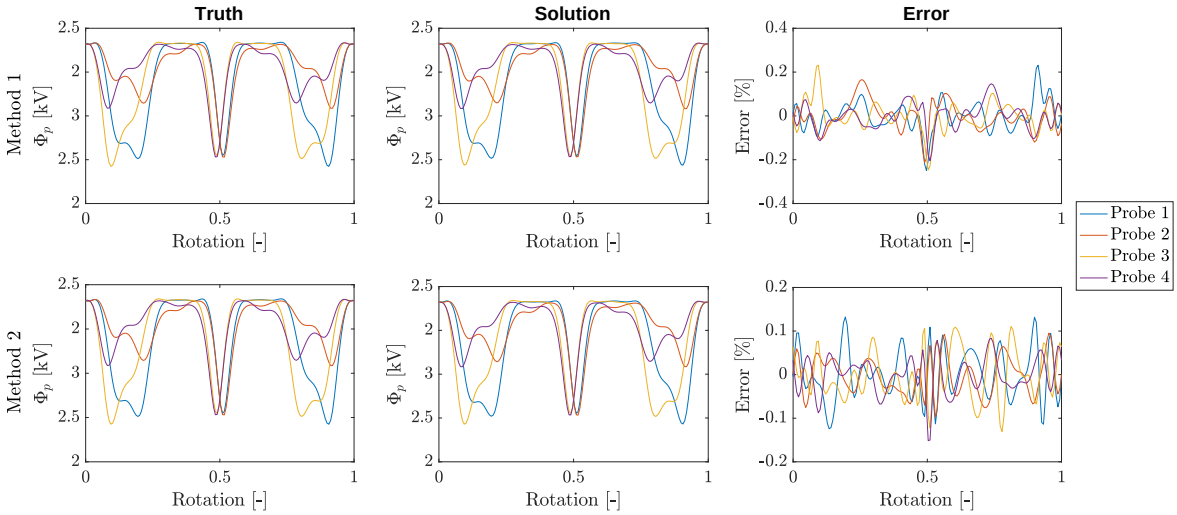

Figure 6.9: Comparison of probe potential between RSEC and FEA over a full revolution of the debris.

In this figure, the top row shows (from left to right) the truth SMSM signals, the optimized equivalent and the error between the two for method 1. The bottom row shows the same curves for the method 2. From this figure, it can be concluded that both methods perform comparably well and are able to find a optimal sphere distribution that resembles the potential field within percent error. No distinct outliers can be found in the error curve, indicating the solver is well able to fit spheres to match the global potential field.

The performance of the RSEC method, should be evaluated based on the ability to match the Coulomb force and therefore the electrostatic behavior of the debris. The optimized force curves corresponding to potential signals described previously, can be found in Figure 6.10.

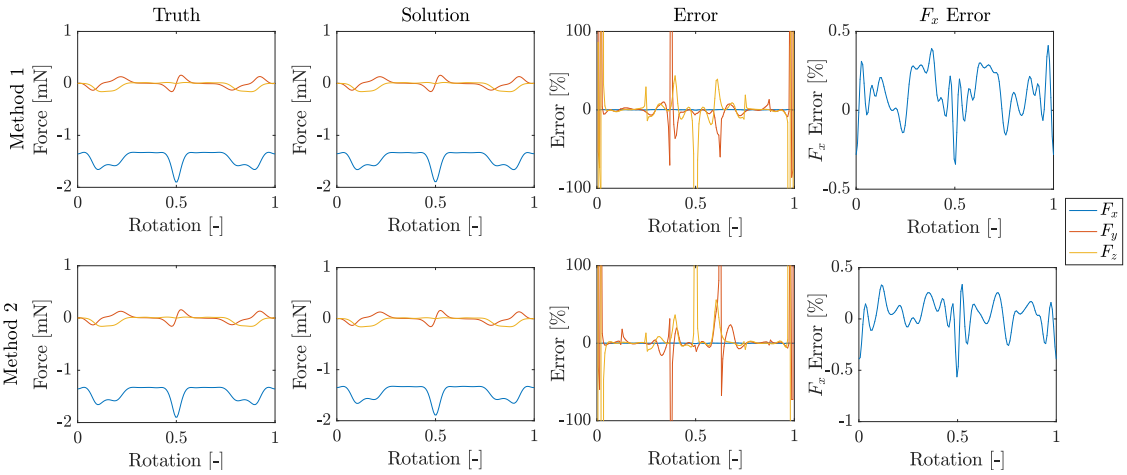

Figure 6.10: Comparison of force between RSEC and FEA over a full revolution of the debris.

Again, the results from method 1 are displayed in the top row, while the bottom row applies to method 2. The left-most plots shows the force curves obtained from the SMSM simulation, while the plots adjacent show the force curves resulting from the optimized sphere distribution. The plots in the third column shows the force error for all three Cartesian axis displayed in Figure 5.6. As the most important

force for application of the ET is the F_x force, and the other two force components are negligible, the error in F_x is additionally displayed in the right-most plot. Due to the F_y and F_z force components attaining zero, or near-zero, values for distinct debris orientations, the percent error is very large. As the F_x force component is always non-zero for two charged objects, the right-hand side error plot is of more interest. From this plot, it can be concluded that both methods are performing very well, with less than percent error. As the results from the optimization based on FEA data provided clear conclusions on which geometrical features of the debris introduced the largest error, the results discussed in this section are harder to interpret. Comparing the error curve with the truth signal, it can be seen that for both methods a peak occurs for the debris orientation introducing the largest absolute force in x-direction. Furthermore, whereas the results from the FEA optimization showed a clear over-prediction of the force due to faulty tug calibration, the implementation of the tug SMSM in this case does not lead to specific under or over-prediction of the force. This also indicates that the results described in Section 6.2 can be improved considerably when performing correct tug calibration and even higher fidelity FEA simulations.

The optimized sphere locations corresponding to the results described previously are displayed in Figures 6.11 through 6.13, where the first two figures display the locations found from method 1, and the third figure those from method 2. For each of the figures, an orthographic view of the two body system is given, above which the xy and xz planes are displayed for a better overview. Furthermore, the Center of Rotation (CoR) is indicated in these figures, where the tug is colored brown, the probes yellow and the debris in blue.

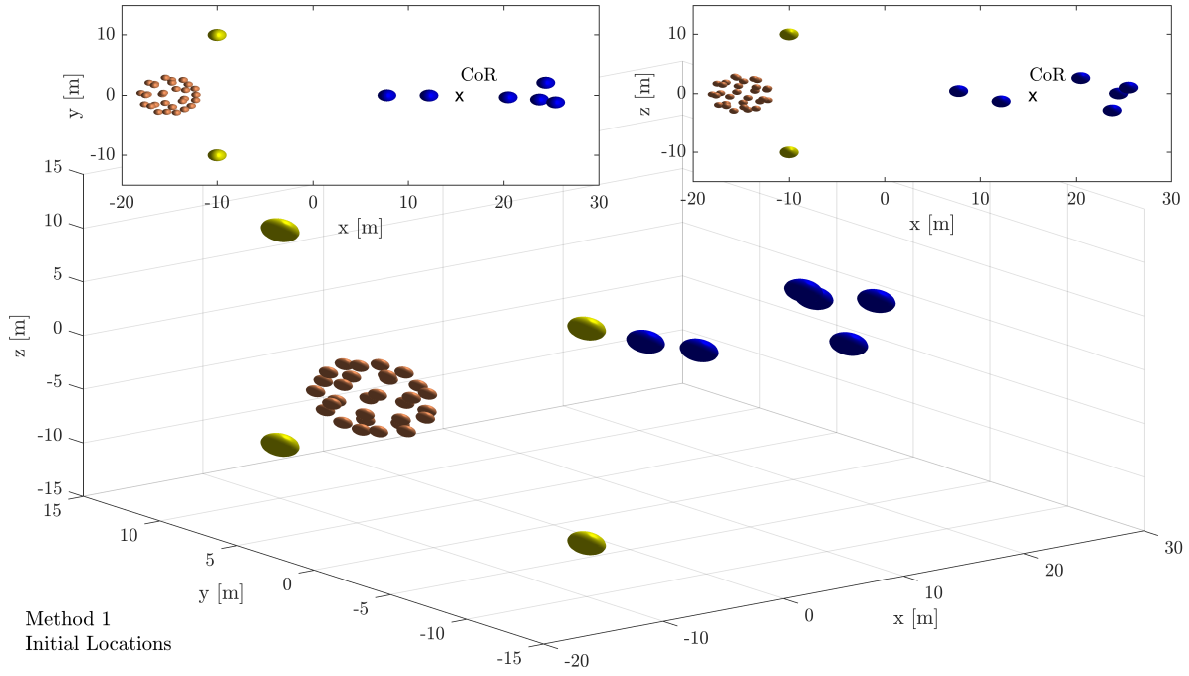

Figure 6.11: Optimized sphere locations obtained for unit debris radius and potential, where the population is 6. These spheres are used as input to obtain the results from method 1.

In Figure 6.11, the optimized sphere distribution is shown for the first step of method 1. The optimization is performed for unit sphere radii and unit potentials. These resulting sphere locations are used as input to the initial state vector for optimization performed in the second step of method 1. It is of interest to see, that without significant contribution of sphere radii and potentials, the solver is already able to place the spheres at locations on the debris that are close to the optimal ones found in the second step. These final locations can be found in Figure 6.12.

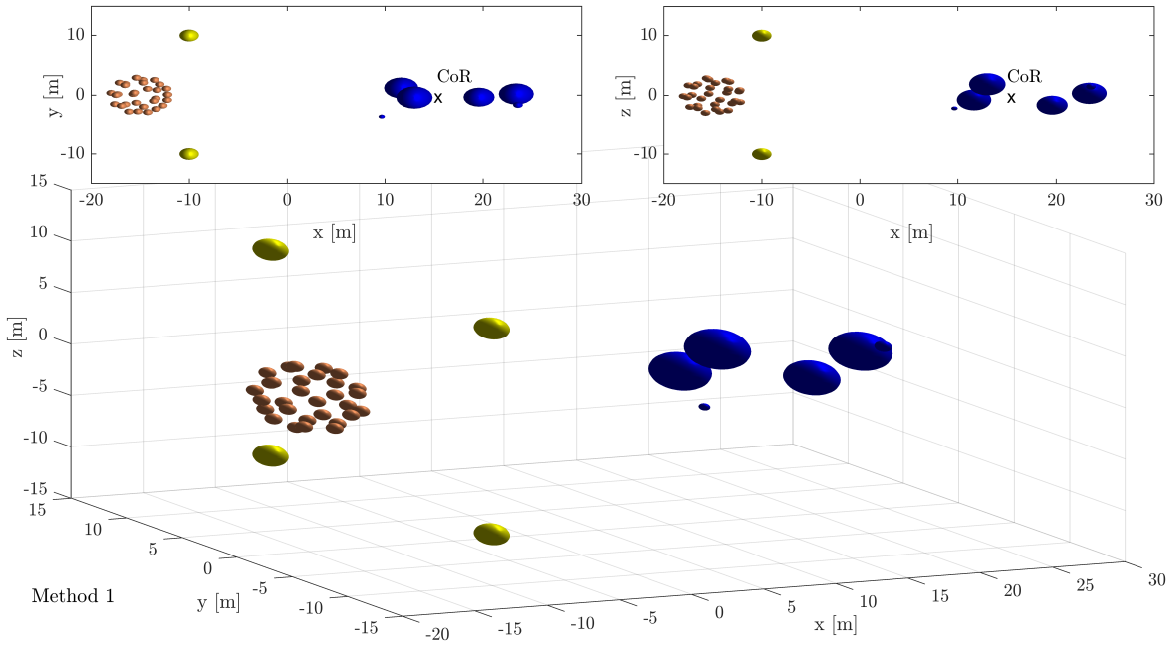

Figure 6.12: Optimized sphere locations obtained from method 1 for a debris population of 6.

From Figure 6.12, it can be concluded that as for the FEA results, the spheres are located at the far ends of the debris. As for single-axis rotation, these elaborate tumbling motions cause the largest charge transfer to take place at the far ends. This causes the shape of the potential signals to be influenced most by these parts of the debris and therefore causes also the optimizer to place spheres at these locations. Furthermore, the sphere radii are mostly comparable, while for the given geometry, a large sphere in the center body and multiple smaller spheres on the panels could be expected.

Starting from a complete random distribution, such as in method 2, the optimized sphere distribution is comparable to that of method 1. The results of this method can be found in Figure 6.13.

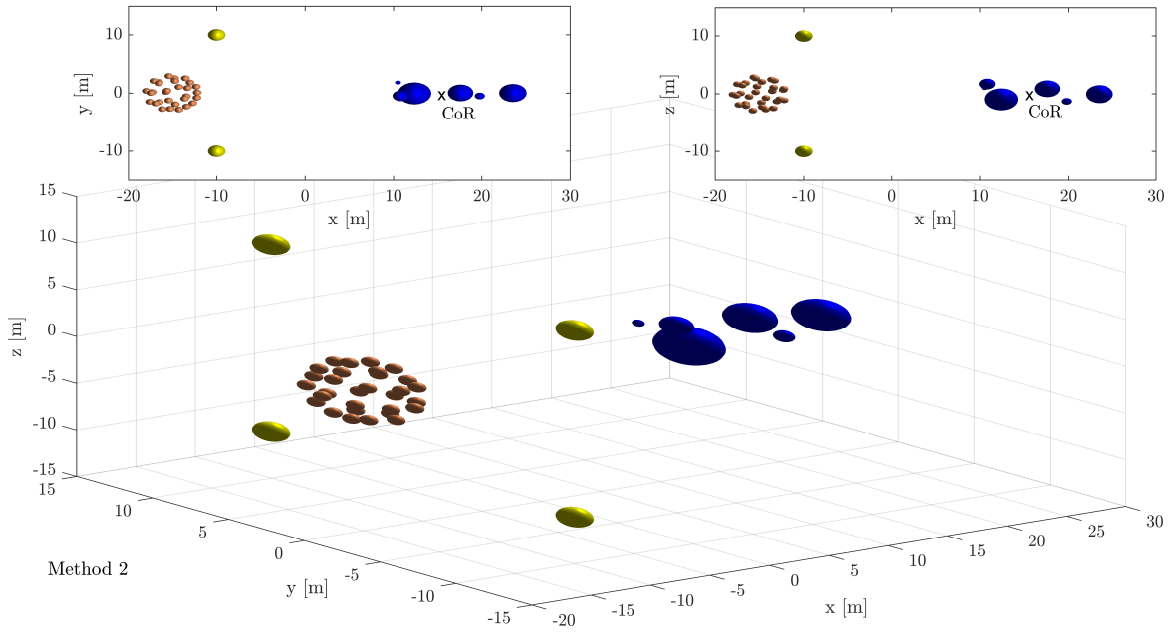

Figure 6.13: Optimized sphere locations obtaind from method 2 for a debris population of 6.

A relatively homogeneous distribution of spheres over the debris can be found in Figure 6.13, but also largely comparable to the results found for method 1 and those of the FEA simulation. Three spheres with large radii are spread over the body, while three smaller spheres act as adjustments as to improve the similarity of the potential field due to the spheres with that of the truth model. The limited effect of these additional spheres emphasizes the results found in the parameter sweep; increasing the debris sphere population is not a guarantee for better performance.

6.3.1. Variation of Rotation Rates

In order to validate the general applicability of the RSEC method for other tumbling orientations, as well as to show that for multiple simulations the method provides the required accuracy, a variation of rotation rates is simulated. For each of the simulations, a full revolution performed as to end up at the initial position of the debris. The rotation rates are normalized, such that a value of 1 corresponds to a single full revolution within the simulation time. Furthermore, the error is force prediction is given a the mean and maximum value of the data. In order to obtain these figures, the absolute value of the error has been used. Therefore the displayed results can either be due to over, or under-prediction. An overview of the results can be found in Table 6.1.

Table 6.1: Overview of error in Coulomb force prediction for a variation of normalized rotation rates, obtained from the two solving methods.

Rotation Rates			Method 1		Method 2	
$\dot{\Phi}$	$\dot{\Theta}$	$\dot{\Psi}$	Mean F_x Error	Max F_x Error	Mean F_x Error	Max F_x Error
[-]	[-]	[-]	[%]	[%]	[%]	[%]
4	2	1	0.22	1.25	0.43	1.68
4	2	1	0.26	1.47	0.26	0.98
4	1	2	0.45	2.26	3.44	8.76
4	1	2	0.35	1.48	3.89	12.76
2	1	4	0.89	3.92	1.03	2.12
2	1	4	3.22	8.94	0.55	2.31
2	1	2	0.21	0.96	1.40	2.95
2	1	2	0.34	1.12	0.16	0.76
1	1	1	0.19	0.47	0.20	0.48
1	1	1	0.37	0.85	1.47	2.37

Analyzing the results in this table, it can be concluded that for most rotation rates, the mean error of force prediction is within percent error, such as shown in Figure 6.10. Some outliers exist however, for instance for the rotation rates described in the third and fourth row of the results. For this simulation however, the first method does provide an accurate result. The same behavior is found in the fifth and sixth row, but now the second method proves more reliable. Therefore it can be concluded that it is wise to either perform multiple RSEC optimization runs for a specific measured potential over time, or to apply both methods and use the best fitting results.

6.4. Mass Budget

So far, the metric for model performance has been the error in force prediction. In order to study the performance of the model when implemented for an actual mission scenario, this metric can be related to fuel cost and reorbiting time by implementing the control law proposed by by Hogan and Schaub[5]. As this control law describes the relative motion between the bodies in the application of

the ET, while introducing a charge-estimation error, this control-law can be exploited to test the RSEC model performance. The control law describes the relative motion between tug and debris in the Local Vertical Local Horizontal (LVLH) and spherical reference frame $\mathcal{S}$. An initial separation distance L and angles Θ and Φ describe the geometry of the two bodies, as can be found in Figure 6.14.

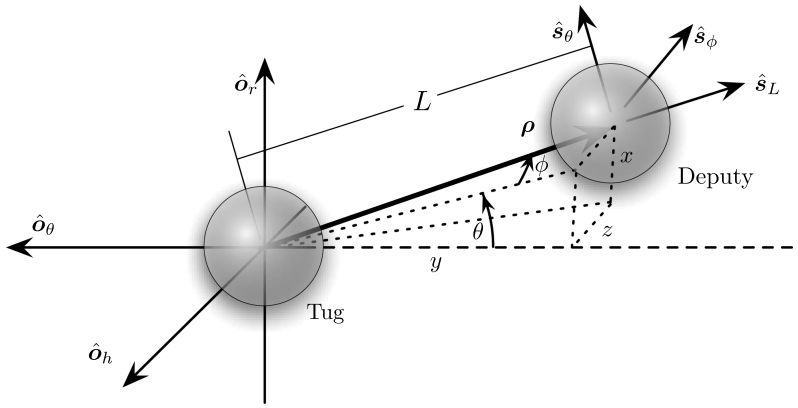

Figure 6.14: Graphical representation of the LVLH and Spherical coordinate frame $\mathcal{S}$, as obtained from Hogan and Schaub [5].

The control law describes the required control acceleration such that a state vector $\mathrm{X} = [L, \Theta, \Phi]^T$ is forced to some reference value X_{ref}. As the most efficient orbit raising maneuver takes place in-plane, this state vector is most likely in the form of $\mathrm{X}_{\text{ref}} = [L, 0, 0]^T$. The control acceleration consists of two parts; the inter-body Coulomb force, as well as the thrust applied by the tug's propulsive system. The magnitude of these two forces is largely influenced by the separation between the two bodies. As this distance decreases, the Coulomb force increases and therefore also the required thrust settings on the tug and vice versa. Now consider a under-prediction of the Coulomb force in the model. Hogan and Schaub describes that in such a case the acceleration of the debris towards the tug can be larger than the maneuver of the tug itself, introducing collision probability. For the opposite case, the tug can find itself losing 'contact' with the debris. Furthermore, as the thrust settings go down for larger separations, the reorbit time takes longer.

This introduces a new metric to test the RSEC performance. Based on the force error and thus charge prediction, a mass and time budget can be evaluated based on a mission scenario. Introducing the force and representative error portrayed in this report to the control law, the time to reorbit and fuel cost can be determined. As the Coulomb force depends on separation distance, the SMSM introduced in Section 5.7 is used to find the force for each distance L=r_{sep}. The debris model is assumed in a detumbled state, such that the panels are perpendicular to L, i.e. as displayed in Figures 5.2 and 5.3. Choosing a reference state vector $\mathrm{X}_{\text{ref}} = [20, 0, 0]^T$, mass of the tug of 1000 kg and all other parameters as in [5], the evolution of spherical coordinates is obtained as depicted in Figure 6.15.

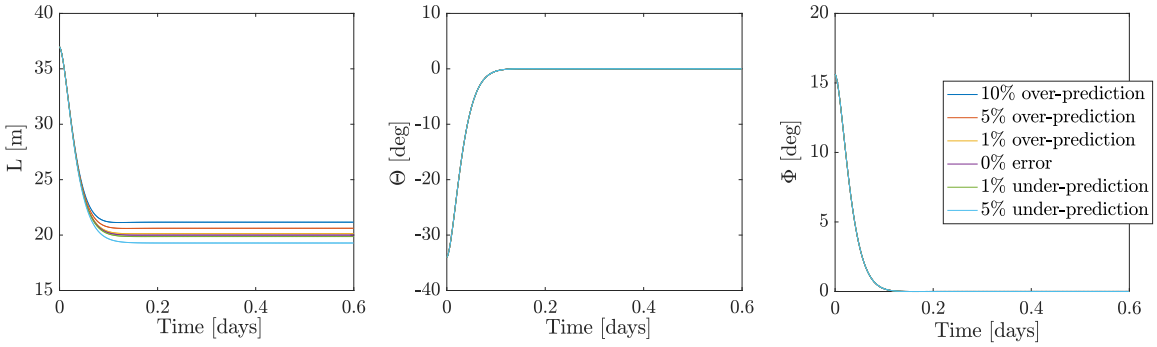

Figure 6.15: Evolution of spherical coordinates during the first 0.6 days of the maneuver for several levels of force mis-prediction

In this figure, several levels of force mis-prediction have been evaluated. These levels are chose according to the results found in the previous chapter. Furthermore, an under-prediction of 10% causes a collision between the two bodies and is therefore left out. From the figure, it can be seen that after a settling time of 0.1 days, as selected in the control algorithm, the spherical angles reach their reference state. It can be clearly seen, that different force estimates in the controller result in varying equilibrium separation distances. Furthermore, the thrust magnitude settles at a value of $4-6$ mN depending on the estimation error, as can be seen in Figure 6.16.

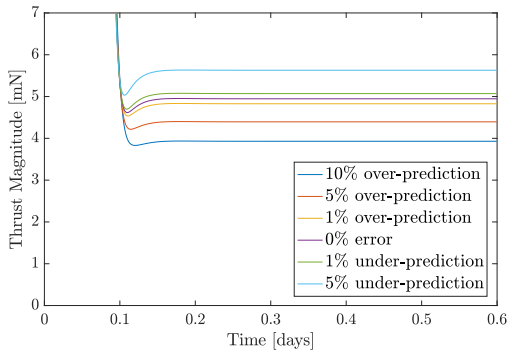

Figure 6.16: Evolution of thrust magnitude during the first 0.6 days of the maneuver for several levels of force mis-prediction.

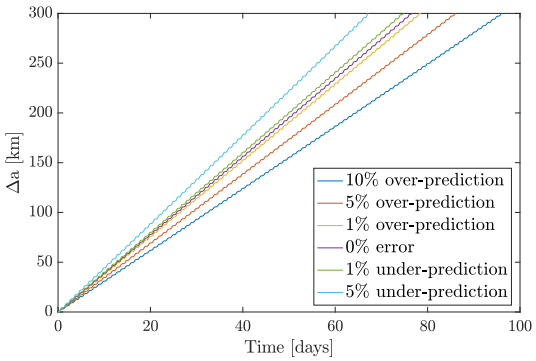

Figure 6.17: Change in semi-major axis over time for several levels of force mis-prediction.

In order to find the difference in reorbiting time and fuel cost for various levels of force mis-prediction, an orbit propagator is used. The orbit is propagated after the settling conditions have been reached, i.e. after 0.2 days. From this point onwards, it is assumed that the thrust is constant and the change in fuel mass has a negligible effect on reorbiting time. Furthermore, the maneuver takes place in one plane and starts at Geostationary Orbit (GEO) altitude.

The orbit propagator used is based on the explicit Runge-Kutta method incorporated in the Matlab function *ODE45*[52]. This function requires an initial state vector $\mathrm{X}_0 = [a, u, v]_0^T$ where the semi-major axis is given by a, the radial velocity by u and the tangential velocity of the tug-debris system by v. The state vector is propagated based on the derivatives of each entry according to the Runge-Kutta scheme. These derivatives can be found in Equations 6.1a through 6.1c.

$$da = u \tag{6.1a}$$

$$du = \frac{v^2}{a} - \frac{\mu_0}{a^2} + \frac{T}{m_\mathrm{t} + m_\mathrm{d}} \tag{6.1b}$$

$$dv = \frac{uv}{a} + \frac{T}{m_\mathrm{t} + m_\mathrm{d}} \tag{6.1c}$$

In these equations, μ_0 represents the standard gravitational of the Earth and m_t and m_d the mass of the tug and debris respectively. Again, a planar motion is described with constant mass and thrust along the trajectory. Propagating the orbit of the tug-debris system for each of the distinct force mis-prediction cases yields the raise in semi-major axis displayed in Figure 6.17. From this figure, it can be deduced that a significant time-increase (20 days) for the maneuver results from a 10% over-prediction. The fuel spend during this maneuver can be found with Equations 6.2a and 6.2b.

$$\dot{m} = \frac{T}{I_\mathrm{sp} g_0} \tag{6.2a}$$

$$m_\mathrm{f} = \dot{m} \Delta t \tag{6.2b}$$

In these equations, the thrust magnitude is given by T, the specific impulse by I_{sp}, the standard acceleration due to gravity by g_0 and time to reorbit by t. An overview of all these values for the corresponding mis-predictions can be found in Table 6.2.

Table 6.2: Overview of thrust settings, time and fuel consumption for a variation of force mis-prediction levels.

Error [%]	T [mN]	$\dot{m}$ [mg/s]	t [days]	m_f [kg]
10 (op)	3.93	0.134	95.98	1.11
5 (op)	4.39	0.149	85.92	1.11
1 (op)	4.83	0.164	78.57	1.11
0	4.95	0.168	76.70	1.11
1 (up)	5.07	0.172	74.79	1.11
5 (up)	5.63	0.191	67.15	1.11

I_{sp} = 3000 s, m_t=1000 kg, m_d=2000 kg

op = over-prediction, up = under-prediction

As a constant thrust is applied, and a constant mass of the system assumed, the fuel spend during the maneuver is equal for each of the scenarios. In a real application scenario of the ET however, amongst others gravity losses, aerodynamic drag and attitude control thrusting increase the fuel cost over time. The most fuel efficient maneuver is therefore one with the short transfer time, preferably with an impulsive shot instead of continuous thrusting. For the application of the ET such a continuous thrust is required however. Furthermore, a safe distance should be kept from the debris, putting a lower bound on the time that is spend to reorbit the body.

Now that the fuel cost can be evaluated based on force mis-prediction levels, the results obtained from the RSEC method can be put to the test. From the numerical validation with FEA data, a mean force mis-prediction of 6.8% is obtained for a number of 7 spheres on the debris (see Figure 6.6). As it is uncertain whether this value is an over or under-prediction, both cases are evaluated. The results can be found in Table 6.3.

Table 6.3: Overview of thrust settings, time and fuel consumption for force mis-prediction levels found from FEA validation.

Error [%]	T [mN]	$\dot{m}$ [mg/s]	t [days]	m_f [kg]
0	4.95	0.168	76.70	1.1138
6.8 (op)	4.22	0.143	89.73	1.1113
6.8 (up)	5.92	0.201	63.93	1.1114

I_{sp} = 3000 s, m_t=1000 kg, m_d=2000 kg

op = over-prediction, up = under-prediction

Based on this data, it can be concluded that an expected force mis-prediction will cause a uncertainty in reorbiting time of around 13 days. On a scale of 76 days, this is an acceptable deviation, taking into account the low computational cost of the RSEC method.

7

Conclusions and Recommendations

This thesis addresses a method which can be used to characterize the electrostatic behavior of space debris, or other charged objects in space. Focusing specifically at the Electrostatic Tractor (ET), the Coulomb force between debris and a dedicated spacecraft (tug) can be estimated by applying this Remote Sensing for Electrostatic Characterization (RSEC) method. In order to reorbit debris with the ET and ensure a collision-less application, the debris has to be characterized in real-time. In order to do so, potential measurements are performed over a full (tumbling) rotation of the debris. It is assumed that the rotational rate, as well as separation distance, are known from measurements with techniques such as Light Detection and Ranging (LiDAR). From a reference Multi-Sphere Method (MSM) model, a potential curve is obtained which can be compared with the measured 'truth' potential. By matching these two potential curves, a best-fit MSM model is found. Using this model, the Coulomb force in the system can be obtained, which is the most important metric for the ET. In order to test the accuracy of the RSEC method, numerical simulations are performed. By performing a Finite Element Analysis (FEA) simulation of debris rotating about a single axis, a truth-model is constructed. Based on this model, a Surface Multi-Sphere Method (SMSM) model is also constructed, allowing for rotations about multiple axis, while keeping computational costs manageable. By comparing the Coulomb force obtained from the RSEC method with the two numerical simulations, the accuracy and performance of the method is tested. Based on this work, some conclusions and recommendations can be made.

7.1. Conclusions

The core of the RSEC method is that measured potential signals are compared with the potential curves resulting from the MSM model, such that an optimization can be performed on this model. The parameters that have to be optimized, are the sphere locations and radii, as well as the debris potential. From analysis, it is found that normalizing the potential signals, allows for decoupling of the sphere radii and potential. The result of this, is that optimization can be broken down in two stages; an initial optimization for only sphere locations and a second optimization including the debris radii and potential. Furthermore, it is shown that normalization of potential measurements reduces the influence of the coupled capacitance between spheres on the debris when optimizing. It is shown that the sum of single-sphere debris models approximates a single model of multiple spheres on the debris reasonably well. For some debris and tug geometries, the implication of decoupling parameters, is that (semi)-analytical solutions can be found, or the model broken down in simpler parts. This can prove to be beneficial for computational cost when applied in satellites, which in general have limited computing power.

In order to obtain the best results from optimization in the RSEC method, several cost functions, boundary conditions and optimizing functions and methods have been evaluated. Based on computational cost and applicability, the gradient based solver *fmincon* within Matlab is used. It is applied for two different methods, where the first is a two-step optimization and the second a single-step optimization. For the first method, an initial optimization is performed to find sphere locations based on unit radii

and potential. Using these locations as initial input, a second optimization is performed to find the best-fitting MSM model as well as debris potential. The second method assumes a random distribution of spheres and radii, as well as potential, and optimizes with those parameters as input. These two methods are chosen as to show robustness and to demonstrate the decoupling accuracy. Robustness is provided by performing optimization from random input, such that the least amount of assumptions is required for a well functioning RSEC method. By analyzing the results of the optimizer, it is found that spheres are predominantly placed at locations where charge moves around a lot; i.e. at the edge and far ends of bodies. The result of this behavior is that the potential field internal to bodies is not well matched, while external behavior is estimated very well. As the Coulomb force between the bodies should be estimated accurately, accuracy in external behavior is preferred.

The RSEC method is put to test using a FEA simulation. A debris model consisting of a block and two plates and a tug represented by a sphere is constructed. For such a relatively simple model, the amount of cells that have to be evaluated is already large. In order to obtain data within a day, the calculations are performed on a cluster from TU Delft. Even for such a high-fidelity simulation, discrepancies can be found in the data. In order to model more complex rotations than the single axis rotation applied in the FEA, a SMSM model is constructed. By matching the charge on the bodies in this model with that found from the FEA results, a comparable model is created. Performing a simulation with this model required significantly less time; minutes instead of a full day. By evaluating the potential fields obtained from both FEA and SMSM, it can be concluded that the discrepancy between the two is fairly small. The largest errors are found at the surface of the bodies and near the zero-potential contour, although the error in the latter is small in absolute measures. The error at the surface is expected, as it is a result of the inherent difference between both methods; continuous charge distribution and one contained in spheres.

By applying the RSEC method to the data obtained from both FEA and SMSM, best-fit MSM models are obtained. As expected from the analysis performed for the optimizing function, the spheres are predominantly located at the edge of the debris; i.e. at the far end of the panels. Furthermore, both method 1 and method 2 seem to provide comparable results. For the FEA data, the best results are obtained for a sphere population of 6 on the debris. Fewer spheres will increase the error, while many more will not contribute to the solution. Both methods show a mean error in force of below 10%. An offset of the error could be found due to an error in tug calibration. The result of this, is an over-prediction in force, which is preferred over under-prediction, as the latter can cause collisions. Further analysis has to be performed however to check for consistency of over-prediction. Application of the RSEC method to the SMSM data shows enhanced performance with respect to that of the FEA simulation. Force predictions around percent error can be expected, showing the strength of the method.

Translating the force mis-prediction to fuel and reorbiting cost, a control law is implemented. For a mission scenario where a 1000 kg tug has to reorbit a 2000 kg debris from Geostationary Orbit (GEO) to a graveyard orbit 300 km higher, it can be found that a percent error will only increase the reorbit time by 2 days. Applying the results from the FEA analysis however, a 10% mis-prediction in Coulomb force, leads to almost 20 days of increased mission time cost. Considering the nominal time to reorbit of 77 days, this is still a fine result.

Stating the conclusion of this work into one paragraph, it can be said that the RSEC method shows a promising method to estimate the electrostatic behavior of debris in a real-time manner. Applying measured potential over a full rotation, the RSEC method is able to find a best-fit MSM model in the matter of tens of minutes. After finding this model, the method is able to predict within 10% accuracy the Coulomb force in a manner of minutes to even seconds, whereas conventional methods such as FEA simulations takes days to find the electrostatic characteristics of charged body. Linking these findings back to the research objectives, it can therefore be concluded that the method has real-time applicability, is characterized by accuracies higher than simple two-sphere models and allows for evaluation of full spatial geometries and multi-axis tumbling of the debris.

7.2. Recommendations

Although a lot of effort has been spent on verifying the RSEC method for as many scenarios as possible, there are still some interesting simulations to perform. Highly irregular shapes such as asteroids and complex tumbling motions, or very marginal rotations that show almost no variation in signal, might constrain the accuracy of the method. Furthermore, in a real-time application, measurements of potential, rotation rates and separation distance will introduce noise to the system. Performing parameter variations can provide more understanding of the influence these parameters have on the RSEC accuracy.

Even higher-fidelity FEA simulations will help to improve the validity of the RSEC method. In stead of simulations, even experiments can be performed, such as described in Stevenson and Schaub [42]. Validating the method with experiments, can lift the Technical Readiness Level. Furthermore, it introduces measurement errors, such that the robustness of the method can be tested. In order to conduct experiments, probing techniques have to be developed capable of measuring kilovolt potential at distances from the charged surface. Some possibilities have been described, but it was found that conducting a proper experiment will take a fair bit of time. This might open up possibilities for other students to spend their thesis work on.

In terms of extension to the current simulations, not even more complex geometries have to be tested, but also the physics involved have to be adjusted. This work has neglected the influence of the ambient plasma, the (varying) space weather, charging effects such as discharges and materials and surfaces that are not perfectly conducting. In order to model these parameters, the Spacecraft Plasma Interaction Software (SPIS) could be used [53]. This software is a common tool to simulate the interaction of satellites with the local plasma environment in space.

Lastly, the research performed by others in this field can be incorporated. Extending from the Coulomb force simulations, also the torque can be validated. This can be used to test the detumbling capabilities of the ET. Furthermore, the research being conducted concerning the SMSM could be used as to create homogeneous initial sphere populations in order to aid the optimization algorithms. As the RSEC method has to be developed further, an endless stream of possible features and research questions can be thought of.

Bibliography

[1] NASA Orbital Debris Program Office, *Orbital Debris Quarterly News*, Report (NASA, 2017).

[2] H. Schaub and Z. Sternovsky, *Active space debris charging for contactless electrostatic disposal maneuvers,* Advances in Space Research **53**, 110 (2014).

[3] D. Stevenson and H. Schaub, *Optimization of sphere population for electrostatic multi-sphere method,* Plasma Science, IEEE Transactions on **41**, 3526 (2013).

[4] National Instruments, *3d cartesian coordinate rotation (euler) vi,* https://zone.ni.com/reference/enXX/help/371361H01/gmath/3d_cartesian_coordinate_rotation_euler/ (accessed on: 26-2-2017).

[5] E. A. Hogan and H. Schaub, *Relative motion control for two-spacecraft electrostatic orbit corrections,* Journal of Guidance, Control, and Dynamics **36**, 240 (2012).

[6] National Aeronautics and Space Administration, *Suitsat-1 floats free,* https://www.nasa.gov/multimedia/imagegallery/image_feature_514.html (accessed on: 10-2-2017).

[7] D. J. Kessler and B. G. Courpalais, *Collision frequency of artificial satellites - creation of a debris belt,* Journal of Geophysical Research-Space Physics **83**, 2637 (1978).

[8] K. Wormnes, R. Le Letty, L. Summerer, R. Schonenborg, O. Dubois-Matra, E. Luraschi, A. Cropp, H. Krag, and J. Delaval, *Esa technologies for space debris remediation,* in *Proceedings of the 6th IAASS Conference: Safety is Not an Option* (2013) pp. 3–4.

[9] L. Anselmo, A. Rossi, and C. Pardini, *Updated results on the long-term evolution of the space debris environment,* Advances in Space Research **23**, 201 (1999).

[10] H. Engwerda, *Literature study: Active space debris removal feasibility study,* (2016).

[11] A. Parness, T. Hilgendorf, P. Daniel, M. Frost, V. White, and B. Kennedy, *Controllable on-off adhesion for earth orbit grappling applications,* in *Aerospace Conference, 2013 IEEE* (IEEE, 2013) pp. 1–11.

[12] L. Cercós, R. Stefanescu, A. Medina, R. Benvenuto, M. Lavagna, I. González, N. Rodríguez, and K. Wormnes, *Validation of a net active debris removal simulator within parabolic flight experiment,* (2014).

[13] R. Dudziak, S. Tuttle, and S. Barraclough, *Harpoon technology development for the active removal of space debris,* Advances in Space Research **56**, 509 (2015).

[14] C. Bombardelli, H. Urrutxua, M. Merino, E. Ahedo, J. Pelaez, and J. Olympio, *Dynamics of ion-beam-propelled space debris,* in *International Symposium on Space Flight Dynamics, Sao Jose dos Campos, Brasil* (2011).

[15] C. Bombardelli and J. Pelaez, *Ion beam shepherd for contactless space debris removal,* Journal of guidance, control, and dynamics **34**, 916 (2011).

[16] D. F. Moorer Jr and H. Schaub, *Electrostatic spacecraft reorbiter,* (2012).

[17] H. Schaub and D. F. Moorer Jr, *Geosynchronous large debris reorbiter: Challenges and prospects,* The Journal of the Astronautical Sciences **59**, 161 (2012).

[18] H. Schaub and L. E. Jasper, *Circular orbit radius control using electrostatic actuation for 2-craft configurations,* Advances in the Astronautical Sciences **142** (2011).

[19] P. Chrystal, D. McKnight, P. Meredith, J. Schmidt, M. Fok, and C. Wetton, *Space debris: on collision course for insurers,* Swiss Reinsurance Co. Publ., Zurich, Switzerland, March (2011).

[20] D. Stevenson and H. Schaub, *Multi sphere modeling for electrostatic forces on three-dimensional spacecraft shapes,* in *AAS/AIAA Spaceflight Mechanics Meeting, Charleston, South Carolina, Jan*, pp. 12–106.

[21] T. Bennett, D. Stevenson, E. Hogan, and H. Schaub, *Prospects and challenges of touchless electrostatic detumbling of small bodies,* Advances in Space Research **56**, 557 (2015).

[22] T. Bennett and H. Schaub, *Touchless electrostatic three-dimensional detumbling of large axi-symmetric debris,* The Journal of the Astronautical Sciences **62**, 233 (2015).

[23] H. Engwerda, J. Hughes, and H. Schaub, *Remote sensing for planar electrostatic characterization using the multi-sphere method,* in *Stardust Final Conference on Asteroids and Space Debris*, pp. 242–252.

[24] T. Jackson, M. Zimmerman, and W. Farrell, *Concerning the charging of an exploration craft on and near a small asteroid,* (2014).

[25] W. Farrell, T. Stubbs, R. Vondrak, G. Delory, and J. Halekas, *Complex electric fields near the lunar terminator: The near-surface wake and accelerated dust,* Geophysical Research Letters **34** (2007).

[26] M. H. Kaplan, B. Boone, R. Brown, T. Criss, and E. Tunstel, *Engineering issues for all major modes of in situ space debris capture,* in *AIAA Space 2010 Conference, paper AIAA*, Vol. 8863 (American Institute of Aeronautics and Astronautics, 2010).

[27] S. E. DeForest and C. McIlwain, *Plasma clouds in the magnetosphere,* Journal of Geophysical Research **76**, 3587 (1971).

[28] S. E. DeForest, *Spacecraft charging at synchronous orbit,* Journal of Geophysical Research **77**, 651 (1972).

[29] M. S. G. E.G. Mullen and D. A. Hardy, *Scatha survey of high-level spacecraft charging in sunlight,* Journal of Geophysical Research **91**, 16 (1986).

[30] M. H. Denton, M. Thomsen, H. Korth, S. Lynch, J.-C. Zhang, and M. Liemohn, *Bulk plasma properties at geosynchronous orbit,* Journal of Geophysical Research: Space Physics **110** (2005).

[31] J. Hughes and H. Schaub, *Monte-carlo analysis of the pulsed electrostatic tractor strength,* (2016).

[32] S. A. O'Keefe and H. Schaub, *Shadow set considerations for modified rodrigues parameter attitude filtering,* Journal of Guidance, Control, and Dynamics **37**, 2030 (2014).

[33] H. Schaub, P. Tsiotras, and J. L. Junkins, *Principal rotation representations of proper n× n orthogonal matrices,* International Journal of Engineering Science **33**, 2277 (1995).

[34] D. Stevenson and H. Schaub, *Multi-sphere method for modeling spacecraft electrostatic forces and torques,* Advances in Space Research **51**, 10 (2013).

[35] S. E. Jo, S. W. Kim, and T. J. Park, *Equally constrained affine projection algorithm,* in *Signals, Systems and Computers, 2004. Conference Record of the Thirty-Eighth Asilomar Conference on*, Vol. 1 (IEEE) pp. 955–959.

[36] The Mathworks Inc, *fsolve: solve system of nonlinear equations,* https://nl.mathworks.com/help/optim/ug/fsolve.html (accessed on: 25-2-2017).

[37] D. Stevenson, *Remote Spacecraft Attitude Control by Coulomb Charging*, Thesis (2015).

[38] R. Stengel, *Introduction to optimization,* Lecture Slides: Robotics and Intelligent Systems (2015).

[39] The Mathworks Inc, *fmincon: Find minimum of constrained nonlinear multivariable function,* http://nl.mathworks.com/help/optim/ug/fmincon.html (accessed on: 25-2-2017).

[40] The Mathworks Inc, *Multistart class: Find multiple local minima,* https://nl.mathworks.com/help/gads/multistart-class.html (accessed on: 25-2-2017).

[41] C. R. Seubert and H. Schaub, *Electrostatic force model for terrestrial experiments on the coulomb testbed,* in *61st International Astronautical Congress, Prague, CZ, International Astronautical Federation*.

[42] D. Stevenson and H. Schaub, *Rotational testbed for coulomb induced spacecraft attitude control,* in *5th International Conference on Spacecraft Formation Flying Missions and Technologies, Munich*.

[43] P. van Nes and A. Rodrigo Mor (TU Delft Faculty of Electrical Engineering, Mathematics and Computer Science), *Personal communication,* (2016).

[44] T. Inc, *Trek model 820 infinitron high impedance contacting/non-contacting voltmeter datasheet,* (2012).

[45] J. N. Chubb, *Two new designs of'field mill'type fieldmeters not requiring earthing of rotating chopper,* IEEE Transactions on Industry Applications **26**, 1178 (1990).

[46] AB COMSOL, *Comsol multiphysics user's guide,* Version: September **10**, 333 (2005).

[47] L. E. Jasper and H. Schaub, *Effective sphere modeling for electrostatic forces on three-dimensional spacecraft shapes,* Advances in the Astronautical Sciences **142** (2011).

[48] AB COMSOL, *Livelink for matlab user's guide,* Part Number CM020008 (2014).

[49] R. Bauer, *Distribution of points on a sphere with application to star catalogs,* Journal of Guidance, Control, and Dynamics **23**, 130 (2000).

[50] The Mathworks Inc, *interp2: Interpolation for 2-d gridded data in meshgrid format,* https://nl.mathworks.com/help/matlab/ref/interp2.html (accessed on: 26-2-2017).

[51] The Mathworks Inc, *fft fast fourier transform,* https://nl.mathworks.com/help/matlab/ref/fft.html (accessed on: 25-2-2017).

[52] The Mathworks Inc, *ode45: Solve nonstiff differential equations - medium order method,* http://nl.mathworks.com/help/matlab/ref/ode45.html (accessed on: 25-2-2017).

[53] J.-F. Roussel, F. Rogier, D. Volpert, J. Forest, G. Rousseau, and A. Hilgers, *Spacecraft plasma interaction software (spis): Numerical solvers. methods and architecture,* in *title 9th Spacecraft Charging Technology Conference 9th Spacecraft Charging Technology Conference*, p. 462.